

University of St Andrews



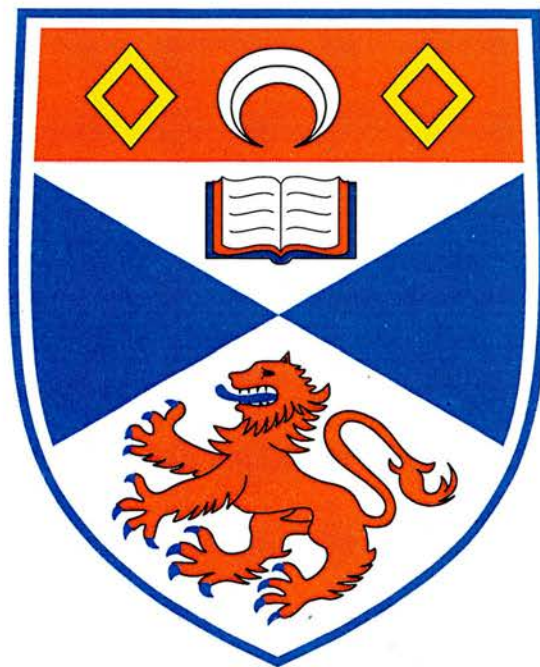
Full metadata for this thesis is available in
St Andrews Research Repository
at:

<http://research-repository.st-andrews.ac.uk/>

This thesis is protected by original copyright

Non-linear MHD simulations of Solar Coronal structures

Robert Kevis



Thesis submitted for the degree of Doctor of Philosophy
of the University of St Andrews

December 18, 2005



Th
F120

Abstract

The aim of this thesis is two-fold: the development and testing of a numerical code which solves the non-linear magnetohydrodynamic equations, and in particular is capable of accurately resolving interfaces; two solar coronal heating mechanisms are investigated.

A number of problems in astrophysics involve qualitatively different regions. For example, the photosphere and chromosphere or prominence and surrounding atmosphere in a Solar context, and a re-entry vehicle and surrounding atmosphere in a broader Solar system context. In this thesis, a non-linear shock-capturing code for the resistive magnetohydrodynamic equations has been converted into a multi-material code. Interface tracking algorithms have been written and incorporated into the code, so the overall scheme can accurately resolve material boundaries. The code has been parallelised using the MPI library. The interface tracking capabilities of the code have been rigorously tested against well known test cases found in the literature.

How the Solar Corona is heated to millions of degrees is one of the outstanding problems in Solar physics. It is widely thought that the heating mechanism relies upon the coronal magnetic field, and a number of heating mechanisms have been proposed. In this thesis two such mechanisms are investigated numerically. Firstly, the non-linear phase-mixing of Alfvén waves in the presence of uniform resistivity is investigated. Secondly, a nanoflare model, whereby a kink unstable coronal loop relaxes to a lower energy state, is investigated.

Declaration

1. I, Robert Kevis, hereby certify that this thesis, which is approximately 21 000 words in length, has been written by me, that it is a record of work carried out by me and that it has not been submitted in any previous application for a higher degree.

date *19/12/05* signature of candidate .

2. I was admitted as a research student in October 2001 and as a candidate for the degree of PhD in October 2002; the higher study for which this is a record was carried out in the University of St Andrews between 2001 and 2005.

date *19/12/05* signature of candidate .

3. I hereby certify that the candidate has fulfilled the conditions of the Resolution and Regulations appropriate to the degree of PhD in the University of St Andrews and that the candidate is qualified to submit the thesis in application for that degree.

date *19/12/05* signature of supervisor

4. In submitting this thesis to the University of St Andrews I understand that I am giving permission for it to be made available for use in accordance with the regulations of the University Library for the time being in force, subject to any copyright vested in the work not being affected thereby. I also understand that the title and abstract will be published and that a copy of the work may be made and supplied to any bona fide library or research worker.

date *19/12/05* signature of candidate .

Acknowledgements

I would like to thank the many friends and family members who have smiled and nodded at the appropriate junctures in many of our conversations over the past four years. I would

also like to thank Alan Hood for his patience, and for his vain attempts in trying to keep me focused on only one or two problems. Thanks must also go to Aaron Longbottom,

who managed to make many aspects of computational physics transparent enough for even me to understand them. Praise should also be given to Keith Bennett and Dan Brown, who were always willing to help me fix the many and exotic bugs I uncovered. I would

like to gratefully acknowledge the financial support of PPARC. The numerical simulations were carried out using the PPARC/SRIF funded maths cluster in St Andrews.

Contents

1	Introduction	1
1.1	The Sun	1
1.2	The Magnetohydrodynamic (MHD) equations	6
1.3	Aspects of Linear Wave Theory	12
1.4	Aspects of Magnetic Reconnection	14
1.5	Numerical basics	17
1.5.1	Linear stability theory	19
1.5.2	Some basic schemes	22
1.5.3	Demonstration of numerical dissipation and dispersion	24
1.5.4	Discontinuities	28
1.6	Summary	29
2	A Multi-material code for Resistive MHD	30
2.1	Introduction	30
2.1.1	Shock capturing methods	31
2.1.2	Contact algorithms	31
2.2	The Grid	33
2.3	Volume Of Fluid methodology	34
2.4	The Equations	36
2.4.1	The Equation Of State	38
2.4.2	The multi-material equations	39
2.4.3	Mixing theory	40
2.5	The Lagrangian step	42
2.5.1	The magnetic field	44

2.5.2	Artificial viscosity	45
2.5.3	The CFL condition	48
2.6	The Remap step	49
2.6.1	Single material remap of Fluid variables	50
2.6.2	Gradient Limiters	53
2.6.3	Multi-material remap of Fluid variables	55
2.6.4	Magnetic flux remap	57
2.7	Summary	59
3	Interface tracking algorithms	60
3.1	Introduction	60
3.2	Piecewise Constant Methods	60
3.2.1	The SLIC algorithm	61
3.2.2	Difficulties with Piecewise constant Methods	64
3.3	Piecewise linear Methods	65
3.3.1	Youngs algorithm	65
3.3.2	Further developments of PLIC methods	71
3.3.3	New developments	77
3.4	Summary	77
4	Test cases	78
4.1	Introduction	78
4.2	Advection tests	78
4.2.1	Notched circle	78
4.2.2	Single vortex	79
4.2.3	Deformation field	80
4.3	1D tests	81
4.3.1	1D shock tube problem	81
4.3.2	Interacting blast waves	83
4.3.3	1.5D MHD shock tube problem	84
4.4	2D tests	85
4.4.1	2D Riemann problem	85
4.4.2	Implosion problem	86

4.4.3	Explosion problem	88
4.5	Multi-material tests	88
4.5.1	2D air cavity collapse in water	88
4.5.2	Air-Helium shock interaction	90
4.6	Summary	90
5	Non-linear phase-mixing of an Alfvén wave	91
5.1	Introduction	91
5.2	The Equations	92
5.3	The model	94
5.4	The $\beta = 0, \eta = 0$ case	96
5.5	The $\beta \neq 0, \eta = 0$ case	99
5.6	The resistive effects	101
5.7	Conclusions	105
6	Ongoing research: Coronal heating by nanoflares triggered by an ideal kink instability in a loop	106
6.1	Introduction	106
6.2	The model	109
6.3	Preliminary results	111
6.3.1	Case 1	111
6.3.2	Case 2	112
7	Summary	115
A	Derivation of artificial viscosity	117
B	Integration of the Induction equation	120
C	Initialising a volume fraction field	122
D	Discretisation of the multi-material Ideal gas equations	124
D.1	Conservation of mass	124
D.2	Conservation of momentum	125
D.3	Specific internal energy	126

D.4 Energy conservation	128
Bibliography	129

List of Figures

1.1	The interior and atmospheric layers of the Sun.	2
1.2	Helioseismology: sound waves of different wavelengths penetrate to different depths of the solar interior.	2
1.3	Plasma in the interior of the Sun rotates at different speeds. Image courtesy of SOHO/MDI, 1997. SOHO is an international project between ESA and NASA.	3
1.4	Coronal loops observed at the 171\AA pass band. Image courtesy of TRACE 06/11/999. TRACE is part of NASA's Earth-Sun system mission program.	4
1.5	The solar activity cycle. Images of the Sun's atmosphere obtained between 1991 and 1995 at 120 day increments. Image courtesy of Yohkoh/SXT. Yohkoh was an international project between Japan, the US. and the UK.	4
1.6	The Butterfly diagram shows the latitude of sunspot appearance as a function of year, from 1874-1996. Image courtesy of the Marshall Space Flight Center.	5
1.7	A sunspot group clearly indicating the dark umbra and penumbra filaments. Photospheric granulation can also be discerned. Image courtesy of the Swedish 1m. Solar Telescope, 06/02.	5
1.8	A SOHO/LASCO coronagraph of a transversely directed CME. Image courtesy of NRL.	6
1.9	Sweet-Parker diffusion region with oppositely directed magnetic fields.	15
1.10	Petschek reconnection region, the diffusion region is shaded.	17
1.11	Example of aliasing: both the function and the samples vary sinusoidally, but the samples possess a longer wavelength.	18
1.12	An example of an implicit stencil.	20
1.13	Simulation of the advection equation using FTCS with 1000 grid points.	23
1.14	Exact solution of the advection problem.	25

1.15	1 st order diffusive simulation of the advection equation, with uniform grid spacing $\delta x = 0.2$	26
1.16	2 nd order dispersive simulation of the advection equation, with uniform grid spacing $\delta x = 0.2$	27
2.1	Schematic of Riemann method: a) cell centred variables (dots) are used to approximate the gradient (dashed line) which may be limited (shaded volume); b) characteristics traced to form left and right hand states of the Riemann problem; c) Riemann problem determines the fluxes used in the conservative equations.	32
2.2	Schematic of the Lagrangian-Remap technique.	33
2.3	Cell labellings and a logically structured grid defined by two sets of intersecting lines.	34
2.4	Variable placement for a staggered grid in two and three dimensions.	34
2.5	Development of the chequerboard instability from an initially square wave using the Leapfrog method.	35
2.6	An initial mixed Eulerian cell and the developed Lagrangian cell according to "Equal expansion".	41
2.7	An initial mixed Eulerian cell and the developed mixed Lagrangian cell with one material incompressible.	41
2.8	Eulerian and Lagrangian cells at the end of the Lagrangian step.	44
2.9	Noh's wall heating problem, increasing the artificial viscosity to control the shocks at $x = 0.16$ and $x = 0.84$ increases the error at the "wall", $x = 0.5$	48
2.10	Single material density remap: showing a Lagrangian cell whose bulk motion is to the right of the Eulerian cell. The shaded region depicts dM_i	51
2.11	Single material specific energy remap: showing a Lagrangian cell whose bulk motion is to the right of the Eulerian cell. The shaded region depicts $d\zeta_i$	52
2.12	The monotonicity condition: a) The gradient (solid line) of the central cell is reduced (bold line) so that values in this cell do not go beyond the average levels (dotted line) in the adjacent cells; b) If the grid average reaches an extremum, the gradient is set to zero; c) If the gradient does not agree with the trend in the grid averages, then it is set to zero.	54

2.13	Example of a multi-material region for stencil (2.40a) where $u_x, u_y > 0$	55
2.14	Multi-material remap of volume: showing a mixed Lagrangian cell (SLIC Type IV) whose bulk motion is to the right of the Eulerian cell.	56
2.15	The evolution of an isolated flux tube passing through a cell.	58
3.1	The x and y SLIC reconstructions of a portion of a circle.	62
3.2	A cell with three materials, and SLIC's representation of the cell where materials two and three - which possess the same material index - are combined as material β	62
3.3	The six material configuration types recognised by SLIC.	63
3.4	Rayleigh-Taylor instability at $t = 12.5$ with the SLIC and Youngs algorithms respectively.	65
3.5	The stencil for Young's method for calculating the interface normal. The arrow indicates the transport direction.	66
3.6	The two possible cases, after translation, for a line to intersect a cell.	68
3.7	An example showing the initial and translated orientations of a cell.	68
3.8	The five possible cases, after translation, for a plane to intersect a cell.	69
3.9	The triangular case.	69
3.10	The quadrilateral case.	70
3.11	An example of a mixed cell possessing a "T-join", and the <i>onion skin</i> representation of that same cell.	71
3.12	Contours of density for the Rayleigh-Taylor problem, with the single material, multi-material, and double the resolution single material simulations respectively.	72
3.13	An example of a multi-material region - with volume fraction data - where Young's interface stencil fails to reproduce a straight line exactly.	73
3.14	Young's reconstruction of a portion of a circle.	74
3.15	A hinged line interface. The dashed line indicates the original Young's interface reconstruction.	75
3.16	HELMIT's ability to construct "T-joins".	75
3.17	The material ordering problem encountered by a fixed priority list, and the improvement gained by a background algorithm.	76
4.1	The initial notched circle, and the notched circle after one revolution.	79

4.2	Vortex problem at $t = 4$ and $t = 8$ where $T = 8$	80
4.3	Deformation problem at $t = 1$ and $t = 2$ where $T = 2$	81
4.4	Density profile for Sod's problem at $t = 0.1$, with an enlargement of the contact discontinuity.	82
4.5	Plot and contour of density for the Sod problem, at 45° and 30° respectively.	82
4.6	Density profile for interacting blast wave problem at $t = 0.038$. Solid line depicts the exact solution (4800 grid points), the dashed line the single material case (1200 grid points) and the symbols the multi-material case (1200 grid points).	83
4.7	Profiles for the Brio & Wu shock tube problem. Diamonds represent the single material code, crosses the multi-material code.	84
4.8	Single and multi-material contours of the 2D Riemann problem.	86
4.9	Implosion problem with a dimensionally split code.	86
4.10	Single and multi-material contours for the Implosion problem.	87
4.11	Single and multi-material explosion test.	88
4.12	Density contours for 2D air cavity collapse.	89
4.13	Air-Helium interaction at $t = 123.8$	90
5.1	Density (solid line) and Alfvén velocity (dashed line) profiles for the periodic and driven set ups respectively.	95
5.2	Plot of u_z showing the ponderomotive effect and acoustic mode.	96
5.3	Contours of u_y and b_y respectively, showing the phase-mixed Alfvén wave at $t = 5$ for the periodic case.	97
5.4	Perpendicular and parallel components of velocity respectively, for the periodic case at $t = 5$	98
5.5	Comparison of slices across the x -direction of the perpendicular and parallel velocity components respectively, for $\beta = 0$ (solid line), $\beta = 0.01$ (dotted line), $\beta = 0.1$ (dashed line) and $\beta = 1$ (dot-dashed line) at $t = 1$	99
5.6	Comparison of slices across the z -direction of the perpendicular and parallel velocity components respectively, for $\beta = 0$ (solid line), $\beta = 0.01$ (dotted line), $\beta = 0.1$ (dashed line) and $\beta = 1$ (dot-dashed line) at $t = 1$	100
5.7	Contours of the parallel velocity component for differing values of β at $t = 5$	100

5.8	Comparison of slices across the x -direction of the perpendicular and parallel velocity components respectively, for $\beta = 0$ (solid line), $\beta = 0.01$ (crosses) and $\beta = 0.1$ (dashed line) at $t = 5$	101
5.9	Images of all of the velocity components for the $\eta = 0$ case, at $t = 48$. . .	102
5.10	Images of all of the velocity components for the $\eta \neq 0$ case, at $t = 48$. . .	103
5.11	Comparison of the density perturbation for the $\eta = 0$ (dashed line) and $\eta \neq 0$ (solid line), at 3 locations in x	104
5.12	Comparison of the temperature perturbation for 3 locations in x , where the upper panel considers the case $\eta = 0$ whilst the lower panel considers the case $\eta \neq 0$	104
6.1	Plots of B_z (solid) and B_θ (dashed) for case 1 and case2 respectively. . . .	110
6.2	Isosurfaces of current at $ j = 1.5$ at $t = 100\tau_A$ (left hand side) and $t = 120\tau_A$ (right hand side) for case 1.	111
6.3	Plots of magnetic energy (top, left hand side), kinetic energy (top, right hand side) internal energy (bottom, left hand side) and current (bottom, right hand side) for case 1.	112
6.4	Plots of cumulative ohmic heating (left),and helicity (right) for case 1. . .	112
6.5	Isosurfaces of the loop at $ j = 1.5$ at $t = 10\tau_A$ (left hand side) and $t = 20\tau_A$ (right hand side) for case 2.	113
6.6	Plots of magnetic energy (top, left hand side), kinetic energy (top, right hand side), internal energy (bottom, left hand side) and current (bottom, right hand side) for case 2.	113
6.7	Plots of cumulative ohmic heating (left hand side), and helicity (right hand side) for case 2.	114
C.1	The effect of p on the interface, showing the reconstruction with $p = 1$ and $p = 5$ respectively.	122
C.2	Schematic of the subdividing process for volume fraction initialisation. . .	123

Chapter 1

Introduction

1.1 The Sun

The Sun is an average star, sitting on the main sequence of the Hertzsprung-Russell diagram, which plots colour (temperature) against luminosity. The Sun is middle aged (approximately 5×10^9 years old), has a mass of 2×10^{30} kg and a radius of 7×10^{10} m, giving a mean density of 1.4×10^3 kg/m³. The Sun consists of approximately 93% Hydrogen, 5% Helium and trace amounts of heavier elements. What makes the Sun remarkable is its proximity, making it more readily observable than most astronomical objects. Observing and understanding the Sun is important not just in its own right or for knowledge transferable to other stars and astronomical objects, but also for core plasma dynamics which are not yet reproducible in the laboratory. A schematic of the layers of the Sun is provided in Figure 1.1.

First, consider the solar interior. On the solar surface many oscillations are visible, which penetrate the solar interior, are refracted back towards the solar surface by changes in the plasma, before reflecting off of the surface (see Figure 1.2). The depth to which waves penetrate is dependent upon their wavelength. By careful observation of such waves on the solar surface, properties of the interior may be ascertained. This area of research is called Helioseismology, and is also used to study local subsurface features. The interior then, consists of a core, radiative and convection zones. The core extends to approximately a quarter of the solar radius, and here conditions allow nuclear fusion via

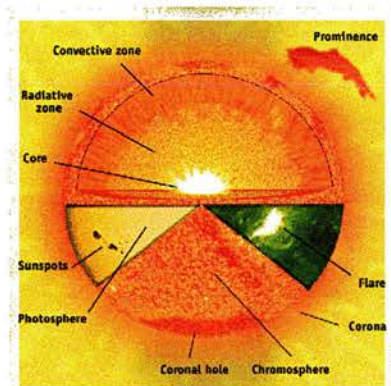


Figure 1.1: The interior and atmospheric layers of the Sun.

the proton-proton chain. By-products of this reaction are a positron which will ultimately be emitted as a photon (with a mean free path of the order of hundreds of thousands of years) and a neutrino which passes unhindered out of the Sun. However, neutrinos are not detected in as large numbers as expected. Extending from the core to approximately 0.7 of the solar radius (Priest, 1982) is the radiative zone. The body of the Sun so far discussed rotates uniformly, this is not the case for subsequent layers and at the surface the equator rotates once in approximately 26 days whereas polar regions take approximately 30 days (Golub and Pasachoff, 2001). The narrow layer where this shear begins is called the tachocline and is believed to be the seat of the large scale dynamo, whereas small scale dynamo motions may be present near the solar surface generating the so-called magnetic carpet. Above the tachocline is the convection zone.

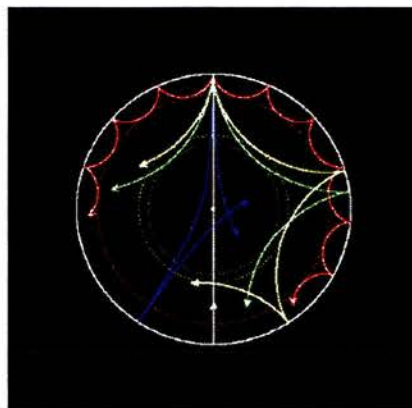


Figure 1.2: Helioseismology: sound waves of different wavelengths penetrate to different depths of the solar interior.

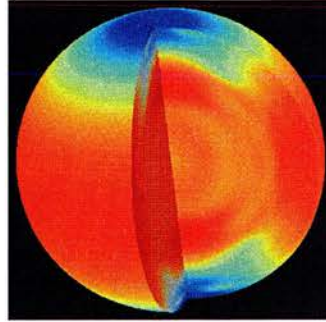


Figure 1.3: Plasma in the interior of the Sun rotates at different speeds. Image courtesy of SOHO/MDI, 1997. SOHO is an international project between ESA and NASA.

The thin, visible layer of the Sun is called the photosphere. Evidence for the convection layer can clearly be seen in the granulation and supergranulation patterns found in the photosphere (see Figure 1.7). The temperature of the photosphere initially falls to a minimum value, and then starts to rise. The average temperature is approximately 6000K. Above the photosphere lies the chromosphere, and in this region the temperature increases monotonically until near the transition region where temperature increases rapidly from approximately 10 000K to 1 000 000K (Golub and Pasachoff, 2001). The outermost atmospheric layer of the Sun is called the corona, and this stretches from the top of the transition region into space as the solar wind. The corona is a very hot ($T \approx 10^6\text{K}$) and tenuous ($\rho \approx 10^{-12}\text{kg/m}^3$) plasma dominated by the magnetic field. Coronal structures are normally divided into two classes: those whose magnetic field connects with the interplanetary magnetic field (open), those whose magnetic field connects solely with the Sun (closed). Open structures, including coronal holes, coronal plumes, streamers, tend to be cooler and less dense. Closed structures, which tend to be located away from the poles, include coronal loops and arcades. The above description of the solar atmosphere can be somewhat misleading, leaving the reader with the impression that the solar atmosphere is simply stratified. Looking at Figure 1.4, one can see this is clearly not the case. Ignoring any temporal evolution of the structures, the complexity, whereby adjacent loops can possess quite different properties, is still evident.

The Sun exhibits an approximately eleven year activity cycle (≈ 22 years for full field reversal), Figure 1.5 clearly shows the difference of the solar Corona between solar maximum and solar minimum. Solar activity is traditionally measured by sunspot number. Observed in the photosphere, sunspots are areas of cool plasma ($T \approx 3700\text{K}$ Priest (1982)) with strong magnetic field ($B \approx 2000 - 4000\text{G}$ Priest (1982)) which normally



Figure 1.4: Coronal loops observed at the 171\AA pass band. Image courtesy of TRACE 06/11/999. TRACE is part of NASA's Earth-Sun system mission program.

consist of a dark central umbra surrounded by a lighter penumbra (Figure 1.7). At the beginning of a solar cycle, sunspots appear at latitudes $\pm 30^\circ$ from the equator. As the cycle progresses, the location of sunspot appearance migrates towards the equator, yielding the well known butterfly diagram (Figure 1.6). The solar cycle is driven by the intensity of the Sun's magnetic field strength, a manifestation of which is the sunspot cycle.

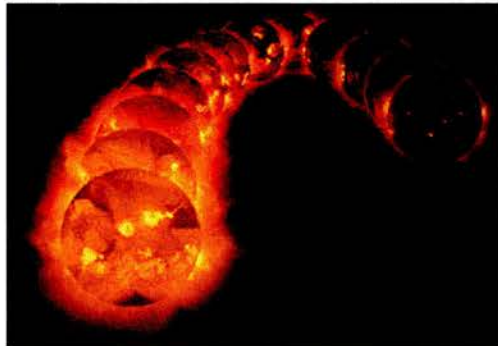


Figure 1.5: The solar activity cycle. Images of the Sun's atmosphere obtained between 1991 and 1995 at 120 day increments. Image courtesy of Yohkoh/SXT. Yohkoh was an international project between Japan, the US. and the UK.

Prominences are observed in the corona (they are called filaments when seen against the solar disc), these are divided into quiescent prominences and active prominences. Quiescent prominences are cool, dense ($T \approx 7000\text{K}$, $n_e \approx 10^{17}\text{m}^{-3}$ Démoulin (1991)) sheets of plasma supported by the local magnetic field, more precisely they lie above a

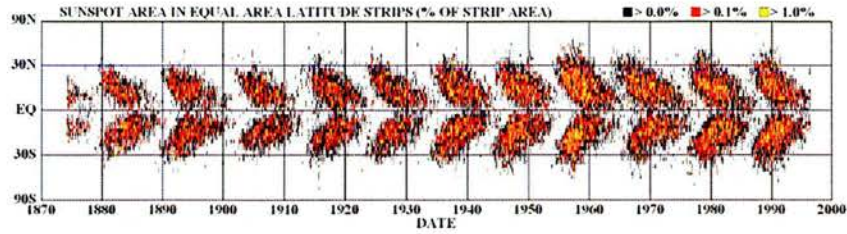


Figure 1.6: The Butterfly diagram shows the latitude of sunspot appearance as a function of year, from 1874-1996. Image courtesy of the Marshall Space Flight Center.

magnetic polarity inversion line. Quiescent prominences range in length (approximately 200Mm Priest (1982)) and can last for several months. Active prominences lie in active regions, are shorter lived and can be associated with eruptive events.

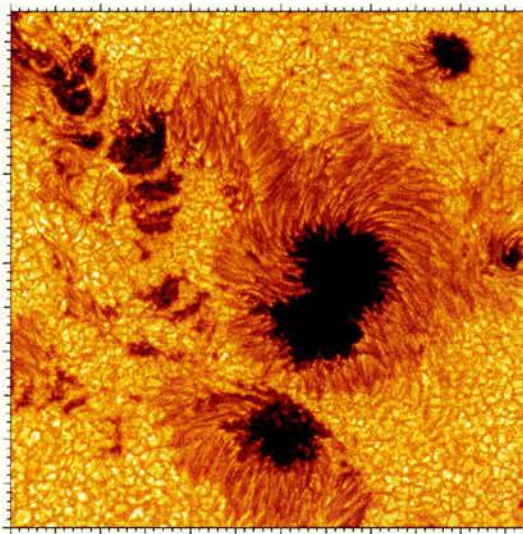


Figure 1.7: A sunspot group clearly indicating the dark umbra and penumbra filaments. Photospheric granulation can also be discerned. Image courtesy of the Swedish 1m. Solar Telescope, 06/02.

The term solar flare encapsulates a range of events, from a simple localised brightening to large complex events in active regions. The flare energy source is the magnetic field and the release mechanism is magnetic reconnection. There is a range of potential triggering mechanisms for a solar flare, a couple of examples are the kink instability and photospheric shearing motions. Flares are normally classified into two groups: compact loop flares and two ribbon flares. Compact loop flares are smaller than two ribbon flares, and consist of the brightening of an individual loop which is not destroyed by the process.

Two ribbon flares normally involve a loop arcade and are sited near an active prominence. Often a prominence eruption is associated with the flare. During the flare, two ribbons can be seen in H_α , hence the name. Figure 1.8 shows a coronal mass ejection, another explosive event witnessed in the solar atmosphere. CMEs are often associated with erupting prominences, and involve the rapid expulsion of plasma from the corona.

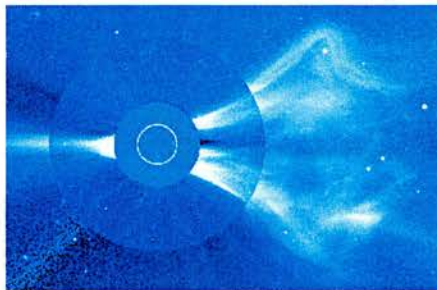


Figure 1.8: A SOHO/LASCO coronagraph of a transversely directed CME. Image courtesy of NRL.

Solar theory is very much guided by observations; as well as many ground based observatories there now exist several satellite missions dedicated to observing the Sun, for example SOHO and TRACE from which several of the images in this section are taken. For details of these and other satellite missions and the range of instrumentation, see Golub and Pasachoff (2001).

1.2 The Magnetohydrodynamic (MHD) equations

In this section, a sketch derivation of the governing MHD equations is presented. The primary focus is upon the assumptions made to facilitate a single fluid (MHD) approximation to plasma dynamics. A full derivation would consist of three parts: derivation of the moment equations, closure of the moment equations and the derivation of the MHD equations.

Starting from a microscopic level, let α denote particle species (ion or electron), and let $f_\alpha(\mathbf{x}, \mathbf{v}, t) d\mathbf{x}d\mathbf{v}$ be the probability at time t of finding particles of species α within

$d\mathbf{x}d\mathbf{v}$. The density of particle species α is given by

$$n_\alpha(\mathbf{x}, t) = \int f_\alpha(\mathbf{x}, \mathbf{v}, t) d\mathbf{v}.$$

The flow velocity $\mathbf{u}_\alpha(\mathbf{x}, t)$ is the mean velocity of all particles of species α in the volume $d\mathbf{x}$ at time t is

$$\mathbf{u}_\alpha(\mathbf{x}, t) = \frac{1}{n_\alpha(\mathbf{x}, t)} \int \mathbf{v} f_\alpha(\mathbf{x}, \mathbf{v}, t) d\mathbf{v}.$$

Since particles are neither created or destroyed, f_α obeys a continuity equation in (\mathbf{x}, \mathbf{v}) space. There are two divergence terms for flow through the surfaces of the volume element in \mathbf{x} and \mathbf{v} space,

$$\frac{\partial f}{\partial t} + \frac{\partial}{\partial \mathbf{x}} \cdot (f\mathbf{v}) + \frac{\partial}{\partial \mathbf{v}} \cdot (f\mathbf{a}) = 0, \quad (1.1)$$

where \mathbf{a} is the acceleration of particles in the volume element. Equation (1.1) can be rewritten as

$$\frac{\partial f}{\partial t} + \frac{\partial}{\partial \mathbf{x}} \cdot (f\mathbf{v}) + \frac{\mathbf{F}}{m} \cdot \frac{\partial f}{\partial \mathbf{v}} = \left(\frac{\partial f}{\partial t} \right)_c, \quad (1.2)$$

where $\mathbf{F}/m = \mathbf{a}$ and \mathbf{F} is the force acting on the particles with mass m at the point (\mathbf{x}, \mathbf{v}) at time t . The change in f with time due to collisions is represented by $(\partial f/\partial t)_c$. Equation (1.2) is called the kinetic equation. Multiplying (1.2) by some general function $\psi(\mathbf{v})$ and integrating over velocity space yields a general moment equation

$$\begin{aligned} \frac{\partial}{\partial t} (n_\alpha \langle \psi \rangle) + \frac{\partial}{\partial \mathbf{x}} \cdot (n_\alpha \langle \mathbf{v} \psi \rangle) - \frac{n_\alpha e_\alpha \mathbf{E}}{m_\alpha} \cdot \left\langle \frac{\partial \psi}{\partial \mathbf{v}} \right\rangle \\ - \frac{n_\alpha e_\alpha}{m_\alpha} \left\langle (\mathbf{v} \wedge \mathbf{B}) \cdot \frac{\partial \psi}{\partial \mathbf{v}} \right\rangle = \int \psi \left(\frac{\partial f}{\partial t} \right)_c d\mathbf{v}, \end{aligned} \quad (1.3)$$

where

$$\langle \psi \rangle = \frac{1}{n_\alpha(\mathbf{x}, t)} \int \psi(\mathbf{v}) f_\alpha(\mathbf{x}, \mathbf{v}, t) d\mathbf{v},$$

and $\mathbf{F} = e_\alpha(\mathbf{E} + \mathbf{v} \wedge \mathbf{B})$ with e_α the species charge. From (1.3) it is possible to generate evolution equations by making appropriate choices for $\psi(\mathbf{v})$.

The conditions on conservation of mass, momentum and kinetic energy during colli-

sions are

$$\int d\mathbf{v} \left(\frac{\partial f_\alpha}{\partial t} \right)_c = 0 \quad (1.4)$$

$$\sum_\alpha \int d\mathbf{v} \mathbf{v} \left(\frac{\partial f_\alpha}{\partial t} \right)_c = 0 \quad (1.5)$$

$$\sum_\alpha \frac{m_\alpha}{2} \int d\mathbf{v} v^2 \left(\frac{\partial f_\alpha}{\partial t} \right)_c = 0, \quad (1.6)$$

ie. recombination and ionisation are ignored, collisions involving just one species conserve momentum and energy.

The macroscopic single fluid variables in terms of the microscopic species variables are

$$\rho(\mathbf{x}, t) = \sum_\alpha m_\alpha n_\alpha(\mathbf{x}, t)$$

$$q(\mathbf{x}, t) = \sum_\alpha e_\alpha n_\alpha(\mathbf{x}, t)$$

$$\mathbf{u}(\mathbf{x}, t) = \frac{\sum_\alpha m_\alpha n_\alpha(\mathbf{x}, t) \mathbf{u}_\alpha(\mathbf{x}, t)}{\sum_\alpha m_\alpha n_\alpha(\mathbf{x}, t)}$$

$$\mathbf{j}(\mathbf{x}, t) = \sum_\alpha e_\alpha n_\alpha(\mathbf{x}, t) \mathbf{u}_\alpha(\mathbf{x}, t)$$

etc.

Consider the zeroth moment (taking $\psi(\mathbf{v}) = 1$ in (1.3)), multiplying by species mass then summing over species yields

$$\frac{\partial \rho}{\partial t} + \frac{\partial}{\partial \mathbf{x}} (\rho \mathbf{u}) = 0.$$

Following the same procedure but multiplying by species charge yields

$$\frac{\partial q}{\partial t} + \frac{\partial}{\partial \mathbf{x}} (\mathbf{j}) = 0.$$

Taking the first moment (setting $\psi(\mathbf{v}) = m_\alpha \mathbf{v}$ in (1.3)) and summing over species yields

$$\frac{\partial}{\partial t} (\rho u_i) + \frac{\partial}{\partial x_j} (\rho u_i u_j + P_{ij}) - q E_i - \epsilon_{ijk} j_j B_k = 0. \quad (1.7)$$

Multiplying by e_α/m_α before summing over species yields a generalised Ohm's law. The

second moment ($\psi(\mathbf{v}) = m_\alpha |\mathbf{v}|^2/2$) yields equations for the evolution of species temperature (T_α). These equations are simplified slightly by taking the limit $m_e/m_i \rightarrow 0$ - i.e. the ratio of electron to ion mass is small - and $|q| \ll en_e$ which is a consequence of charge neutrality. This set of equations is not closed, and cannot be closed by generating higher moment equations.

The truncation and closure of the infinite chain of moment equations is based upon an analysis of the timescales that characterise the plasma dynamics. A full investigation of this analysis is beyond the remit of this section, which is confined to outlining the assumptions made to move towards a single fluid description of a plasma. First, assume \mathbf{E} and \mathbf{B} vary over the same timescale as the hydrodynamic variables (ρ , \mathbf{u} , T_α etc.). That is, field fluctuations arise from plasma motion or *vice versa*. This implies neglecting the displacement current and Gauss' law in Maxwell's equations, which become

$$\nabla \wedge \mathbf{E} = -\frac{\partial \mathbf{B}}{\partial t}, \quad (1.8)$$

$$\nabla \wedge \mathbf{B} = \mu_0 \mathbf{j}, \quad (1.9)$$

$$\nabla \cdot \mathbf{B} = 0, \quad (1.10)$$

where $\mu_0 = 1.257 * 10^{-6} H/m$ is the vacuum permeability, $\epsilon_0 = 8.854 * 10^{-12} F/m$ is the vacuum permittivity. Next, assume that the collisional relaxation time for each species is much smaller than the timescale for hydrodynamic variations - $\tau_\alpha \ll \tau_H$. This implies that ion and electron populations will approach a local Maxwellian distribution ($f_{\alpha,0}$) over the short timescale τ_α . The distribution function (f_α) can be rewritten as a deviation from $f_{\alpha,0}$. The expansion of this form of f_α can be truncated at various levels (Balescu and Paiva-Veretennicoff (1978), Xiaoming and Balescu (1982)). Although the exchange of momentum between species (\mathbf{R}) cancels in (1.7) due to (1.5), collision terms such as \mathbf{R} still appear in the generalised Ohm's law and higher order moment equations, these terms must also be expanded. For example

$$\mathbf{R}_e = \frac{m_e}{\tau_e} \left(\frac{\mathbf{j}}{e} + \dots \right) = -\mathbf{R}_i.$$

The transport equations from Boyd and Sanderson (2003) are

$$j_k = \sigma_{kl} \hat{E}_l - \alpha_{kl} \frac{\partial T_e}{\partial x_l}$$

$$q_{k,e} = \alpha_{kl} T_e \hat{E}_l - \kappa_{kl,e} \frac{\partial T_e}{\partial x_l}$$

$$q_{k,i} = -\kappa_{kl,i} \frac{\partial T_i}{\partial x_l}$$

where the effective electric field is

$$\hat{E}_i = E_i + \epsilon_{ijk} u_j B_k + \frac{1}{en_e} \frac{\partial}{\partial x_i} (n_e T_e),$$

and where σ_{kl} represents electrical conductivity, α_{kl} is the thermoelectric coefficient and $\kappa_{kl,\alpha}$ is the species thermal conductivity. This system can be simplified by discovering relationships between the transport coefficients for particular configurations, see for example Braginskii (1965). Substituting the transport equations and collision terms into the moment equations yields, after a little manipulation

$$\frac{\partial \rho}{\partial t} = -\nabla \cdot (\rho \mathbf{u}), \quad (1.11)$$

$$\frac{\partial}{\partial t} (\rho \mathbf{u}) = -\nabla \cdot (\rho \mathbf{u} \mathbf{u} + P \mathbf{I}) + \mathbf{j} \wedge \mathbf{B} + [DISS], \quad (1.12)$$

$$\frac{\partial T_\alpha}{\partial t} = -\mathbf{u} \cdot \nabla T_\alpha - \frac{2}{3} T_\alpha \nabla \cdot \mathbf{u} + [DISS], \quad (1.13)$$

$$\frac{\partial P}{\partial t} = -\mathbf{u} \cdot \nabla P - \frac{5}{3} P \nabla \cdot \mathbf{u} + [DISS], \quad (1.14)$$

where $[DISS]$ represents the dissipative terms, \mathbf{I} is the unit dyadic and P is the scalar pressure. All of the dissipative terms are of order τ_α/τ_H or higher, whereas all of the hydrodynamic terms are of order 1. Neglecting all of the dissipative terms except electrical resistivity implies

$$\alpha_{kl} = \kappa_{kl,\alpha} = \mu_{p,\alpha} = 0, \quad (1.15)$$

where $\mu_{p,\alpha}$ is the viscosity. This is achieved in the following limit

$$|\omega_\alpha \tau_\alpha| \rightarrow \infty, \quad T_\alpha \rightarrow 0,$$

where ω_α is the particle Larmor frequency. Since $\tau_\alpha \propto T_\alpha^{3/2}/n_\alpha$ this limit is valid for low pressure plasmas in a strong magnetic field. After making these simplifications, the generalised Ohm's law reduces to

$$\frac{m_e}{\tau_e} \mathbf{j} + e \mathbf{j} \wedge \mathbf{B} = e^2 n_e (\mathbf{E} + \mathbf{u} \wedge \mathbf{B}) + e \nabla (n_e T_e). \quad (1.16)$$

Assuming the ion Larmor radius is smaller than the hydrodynamic length scale ($r_{Li} \ll$

L_H) and $|\mathbf{j}| \ll en_e|\mathbf{u}|$ which is reasonable since $|\mathbf{j}| \sim O(1)$, $n_e, \mathbf{u} \sim O(\tau_\alpha/\tau_H)$, then (1.16) reduces to

$$\mathbf{j} = \frac{e^2 n_e \tau_e}{m_e} (\mathbf{E} + \mathbf{u} \wedge \mathbf{B}) = \sigma_{\parallel} (\mathbf{E} + \mathbf{u} \wedge \mathbf{B}). \quad (1.17)$$

Applying (1.15), (1.17) and (1.8)-(1.10) to (1.11)-(1.14) yields the closed single fluid MHD approximation,

$$\frac{\partial \rho}{\partial t} = -\nabla \cdot (\rho \mathbf{u}), \quad (1.18)$$

$$\rho \frac{\partial \mathbf{u}}{\partial t} + \rho (\mathbf{u} \cdot \nabla) \mathbf{u} = -\nabla P + \frac{1}{\mu_0} (\nabla \wedge \mathbf{B}) \wedge \mathbf{B}, \quad (1.19)$$

$$\frac{\partial P}{\partial t} + (\mathbf{u} \cdot \nabla) P = -\frac{5}{3} P \nabla \cdot \mathbf{u} + \frac{2}{3 \sigma_{\parallel} \mu_0^2} (\nabla \wedge \mathbf{B})^2, \quad (1.20)$$

$$\frac{\partial \mathbf{B}}{\partial t} = \nabla \wedge (\mathbf{u} \wedge \mathbf{B}) - \nabla \wedge \left(\frac{1}{\sigma_{\parallel} \mu_0} \nabla \wedge \mathbf{B} \right), \quad (1.21)$$

$$\nabla \cdot \mathbf{B} = 0. \quad (1.22)$$

A standard notation is to use $\eta = 1/\mu_0 \sigma_{\parallel}$ for resistivity. Equations (1.18)-(1.22) represent an ideal gas with $\gamma = 5/3$.

The ideal MHD equations which possess no dissipative mechanisms (ie. $\eta = 0$), are simply

$$\frac{\partial \rho}{\partial t} = -\nabla \cdot (\rho \mathbf{u}), \quad (1.23)$$

$$\rho \frac{\partial \mathbf{u}}{\partial t} + \rho (\mathbf{u} \cdot \nabla) \mathbf{u} = -\nabla P + \frac{1}{\mu_0} (\nabla \wedge \mathbf{B}) \wedge \mathbf{B}, \quad (1.24)$$

$$\frac{\partial P}{\partial t} + (\mathbf{u} \cdot \nabla) P = -\frac{5}{3} P \nabla \cdot \mathbf{u}, \quad (1.25)$$

$$\frac{\partial \mathbf{B}}{\partial t} = \nabla \wedge (\mathbf{u} \wedge \mathbf{B}), \quad (1.26)$$

$$\nabla \cdot \mathbf{B} = 0. \quad (1.27)$$

1.3 Aspects of Linear Wave Theory

For an ideal gas, compressional waves are propagated isotropically with the sound speed

$$c_s = \left(\frac{\gamma P_0}{\rho_0} \right)^{1/2}, \quad (1.28)$$

where P_0 and ρ_0 are the undisturbed pressure and density respectively, γ is the ratio of specific heat. In an ideal magnetised plasma, variations in gas pressure will disturb the magnetic field, waves can propagate at the speed c_s only in the direction parallel to the magnetic field. The directionality of the magnetic field makes wave propagation anisotropic.

The characteristic speed for the propagation of magnetic disturbances is the Alfvén speed

$$v_A = \frac{B_0}{\sqrt{\mu_0 \rho_0}}. \quad (1.29)$$

where μ_0 is the permeability of free space and B_0 is the undisturbed magnetic field strength. The ratio of gas pressure to magnetic pressure is known as the plasma beta

$$\beta = \frac{P_0}{B_0^2/2\mu_0} = \frac{2 c_s^2}{\gamma v_A^2}. \quad (1.30)$$

This acts as a guide to the importance of the magnetic forces to the thermal pressure force. For an ideal plasma, Alfvén's theorem applies (ie. plasma is frozen to the magnetic field). So, for $\beta \gg 1$ the flow responds to the pressure gradient and drags the magnetic field-lines with it, conversely for $\beta \ll 1$ the flow is severely restricted by the magnetic field. The value of β is considered large in the solar interior, becoming small with the rapid decrease in gas pressure in the solar atmosphere.

Useful combinations of the defined speeds are

$$c_f^2 = c_s^2 + v_A^2 \quad (1.31)$$

$$c_T^{-2} = c_s^{-2} + v_A^{-2}, \quad (1.32)$$

where c_f is known as the fast speed for perpendicular propagation (super-Alfvénic, supersonic), c_T is known as the tube or slow speed (sub-Alfvénic, subsonic).

This discussion is limited to linear waves, for a discussion of some aspects of non-linear waves see Nakariakov et al. (1998). The ideal MHD equations (1.23)-(1.26) are linearised by setting $f = f_0 + \delta f_1$ for $f = \rho, \mathbf{u}, P, \mathbf{B}$ noting that $\mathbf{u}_0 = 0$. The resulting equations are

$$\frac{\partial \rho_1}{\partial t} = \nabla \cdot (\rho_0 \mathbf{u}_1) = 0, \quad (1.33)$$

$$\rho_0 \frac{\partial \mathbf{u}_1}{\partial t} = \nabla P_1 + \frac{1}{\mu_0} (\nabla \wedge \mathbf{B}_1) \wedge \mathbf{B}_0, \quad (1.34)$$

$$\frac{\partial P_1}{\partial t} = -(\mathbf{u}_1 \cdot \nabla) P_0 - \gamma P_0 \nabla \cdot \mathbf{u}_1, \quad (1.35)$$

$$\frac{\partial \mathbf{B}_1}{\partial t} = (\mathbf{B}_0 \cdot \nabla) \mathbf{u}_1 - \mathbf{B}_0 \cdot (\nabla \cdot \mathbf{u}_1). \quad (1.36)$$

Assuming a uniform plasma ($\rho_0, P_0, \mathbf{B}_0$ all constant) and performing a Fourier analysis (ie. seek solutions of the form $f(\mathbf{x}, t) = \Re(f'(\mathbf{x}, t)e^{i(\mathbf{k} \cdot \mathbf{x} - \omega t)})$ for $v = \rho_1, \mathbf{u}_1, P_1, \mathbf{B}_1$), yields the following dispersion relation

$$(\omega^2 - (\mathbf{k} \cdot \mathbf{v}_A)^2) (\omega^4 - c_f^2 k^2 \omega^2 + k^2 c_s^2 (\mathbf{k} \cdot \mathbf{v}_A)^2) = 0, \quad (1.37)$$

where \mathbf{k} is the wave number, ω is the frequency and $k = |\mathbf{k}|$. For linear waves in a non-uniform medium see Roberts (1991).

Alfvén waves have the dispersion relation

$$\omega^2 = (\mathbf{k} \cdot \mathbf{v}_A)^2, \quad (1.38)$$

which stems from $\mathbf{k} \cdot \mathbf{u}' = \mathbf{v}_A \cdot \mathbf{u}' = P' = 0$ in (1.37), that is an incompressible disturbance, with velocity and magnetic perturbations normal to the plane containing \mathbf{k} and \mathbf{v}_A .

Magnetoacoustic waves satisfy

$$\omega^4 - c_f^2 k^2 \omega^2 + k^2 c_s^2 (\mathbf{k} \cdot \mathbf{v}_A)^2 = 0, \quad (1.39)$$

which is the case provided $\mathbf{B}_0 \cdot (\mathbf{k} \wedge \mathbf{u}') = \mathbf{v}_A \cdot (\mathbf{k} \wedge \mathbf{B}') = 0$ in (1.37), that is velocity and magnetic perturbations lie in the plane containing \mathbf{k} and \mathbf{v}_A . The two solutions for the quadratic in ω^2 are

$$\omega^2 = \frac{k^2 c_f^2}{2} \left(1 \pm \sqrt{1 - \frac{4c_s^2 (\mathbf{k} \cdot \mathbf{v}_A)^2}{k^2 c_f^4}} \right). \quad (1.40)$$

It can be seen that $\omega_s \leq \omega_A \leq \omega_f$ where $\omega_{s,f}$ are the slow and fast frequencies corresponding to using the plus and minus signs in (1.40) respectively. These waves are compressional and are known as the slow and fast magnetoacoustic waves. These modes decouple when propagating either parallel or perpendicular to the background field, B_0 .

For perpendicular propagation $\mathbf{k} \cdot \mathbf{v}_A = 0$ and the fast wave is given by

$$\omega_f^2 = k^2 c_f^2, \quad (1.41)$$

$B' \parallel B_0$ so the compression of the magnetic field combines with the thermal pressure to drive the wave. The slow mode does not propagate perpendicular to the magnetic field and $\omega_s = 0$ in this case.

For parallel propagation $\mathbf{k} \cdot \mathbf{v}_A = k_{\parallel} v_A$, one mode has $\omega = k_{\parallel} v_A$ (Alfvén wave), the other has $\omega = k_{\parallel} c_s$ (acoustic wave). Which of these is slow and which is fast is dependent upon β . For $\beta \ll 1$ the acoustic wave is slow, the Alfvén wave is fast. The acoustic mode is driven by variations in thermal pressure, and is only guided by the magnetic field. The Alfvén wave is independent of plasma compressibility ($\nabla \cdot \mathbf{u}' = 0$).

For propagation at an arbitrary angle, the fast and slow modes will have contributions from the components of velocity perpendicular and parallel to the magnetic field. For $\beta \ll 1$ the fast mode propagates almost perpendicular to B_0 whereas the slow mode propagates almost parallel to B_0 .

1.4 Aspects of Magnetic Reconnection

In this section, outlines of two classical two-dimensional reconnection mechanisms are presented to give a flavour of the reconnection process. For details of more advanced reconnection methods including three-dimensional reconnection away from null points, see Priest and Forbes (2000). Magnetic reconnection reconfigures the magnetic topology, converts energy stored in the magnetic field into thermal and kinetic energy, and accelerates particles.

The first reconnection mechanism outlined is that proposed by Sweet (1958) and Parker (1963). This mechanism is steady (ie. advection of magnetic field-lines into the diffusion region equals the diffusion rate), incompressible, and the external magnetic field

is constant, so the reconnection rate is constant and equivalent to the rate of inflow of magnetic field. The dimensionless reconnection rate is given by the inflow Alfvén Mach number

$$M_{Ai} = \frac{u_i}{v_{Ai}} \text{ where } v_{Ai} = \frac{B_i}{\sqrt{\mu_0 \rho}}.$$

In this section the subscript i denotes inflow values and o denotes outflow values. The diffusion region has dimensions $2L$ by $2l$ as indicated in Figure 1.9. The induction equation implies

$$u_i = \eta/l, \tag{1.42}$$

and conservation of mass implies

$$Lu_i = lu_o. \tag{1.43}$$

The steady version of equation (1.8) implies \mathbf{E} is constant and so equation (1.17) gives

$$u_i B_i = u_o B_o. \tag{1.44}$$

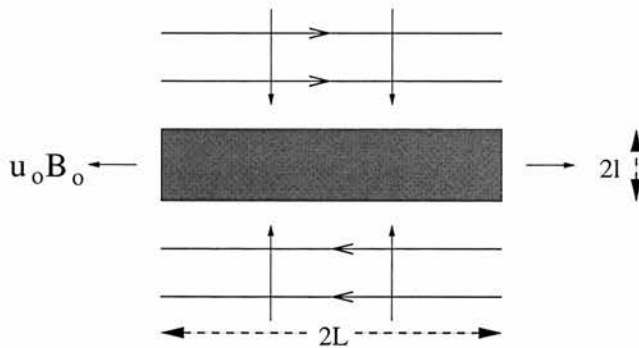


Figure 1.9: Sweet-Parker diffusion region with oppositely directed magnetic fields.

Equation (1.9) then implies

$$j_z = \frac{B_i}{l\mu_0}, \tag{1.45}$$

and the solenoidal condition gives

$$\frac{B_i}{L} = \frac{B_o}{l}. \quad (1.46)$$

The momentum equation in the x-direction is

$$\rho(\mathbf{u} \cdot \nabla)u_x = -\frac{\partial P}{\partial x} + j_z B_y, \quad (1.47)$$

neglecting thermal pressure and substituting (1.45) yields

$$\rho \left(\frac{u_o}{L} \right) u_o = \frac{B_i}{l\mu_0} \frac{lB_i}{L} \Rightarrow u_o^2 = \frac{B_i^2}{\mu_0\rho} = v_{Ai}^2. \quad (1.48)$$

Eliminating l from (1.42) and (1.43) gives

$$u_i^2 = \frac{\eta}{L} u_o.$$

Thus, the dimensionless reconnection rate is

$$M_{Ai} = \frac{u_i}{v_{Ai}} = \frac{\sqrt{\eta v_{Ai}/L}}{v_{Ai}} = \frac{1}{\sqrt{R_{Mi}}},$$

where $R_{Mi} = Lv_{Ai}/\eta$. In the corona $R_M \approx 10^{12}$ giving $M_A \approx 10^{-6}$. This is too slow to explain solar flares for example, so faster reconnection methods are sought.

A faster reconnection mechanism was proposed by Petschek (1964). In addition to the diffusion region and external field of the Sweet-Parker model, the immediate field surrounding the diffusion region is also considered. The diffusion region occupies a small proportion of the area under consideration, slow magnetoacoustic shocks are also present and indicated in Figure 1.10. These shocks contribute to the conversion of magnetic energy into heat and kinetic energy.

A full analysis of the Petschek reconnection mechanism is quite involved and beyond the remit of this section. A more rigorous analysis of a Petschek-like reconnection mechanism is given in Soward and Priest (1982). The reconnection rate is inversely proportional to the size of the diffusion region. Petschek suggested that the lower limit for the size of the diffusion region is achieved when $B_o = B_i/2$. The maximum reconnection

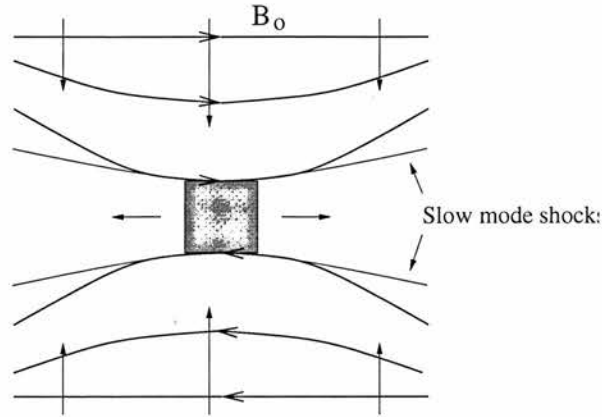


Figure 1.10: Petschek reconnection region, the diffusion region is shaded.

rate is given by

$$M_{Ai} \approx \frac{\pi}{8 \log R_{mi}}.$$

1.5 Numerical basics

This section provides a brief introduction to some numerical techniques used to solve systems of partial differential equations. There are a large number of possible approaches and this section will only concern itself with the more basic approaches.

Consider a set of sample points $[x_0, \dots, x_N]$ in the domain of some function $f(x)$. The *samples* $f_i = f(x_i)$ represent the function $f(x)$ at the sample points x_i . The spacing between samples is $\delta x_i = x_i - x_{i-1}$. If the sample spacing is constant, then $\delta x = (x_N - x_0)/N$. The sample spacing must be small enough to accurately represent the original function, otherwise difficulties such as aliasing (see Figure 1.11) can occur. The sample spacing is permitted to vary, however there are requirements on the smoothness of such a variation and such spacings shall not be discussed here.

Finite difference methods use *samples* to solve differential equations, since differential equations are pointwise. Derivatives are approximated by finite difference formulae which simply use the *samples*. For example

$$f(x) = \frac{\partial u}{\partial x} \Big|_{i,n} = \frac{U_{i+1}^n - U_i^n}{\delta x}$$

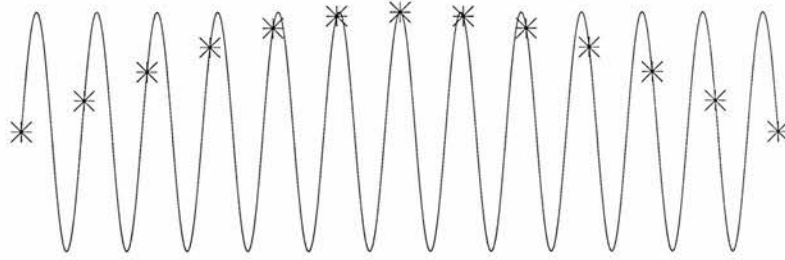


Figure 1.11: Example of aliasing: both the function and the samples vary sinusoidally, but the samples possess a longer wavelength.

where U_i is the sample of u . For a comprehensive list of such approximations, see Abramowitz and Stegun (1965). To construct finite difference approximations to derivatives involves converting the samples into a functional representation via, for example, interpolation or Taylor series expansion. For example, to construct a first order approximation linear interpolation is used, ie. a polynomial passing through two *samples* is created

$$p_1(x) = U_i + \frac{U_{i+1} - U_i}{x_{i+1} - x_i}(x - x_i),$$

then

$$\frac{\partial u}{\partial x} \approx \frac{\partial p_1}{\partial x} = \frac{U_{i+1} - U_i}{x_{i+1} - x_i}.$$

By differentiating quadratics, cubics and higher order interpolation polynomials p_n , one can obtain higher order approximations and higher order derivatives. Simply substituting chosen finite difference approximations to derivatives into a differential equation will often fail to create a stable scheme. Linear stability will be discussed briefly in a following subsection.

Closely related to finite difference methods are finite volume methods which use cell integral averages rather than samples, where the cell width is the sample spacing. However, cell centred samples equal cell integral averages to within second order in one dimension,

$$\frac{1}{\delta x_i} \int_{x_{i-1/2}}^{x_{i+1/2}} f(x) dx = f(x_i) + O(\delta x^2),$$

where $x = x_{i+1/2}$ is the cell edge.

Finite element methods carry piecewise polynomial coefficients for each cell rather

than samples, and do not necessarily need to reconstruct $f(x)$. Finite element methods will not be considered for the remainder of this thesis.

Consider the simple one dimensional linear advection equation,

$$\frac{\partial u}{\partial t} + a \frac{\partial u}{\partial x} = 0. \quad (1.49)$$

Let space be divided into cells $[x_{i-1/2}, x_{i+1/2}]$ and time divided into intervals $[t^n, t^{n+1}]$ where t^n is called a time level. An example of a simple discretisation of (1.49) is

$$U_i^{n+1} = U_i^n - \frac{a}{2} \frac{\delta t}{\delta x} (U_{i+1}^n - U_{i-1}^n), \quad (1.50)$$

where $\delta x = x_{i+1/2} - x_{i-1/2}$, $\delta t = t^{n+1} - t^n$. Equation (1.50) describes a timestep from time level n to time level $n + 1$. Starting from initial conditions, such a scheme can *time march* to any desired time, restricted only by the number of timesteps. In an implicit method, the unknown solution at time level $n + 1$ depends on itself or on unknown solutions at later time levels, ie.

$$U_i^{n+1} = U(U_{i-K_1}^n, \dots, U_{i+K_2}^n, U_{i-L_1}^{n+1}, \dots, U_{i+L_2}^{n+1}).$$

In an explicit method the unknown solution at time level $n + 1$ depends on known solutions at time level n or earlier. Although implicit methods are more computationally expensive per timestep than explicit methods, stability conditions, yet to be discussed, permit implicit methods to possess larger timesteps. It is therefore possible for an implicit method to be more efficient than an explicit method. For hyperbolic systems of PDEs - such as the ideal gas laws, ideal MHD - explicit methods are more efficient. Only explicit methods shall be considered from hereon in. The numerical domain of dependence of the unknown solution is called the stencil, which are often illustrated as in Figure 1.12.

1.5.1 Linear stability theory

In this section a very brief overview of the linear theory is given. This develops some of the key concepts including consistency, convergence and stability.

The aim is to know how well U_i^n approximates the true solution. For smooth solutions

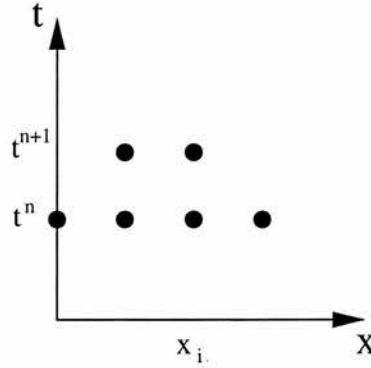


Figure 1.12: An example of an implicit stencil.

we define the *global error* to be

$$E_i^n = U_i^n - u_i^n,$$

where $u_i^n = u(x_i, t^n)$. The method *converges* if

$$\|E_{\delta t}(\cdot, t)\| \rightarrow 0 \text{ as } \delta t \rightarrow 0,$$

for some norm, for any fixed $t \geq 0$, for all initial data. We can estimate the global error from the Local Truncation Error (LTE) and some stability analysis. The LTE is defined as

$$L_{\delta t} = \frac{1}{\delta t} (u(x, t + \delta t) - H_{\delta t}(u(\cdot, t); x)),$$

where $H_{\delta t}$ is an operator such that $U_i^{n+1} = H_{\delta t}(U_i^n)$.

In order to define linear stability, a few definitions are needed. Briefly, the method is *consistent* if $\|L_{\delta t}(\cdot, t)\| \rightarrow 0$ as $\delta t \rightarrow 0$. The method is of *order* p if for all sufficiently smooth initial data there exists a constant C_L such that

$$\|L_{\delta t}(\cdot, t)\| < C_L \delta t^p \quad \forall \delta t < \delta t_0, \quad t \leq T.$$

The solution to the PDE can be written

$$u(x, t + \delta t) = H_{\delta t}(u(\cdot, t); x) + \delta t L_{\delta t}(x, t),$$

and the error is

$$E_{\delta t}(\cdot, t_n) = \underbrace{H_{\delta t} E_{\delta t}(\cdot, t)}_{[1]} - \underbrace{\delta t L_{\delta t}(\cdot, t)}_{[2]}.$$

[1]: cumulative error from previous steps.

[2]: new local error introduced at this timestep.

Applying this relationship recursively yields

$$E_{\delta t}(\cdot, t_n) = H_{\delta t}^n E_{\delta t}(\cdot, 0) - \delta t \sum_{l=1}^n H_{\delta t}^{n-l} L_{\delta t}(\cdot, t_{l-1}).$$

To obtain a bound on the global error, we must ensure that the LTE is not unduly amplified by applying $n - i$ steps of the method, ie. the method must be stable. A method is *stable* if, for each time T , there exists a constant C_S and value $\delta t_0 > 0$ such that

$$\|H_{\delta t}^n\| \leq C_S \quad \forall n\delta t \leq T, \quad \delta t < \delta t_0.$$

The *Lax Equivalence Theorem* states that for a consistent linear method, stability is necessary and sufficient for convergence of linear equations.

It should be noted that some finite different schemes are inherently unstable. An example of this is given in the next subsection.

The CFL condition

The CFL condition is a necessary but not sufficient condition for stability. This condition states that the domain of dependence of the finite difference method should completely include the domain of dependence of the PDE.

The solution at a fixed point in space and time (\bar{x}, \bar{t}) is determined by the initial data within some finite distance of \bar{x} . The size of this set usually increases with \bar{t} , but we have a bound on this set

$$D \subset \{x : |x - \bar{x}| < a_{max} \bar{t}\} \quad \text{for some } a_{max},$$

which is the domain of dependence for the PDE. This states that hyperbolic equations

have a finite propagation speed, information can travel with speed at most a_{max} .

The domain of dependence of a finite difference scheme is the set of points x for which the initial data $u_0(x)$ could possibly affect the solution at some fixed point (\bar{x}, \bar{t}) .

A numerical method which violates the CFL condition fails to use information that affects the true solution. If this missing information is important the numerical solution will deviate substantially from the true solution, or worse still the numerical solution will tend to infinity, ie. become unstable.

A scheme's stencil can be adjustable. That is, the numerical domain of dependence should model the physical domain of dependence as closely as possible. For example, the physical domain of dependence is entirely *upwind*, ie. the physical domain of dependence lies to the right for left-running waves, and to the left of right-running waves in one dimension. *Upwind* stencils model this physical behaviour by selecting only upwind samples.

1.5.2 Some basic schemes

If one were to simply substitute finite difference approximations to derivatives into a PDE to create a finite difference scheme, there is no guarantee that it will be stable. For example, if one were to choose a first order forward difference in time, and a centred difference in space to model the advection equation (1.49), the result is given in Figure 1.13.

Forward Time Centred Space (FTCS) is an inherently unstable scheme even if the CFL condition is met. It is possible to realise this analytically by performing a von Neumann decomposition. Essentially this seeks solutions of the form $\lambda^n e^{im\delta x}$ which stems from separating variables. Note that this assumes a periodic solution and that the grid is uniform. The condition $|\lambda| \leq 1$ is necessary for stability. For this problem one would find

$$|\lambda| = \left(1 + \left(\frac{a\delta t}{\delta x} \right)^2 \sin^2(m\delta x) \right)^{1/2} > 1 \quad \forall \delta x, \delta t.$$

Some basic schemes can be derived simply by substituting finite difference approx-

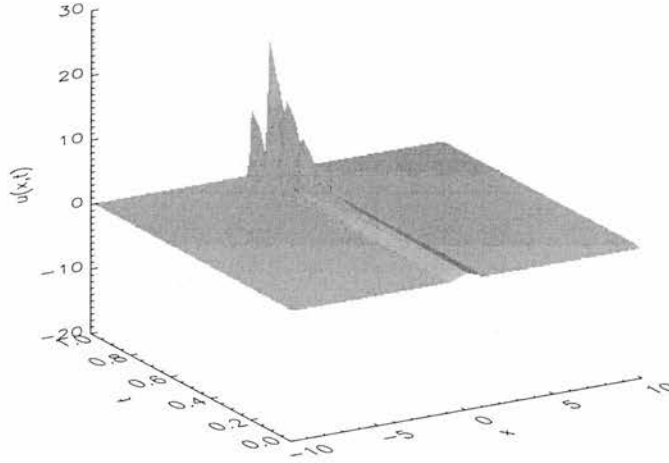


Figure 1.13: Simulation of the advection equation using FTCS with 1000 grid points.

imations to derivatives into the differential equation (eg. FTCS). More complex schemes can be derived with reasonable ease. For example, to derive the Lax Wendroff scheme, apply a Taylor expansion to $u(x, t + \delta t)$, substitute for the first and second derivatives in t with derivatives in x formed from the governing PDE. Discretize the system using centred differences. This is a specific form of the Cauchy-Kowalewski technique, which is also used to derive the Beam-Warming scheme. Note that the Lax Wendroff and Beam-Warming methods are entire classes of methods differing only in the choice of the average wave speed $a_{j+1/2}^n$ where $a(u) = \partial f / \partial u$. Some simple choices are

$$a_{i+1/2}^n = a\left(\frac{U_{i+1}^n + U_i^n}{2}\right) \quad \text{or} \quad a_{i+1/2}^n = \frac{a(U_{i+1}^n) + a(U_i^n)}{2},$$

or more simply

$$a_{i+1/2}^n = \begin{cases} \frac{f(U_{i+1}^n) - f(U_i^n)}{U_{i+1}^n - U_i^n} & U_i^n \neq U_{i+1}^n, \\ a(U_i^n) & U_i^n = U_{i+1}^n, \end{cases}$$

where f is the flux function from (1.51) For complete derivations of many such schemes see Laney (1998).

The MacCormack scheme

The MacCormack scheme is a predictor-corrector variant of the Lax Wendroff method which is especially popular because of the ease with which it can be implemented. It is defined for the scalar conservative law

$$\frac{\partial u}{\partial t} + \frac{\partial}{\partial x} f(u) = 0 \quad (1.51)$$

as

$$\begin{aligned} \tilde{U}_i &= U_i^n - \frac{\delta t}{\delta x} (f(U_{i+1}^n) - f(U_i^n)) \\ U_i^{n+1} &= \frac{1}{2} (U_i^n + \tilde{U}_i) - \frac{\delta t}{2\delta x} (f(\tilde{U}_i) - f(\tilde{U}_{i-1})). \end{aligned}$$

The MacCormack method can be rewritten

$$\begin{aligned} \tilde{U}_i &= U_i^n - \frac{\delta t}{\delta x} (f(U_{i+1}^n) - f(U_i^n)) \\ \bar{U}_i &= \tilde{U}_i - \frac{\delta t}{2\delta x} (f(\tilde{U}_i) - f(\tilde{U}_{i-1})) \\ U_i^{n+1} &= \frac{1}{2} (\tilde{U}_i + \bar{U}_i), \end{aligned}$$

where the predictor is Forward Time Forward Space (FTFS) and the corrector is Forward Time Backward Space (FTBS). Left-running waves are captured well with this form, right-running waves are captured better if the predictor and corrector steps are reversed. To avoid favouring either left or right-running waves the order of FTFS and FTBS are alternated after each timestep, this is an example of an adaptive stencil.

Lax Wendroff methods were not designed for problems containing jump discontinuities. A discussion of methods to enable a scheme to deal with such discontinuities is reserved for a later chapter.

1.5.3 Demonstration of numerical dissipation and dispersion

Numerical methods will incur some form of error due to the truncation error of the scheme. Here the types of error for first and second order schemes (which are indicative of higher order schemes) are presented. To demonstrate these errors, simulations of

the advection equation (1.49) are made. Choosing

$$\text{Initial conditions : } u(x, 0) = \begin{cases} 1 - |x| & |x| < 1 \\ 0 & |x| \geq 1 \end{cases}$$

$$\text{Range : } -10 \leq x \leq 10,$$

the exact solution using the method of characteristics is

$$u(x, t) = \begin{cases} 1 - |x - at| & |x - at| < 1 \\ 0 & |x - at| \geq 1 \end{cases},$$

which is represented graphically in Figure 1.14 with $a = 1/2$.

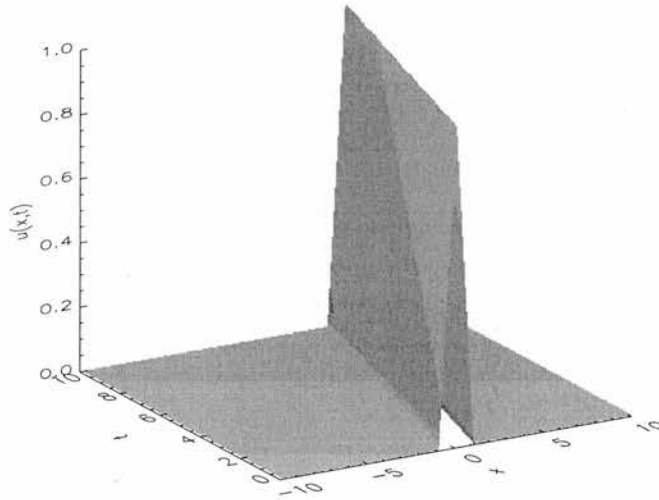


Figure 1.14: Exact solution of the advection problem.

The FTBS method is a first order accurate method and is stable if the CFL condition is satisfied. FTBS is an Upwind method when $a > 0$, the domain of dependence of an Upwind scheme closely models the physical domain of dependence so Upwind methods are quite accurate.

The solution using the FTBS scheme translates at the correct speed, but also diffuses (see Figure 1.15). Instead of doing a LTE analysis, a modified PDE is sought, ie. can one find a PDE that is better satisfied by U_i^n than the original PDE modelled? Let $v(x, t)$ be a

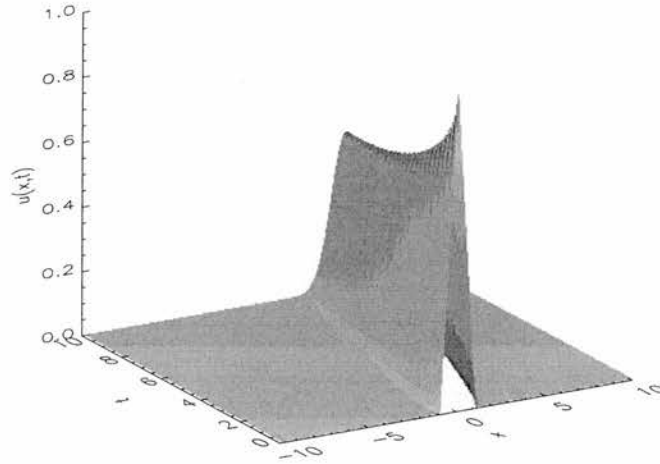


Figure 1.15: 1st order diffusive simulation of the advection equation, with uniform grid spacing $\delta x = 0.2$.

function that agrees exactly with U_i^n at the grid points, so unlike $u(x, t)$, $v(x, t)$ satisfies the difference equation exactly:

$$v(x, t + \delta t) = v(x, t) - \frac{a\delta t}{\delta x}(v(x, t) - v(x - \delta x, t)).$$

Expanding these terms in Taylor series about (x, t) and rearranging yields

$$\frac{\partial v}{\partial t} + a \frac{\partial v}{\partial x} = \frac{1}{2} a \delta x \left(1 - \frac{a\delta t}{\delta x} \right) \frac{\partial^2 v}{\partial x^2} + O(\delta t^2).$$

The modified PDE is an Advection-Diffusion equation. The values U_i^n give a second order accurate approximation to this Advection-Diffusion equation, whilst only a first order accurate approximation to the Advection equation. The diffusion coefficient vanishes for the case $a\delta t = \delta x$, and a higher order approximation is achieved. The diffusion coefficient is positive only if $0 < a\delta t/\delta x < 1$. This is the stability limit for the Upwind scheme. If the diffusion coefficient is negative, this gives an ill-posed problem with exponentially growing solutions.

The Lax-Wendroff method is a second order accurate method and is stable if the CFL condition is satisfied.

The modified equation is

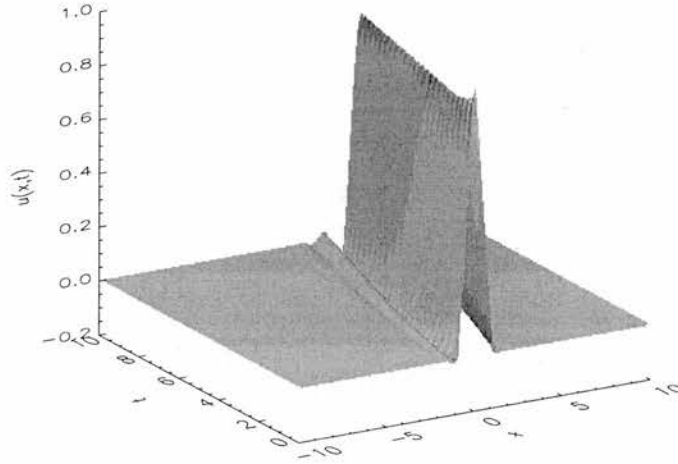


Figure 1.16: 2nd order dispersive simulation of the advection equation, with uniform grid spacing $\delta x = 0.2$.

$$\frac{\partial v}{\partial t} + a \frac{\partial v}{\partial x} = -\frac{1}{6} a \delta x^2 \left(1 - \left(\frac{a \delta t}{\delta x} \right)^2 \right) \frac{\partial^3 v}{\partial x^3} + O(\delta t^3).$$

The Lax Wendroff scheme produces a third order accurate solution to this equation. The v_{xxx} term leads to dispersive behaviour, ie. an oscillating solution plus a phase error (see Figure 1.16). The magnitude of the error is smaller than that from the Upwind method for fixed δx , δt . The group velocity for the modified PDE is

$$c_g = a - \frac{1}{2} a \delta x^2 \left(1 - \left(\frac{a \delta t}{\delta x} \right)^2 \right) k^2.$$

Since $c_g < a \forall \delta t$, one can expect the numerical result to develop a train of oscillations behind the main peak, with high wave numbers lagging furthest behind the correct solution. If one more term in the modified equation is retained, U_i^n is a fourth order accurate solution to

$$\frac{\partial v}{\partial t} + a \frac{\partial v}{\partial x} = \frac{1}{6} a \delta x^2 \left(\left(\frac{a \delta t}{\delta x} \right)^2 - 1 \right) \frac{\partial^3 v}{\partial x^3} - \epsilon \frac{\partial^4 v}{\partial x^4} + O(\delta t^4),$$

where ϵ is $O(\delta x^3)$ and positive. This higher order dissipation causes the highest wave numbers to be damped, so there is a limit to the oscillations seen.

1.5.4 Discontinuities

Simple finite difference methods are adequate for smooth functions. However, flows in ideal gas and MHD can contain non-differentiable jump discontinuities such as contact discontinuities and shocks. Either a discretisation of the appropriate integral form of the governing equations, or weak solutions of the system of PDE's are sought. Weak solutions are not unique, satisfying the entropy condition effectively selects the correct weak solution. One form of the entropy condition in one dimension is

$$\frac{\partial(\rho s)}{\partial t} + \frac{\partial(\rho u s)}{\partial x} > 0,$$

where s is the specific entropy and u is the velocity.

A shock wave is a jump discontinuity satisfying the following Rankine-Hugoniot relationship,

$$\mathbf{f}_R - \mathbf{f}_L = S(\mathbf{u}_R - \mathbf{u}_L) \tag{1.52}$$

where \mathbf{u} is a conserved variable, \mathbf{f} is its flux function and S is the shock speed. Subscripts R and L denote regions to the right and left of the discontinuity respectively. Shocks must satisfy

$$u_L + c_{s,L} \geq S \geq u_R + c_{s,R}. \tag{1.53}$$

Smooth solutions automatically satisfy the second law of thermodynamics, however (1.53) is required to satisfy this law across shocks. The results of applying (1.52) to the ideal gas equations is shown in appendix A. In MHD, just as there are fast and slow magnetoacoustic waves, so there are fast and slow shock waves.

Contact discontinuities occur when the wave speed and total pressure are continuous, whilst other flow properties jump. Fluid does not pass through a contact, rather the discontinuity moves with the flow. Entropy can change across a contact, however contacts cannot create entropy like shocks, a contact discontinuity merely separates regions of different entropy. Density, entropy and energy may increase or decrease across a contact, unlike with shocks. Both shocks and contact discontinuities obey (1.52). Contacts cannot form spontaneously like shocks, but originate from the initial conditions or when shock waves interact.

1.6 Summary

This thesis consists of two topics. Firstly, the development of a multi-purpose code for the 2.5D non-linear resistive MHD equations. This code can accurately capture shocks and can also track interfaces. In chapter 2 a detailed description of the numerical scheme is presented, and in chapter 3 details of the interface tracking algorithm are given. The interface tracking capabilities of the code are tested against well known test problems in chapter 4. Secondly, some mechanisms for heating the Solar Corona are investigated. In Chapter 5 the mechanism is the phase-mixing of Alfvén waves, and in chapter 6 preliminary results from modelling nanoflares triggered by the ideal kink instability in a loop are presented.

Chapter 2

A Multi-material code for Resistive MHD

2.1 Introduction

Many problems in fluid dynamics and MHD do not readily yield an analytic solution. A number of numerical methods have been developed to solve systems of PDEs, only those which have the ability to deal with discontinuities are relevant to this thesis. The types of discontinuity under consideration have already been introduced in Section 1.5.4, namely shock fronts and contact discontinuities.

A number of problems in computational fluid dynamics involve qualitatively different regions, for example different materials in multi-phase flow or shocked/unshocked regions. There are two approaches to resolving material boundaries or contact discontinuities: interface capturing and interface tracking. Interface capturing methods use implicit indicators (eg. steep gradients in density) to locate interfaces, contact sharpening algorithms (see Colella and Woodward (1984)) can then be applied to limit the distance over which the discontinuity is smeared. Interface tracking methods require more computational effort, but resolve the discontinuity to within one computational cell. This is important when considering interface dynamics such as phase change or surface tension, or when capturing methods introduce unacceptable amounts of diffusion (eg. Rayleigh-Taylor instability).

2.1.1 Shock capturing methods

Shock capturing methods fall broadly into three categories: hybrid methods, artificial viscosity and Riemann solvers. Hybrid methods utilise sophisticated adaptive stencils to avoid calculating any gradients across a discontinuity. Normally low order schemes, which are well behaved near discontinuities, are coupled to higher order schemes for smooth regions of the solution.

Adding viscosity and heat conduction terms to the governing equations prevents any discontinuities from forming, instead smooth structures on very small scales need to be resolved. Adding artificial viscosity spreads the discontinuity over a small distance but has little effect on the rest of the flow. Sophisticated forms of artificial viscosity should only smear the shock discontinuity, the smearing of a contact discontinuity is due to the truncation error of the finite difference scheme. The amount of artificial viscosity added is that needed to control the shock, and bears no relation to the plasma's or fluid's true viscosity coefficient, hence the term artificial. The advantage of this approach is its simplicity, however since the shock is spread over a few cells, fine grids are necessary. One solution is to implement an AMR strategy.

Rather than deriving a finite difference scheme from Taylor series expansions (which assumes that the solution is smooth), Riemann solvers introduce explicit nonlinearity to the finite difference method. A solution is constructed by piecing together discontinuous solutions, these solutions closely approximate the smooth solutions in smooth regions and importantly offers a good solution where there is a discontinuity. Cell-centred variables are used to construct gradients, which may then be limited to satisfy monotonicity conditions. The characteristics are traced to determine the left and right hand states of the Riemann problem. The Riemann problem is solved between each cell to determine the fluxes to be used in the conservation laws. A schematic of this method is depicted in Figure 2.1. Riemann solvers resolve shocks very well, but are computationally expensive.

2.1.2 Contact algorithms

Interface tracking techniques fall broadly into three classes: particle methods, Volume-Of-Fluid methods and Level Set methods. Lagrangian particle methods model the material interface by particles connected by line sections, the particles are moved at the

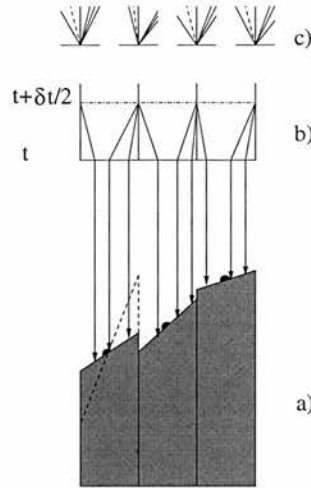


Figure 2.1: Schematic of Riemann method: a) cell centred variables (dots) are used to approximate the gradient (dashed line) which may be limited (shaded volume); b) characteristics traced to form left and right hand states of the Riemann problem; c) Riemann problem determines the fluxes used in the conservative equations.

interpolated fluid velocity. The generation of new free surfaces or the coalescence of existing interfaces, require complex and computationally expensive algorithms, as does the dynamic addition/deletion of particles to maintain resolution when the material interface expands/contracts. VOF methods use volume fraction data in each cell, and neighbouring cells, to reconstruct material interfaces. These methods are the subject of discussion in Chapter 3. The latest methods are the Level set techniques, which bear some resemblance to contouring algorithms. A function measuring the distance from the material interface to the boundary is updated in time. Currently Level Set techniques have difficulty conserving mass locally.

In the remainder of this chapter a numerical scheme for solving the non-linear resistive MHD equations (1.18)-(1.22) will be outlined. This code is based upon that presented by Arber et al. (2001). This is a Lagrangian-remap code, whereby the Lagrangian step advances the solution in time whilst the remap accounts for the transport between cells on the Eulerian grid (see Figure 2.2). The remap step is necessary since purely Lagrangian codes encounter difficulties with flows which possess strong vorticity and/or shear. This code uses artificial viscosity to resolve shock fronts, and a VOF technique to accurately track contact discontinuities.

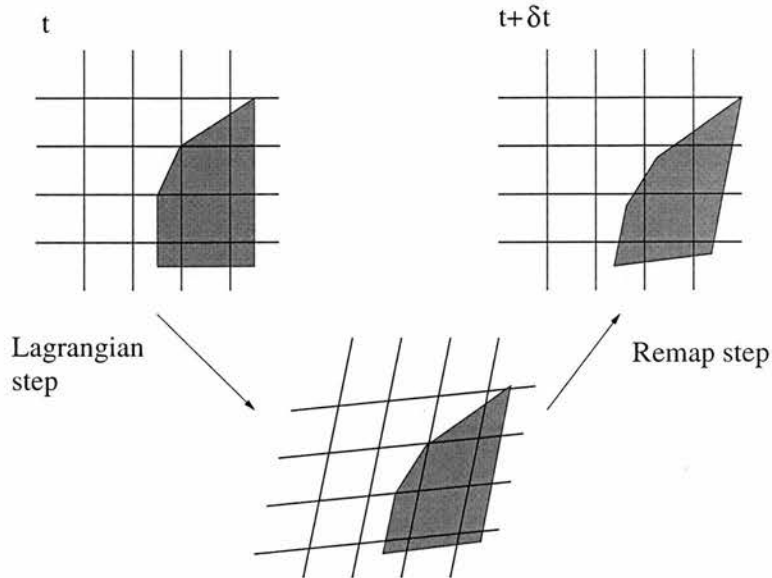


Figure 2.2: Schematic of the Lagrangian-Remap technique.

2.2 The Grid

The grid is the discrete analogue of the continuous spatial domain being modelled. The grid is defined in terms of nodes, which are labelled points where line segments meet. Both structured and unstructured grids are possible for finite difference methods. Structured grids have a repetitive pattern, whilst unstructured grids possess an arbitrary connectivity between nodes. The regions bounded by grid lines are called cells or elements. For a structured grid the cells are normally triangular or quadrilateral in two dimensions, tetrahedral or hexahedral in three dimensions.

A logical structured grid numbers its grid lines sequentially. The nodes are defined as the intersections of grid lines. Cells are labelled by the indices of their centroids, see for example Figure 2.3.

A staggered grid has the velocities positioned at the nodes, with other state variables placed at the centroids of the cells. There are other possibilities for the distribution of state variables. For example, Gudonov methods place all the state variables at the centroids of the cells, whilst some free Lagrangian methods - which use unstructured grids - place all of the state variables at the nodes.

The code presented here uses a logically structured grid, with state variables distrib-

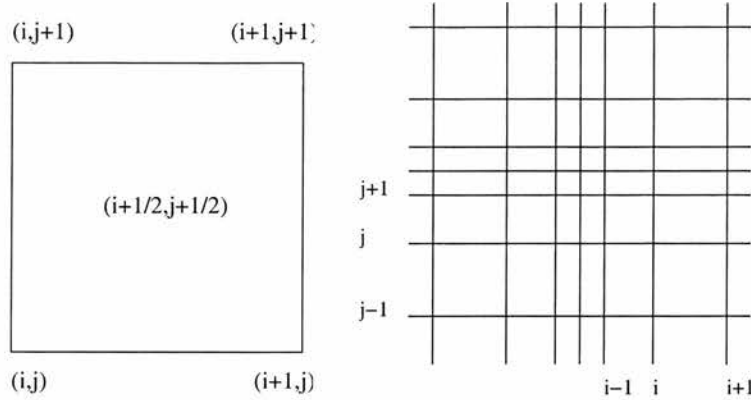


Figure 2.3: Cell labellings and a logically structured grid defined by two sets of intersecting lines.

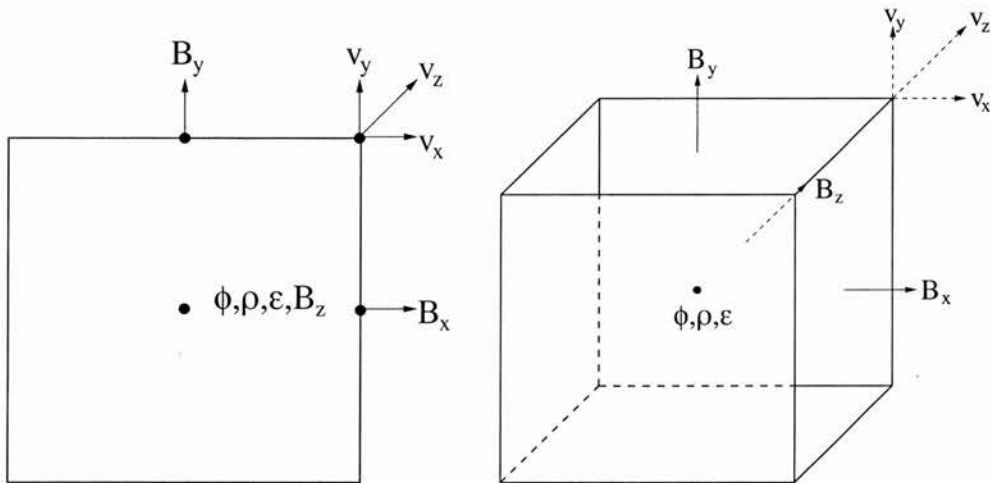


Figure 2.4: Variable placement for a staggered grid in two and three dimensions.

uted in a staggered fashion as shown in Figure 2.4 The grid is capable of being stretched to a certain extent, allowing greater resolution in areas of interest. The staggered grid prevents chequerboard instabilities (Figure 2.5), and allows the original constrained transport technique (Evans and Hawley, 1988) to be used for the solenoidal condition. This technique has been reformulated for Godunov schemes (Tóth, 2000).

2.3 Volume Of Fluid methodology

Before a more detailed exposition of the code is given, an overview of the general VOF framework is given. Initially the interface geometry is defined. From this, material

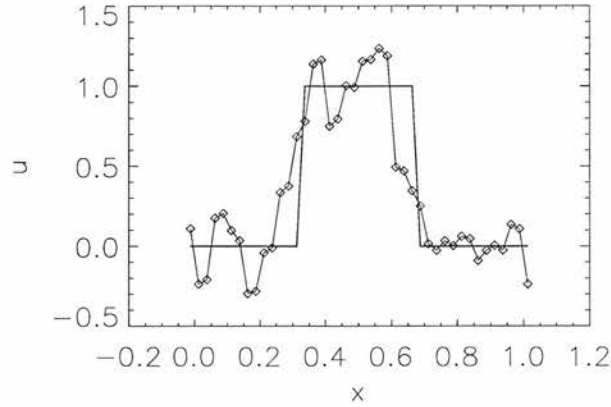


Figure 2.5: Development of the chequerboard instability from an initially square wave using the Leapfrog method.

volumes for each cell are found. An algorithm to perform this task is outlined in appendix C. Cells which contain more than one material - and hence contain an interface - are called mixed cells. In the VOF framework information pertaining to the exact interface location is discarded in favour of discrete material volume information. Associated with each cell is the volume fraction ϕ_m . If material l occupies the whole cell then $\phi_l = 1$, if material l is absent from the cell $\phi_l = 0$, and naturally if material l is not the sole occupier of the cell then ϕ_l is the fraction of the volume occupied by material l . Consequently

$$\sum_{m=1}^n \phi_m = 1,$$

for $n \in \mathbb{N}$ materials.

There are two tasks the VOF method must undertake. Firstly, an equation of motion to time advance the volume fractions must be formulated. The choice of this equation should reflect the underlying physics of the particular simulation. At any time during the simulation the exact interface locations are unknown since the volume fraction information does not guarantee a unique interface geometry. To reconstruct the interface, some algorithm is applied to the volume fraction information. The interface geometry is dependent upon the reconstruction algorithm's assumptions, which should include local volume conservation. The reconstructed interface is used to calculate the material volume fluxes required by the governing scheme.

2.4 The Equations

The equations for a single fluid description of a plasma were derived in section 1.2, they are:

$$\frac{\partial \rho}{\partial t} = -\nabla \cdot (\rho \mathbf{u}) \quad (2.1)$$

$$\rho \frac{\partial \mathbf{u}}{\partial t} + \rho (\mathbf{u} \cdot \nabla) \mathbf{u} = -\nabla P + \mathbf{g} + \mathbf{j} \wedge \mathbf{B} \quad (2.2)$$

$$\frac{\partial P}{\partial t} + (\mathbf{u} \cdot \nabla) P = -\gamma P \nabla \cdot \mathbf{u} + (\gamma - 1) \frac{1}{\sigma} j^2 \quad (2.3)$$

$$\frac{\partial \mathbf{B}}{\partial t} = \nabla \wedge (\mathbf{u} \wedge \mathbf{B}) - \nabla \wedge \left(\frac{1}{\sigma \mu_0} \nabla \wedge \mathbf{B} \right) \quad (2.4)$$

where $\mathbf{j} = \nabla \wedge \mathbf{B} / \mu_0$ is the current density, $j = |\mathbf{j}|$, μ_0 is the permeability of free space and \mathbf{g} is the effect of gravity. The solenoidal condition $\nabla \cdot \mathbf{B} = 0$ must also be satisfied. Equations (2.1)-(2.4) are formulated in Eulerian coordinates, and can be thought of as expressing a flow past a fixed point. Recasting the equations, as though moving with a fluid element, yields the Lagrangian form, which after non-dimensionalising yields:

$$\frac{D\rho}{Dt} = -\rho \nabla \cdot \mathbf{u} \quad (2.5)$$

$$\rho \frac{D\mathbf{u}}{Dt} = -\nabla P + \mathbf{g} + \mathbf{j} \wedge \mathbf{B} \quad (2.6)$$

$$\rho \frac{D\epsilon}{Dt} = -P \nabla \cdot \mathbf{u} + \eta j^2 \quad (2.7)$$

$$\frac{D\mathbf{B}}{Dt} = (\mathbf{B} \cdot \nabla) \mathbf{u} - \mathbf{B} (\nabla \cdot \mathbf{u}) - \nabla \wedge (\eta \nabla \wedge \mathbf{B}). \quad (2.8)$$

The particular normalisation used is

$$\begin{aligned} \mathbf{x} &\rightarrow x^* \mathbf{x}', & \mathbf{B} &\rightarrow B^* \mathbf{B}', & \mathbf{u} &\rightarrow u_A \mathbf{u}' \\ P &\rightarrow P^* P', & t &\rightarrow t^* t', & \rho &\rightarrow \rho^* \rho', \end{aligned}$$

where prime denotes a dimensionless variable, $u_A = B^* / \sqrt{\mu_0 \rho^*}$ is the Alfvén speed, $t^* = x^* / u_A$ is the Alfvén transit time, $P^* = B^{*2} / \mu_0$ and B^* , x^* are typical length scales. The primes have been dropped in (2.5) - (2.8). A normalisation often used takes $\eta^* = \mu_0 x^* u_A / S$, so that for uniform resistivity

$$\frac{\partial \mathbf{B}}{\partial t} = \nabla \wedge (\mathbf{u} \wedge \mathbf{B}) + \frac{1}{S} \nabla^2 \mathbf{B}$$

and the Lundquist number $S = \tau_d/\tau_A$ can be specified. This code permits the use of a non-uniform resistivity, and so keeps a normalised η in the equations by setting $\eta = \mu_0 x^* u_A$.

For certain simulations it is desirable to have non-uniform resistivity, for example three dimensional kink instabilities where reconnection occurs only within the current sheet. Some evidence suggests that once the electron fluid flow speed, u_e exceeds the phase speed of the ion-acoustic mode, u_{ia} , that ion-acoustic turbulence will strongly influence current sheet formation. Bychenkov et al. (1988) have shown that, under certain conditions, the effective anomalous resistivity is a function of j and adjusts to keep $u_e \leq \alpha u_{ia}$ where α is prescribed by the initial conditions. An effective formulation of anomalous resistivity is

$$\eta = \eta_0 \max\left(0, \frac{|u_e|}{\alpha u_{ia}} - 1\right).$$

The form of non-uniform resistivity as a function of current used in the code follows Arber and Van der Linden (1999)

$$\eta = \eta_0 \max\left(0, \frac{|j|}{j_{crit}} - 1\right), \quad (2.9)$$

where $j_{crit} = \alpha n e u_{ia}$ and it is assumed $|u_e| \approx |j|/ne$. The user prescribed constant j_{crit} is normally much smaller than theoretical values. This can be shown by again considering an unstable coronal loop, with a maximum current density $j_{max} = \alpha n e u_{ia}$. Taking

$$j \approx \frac{B_0}{\mu_0 L},$$

then to reach j_{max} would require a length scale collapse to

$$L_{min} = \frac{B_0}{\mu_0 \alpha n e u_{ia}}.$$

For $B_0 = 100G$, $n = 5 \times 10^{14} m^{-3}$, $\alpha = 10$, $u_{ia} = 1.35 \times 10^5 ms^{-1}$, $e =$ and $\mu_0 =$ gives $L_{min} = 76.5$. With a loop of radius $r \approx 1Mm$ the difference in length scale is approximately 13000. To resolve current sheets with current densities up to j_{max} requires a uniform grid of about 50000^3 grid points. A stretched grid improves this slightly, but it is still beyond the realms of current technology. An AMR technique would be ideally suited to this type of problem.

Notice that equation (2.7) is given in terms of the internal energy density ϵ , and has

replaced the total energy equation (2.3). A code which uses the conservative form of the energy equation incurs large errors in thermal pressure (and hence temperature for an ideal gas equation of state) for a low beta plasma. This stems from the thermal pressure being calculated as the difference of two large numbers in such a code. Despite using a non-conservative form for the energy equation, in the absence of a magnetic field total energy is still conserved to machine precision during the Lagrangian step. Details of how this is achieved will be described at a later point. When a magnetic field is present, errors in total energy are due to the magnetic tension force.

2.4.1 The Equation Of State

To complete (2.5) - (2.8) a relationship between ϵ and P must be defined. This is the equation of state and a few options exist within the code. For a Lagrangian scheme it is a trivial matter to utilise more complicated equations of state.

Firstly a void equation of state is implemented.

$$P = \text{constant} \quad (2.10)$$

$$c_s^2 = 0. \quad (2.11)$$

This allows pure advection, and is particularly useful in testing interface tracking algorithms.

Second is the commonly used ideal gas equation of state.

$$P = \epsilon \rho (\gamma - 1) \quad (2.12)$$

$$c_s^2 = \frac{\gamma P}{\rho}. \quad (2.13)$$

Here γ is the ratio of specific heats at constant pressure and constant volume. Typical values for γ are 5/3 for a fully ionised plasma, 1.4 for air at STP.

Also included is the Tait equation of state:

$$P_1 = a \left(\left(\frac{\rho}{\rho_0} \right)^b - 1 \right), \quad P = \max(P_1, P_0) \quad (2.14)$$

$$c_s^2 = \frac{ab}{\rho_0} \left(\frac{\rho}{\rho_0} \right)^{b-1}, \quad (2.15)$$

where P_0 is the minimum pressure, and a , b and ρ are constants defining the materials properties.

The last equation of state included is JWL.

$$P = \omega\rho\epsilon + ae^{-r_1v}\left(1 - \frac{\omega}{r_1v}\right) + be^{-r_2v}\left(1 - \frac{\omega}{r_2v}\right) \quad (2.16)$$

$$c_s^2 = \omega\frac{P}{\rho} + \omega\epsilon - ae^{-r_1v}\left(\frac{\omega}{r_1} + \omega v - r_1v^2\right) - be^{-r_2v}\left(\frac{\omega}{r_2} + \omega v - r_2v^2\right), \quad (2.17)$$

where $v = \rho/\rho_0$ and a , b , ω , r_1 , r_2 and ρ_0 are constants defining the materials properties.

2.4.2 The multi-material equations

For a multi-material code, each material possesses values of ϕ , P , ρ and ϵ . A simplification that is made is to ignore the possibility of material penetration and voids. This is achieved by having one velocity field to evolve the grid during the Lagrangian step, rather than each individual material possessing its own velocity. Materials also do not possess individual values of \mathbf{B} . Although $\nabla \cdot \mathbf{B} = 0$ is an initial constraint, it must be explicitly enforced in any numerical scheme. Methods for achieving this will be discussed later. Enforcing the solenoidal condition on a multi-material cell with each material possessing a value for \mathbf{B}_m is complicated. This problem is further aggravated by the interface being irregular and discontinuous across cell edges. This problem has been left to the future, and a single magnetic field permeates the numerical domain. The multi-material equations for up to n materials with $1 \leq m \leq n$ are

$$\frac{D}{Dt}(\phi_m\rho_m) = -\phi_m\rho_m\nabla \cdot \mathbf{u} \quad (2.18)$$

$$\sum_{m=1}^n (\phi_m\rho_m) \frac{D\mathbf{u}}{Dt} = -\nabla \left(\sum_{m=1}^n (\phi_m P_m) \right) + \mathbf{g} + \mathbf{j} \wedge \mathbf{B} \quad (2.19)$$

$$\phi_m\rho_m \frac{D\epsilon_m}{Dt} = -\phi_m P_m \nabla \cdot \mathbf{u} + \eta_m j^2 \quad (2.20)$$

$$\frac{D\mathbf{B}}{Dt} = (\mathbf{B} \cdot \nabla) \mathbf{u} - \mathbf{B}(\nabla \cdot \mathbf{u}) - \nabla \wedge (\eta \nabla \wedge \mathbf{B}) \quad (2.21)$$

$$P_m = P_m(\rho_m, \epsilon_m). \quad (2.22)$$

The single material equations are regained by realising that

$$P = \sum_{m=1}^n (\phi_m P_m), \quad \rho = \sum_{m=1}^n (\phi_m \rho_m), \quad \text{and} \quad \epsilon = \frac{\sum_{m=1}^n (\phi_m \rho_m \epsilon_m)}{\sum_{m=1}^n (\phi_m \rho_m)}.$$

It should be noted that a particular partitioning of energy is used in deriving (2.20):

$$\begin{aligned} \frac{D}{Dt} \left(\phi_m \rho_m \left(\epsilon_m + \frac{u^2}{2} \right) \right) &= \mathbf{u} \cdot \nabla \phi_m \rho_m \frac{D\mathbf{u}}{Dt} + \dots \\ &= -\mathbf{u} \cdot \nabla (\phi_m P_m) + \dots, \end{aligned}$$

which follows from the momentum equation, but this is only strictly true when summed over all m . Also, the partitioning of ohmic heating is in a simple area weighted manner. It would be possible to assign individual values of η_m to each material, but this has yet to be implemented. The equation of state, and the parameters for the equations of state, can be set for each material independently.

2.4.3 Mixing theory

To close the system of equations (2.18)-(2.22) the variation of ϕ_m with time is needed. Such an equation controls the mixing of materials within a cell.

The simplest choice is known as Equal expansion

$$\frac{D\phi_m}{Dt} = 0. \tag{2.23}$$

This condition assumes equal strain rates which can be incorrect. In a mixed cell containing, for example, steel and air, the air is highly compressible and should absorb most of the volumetric strain. Instead, the steel is forced to accept an equal amount of the strain as air. Despite this error, Equal expansion gives good results, is the simplest to implement, and is the condition used in this code.

At low pressures solids are essentially incompressible. An incompressible material is described by

$$\frac{D\phi_m}{Dt} = -\phi_m \nabla \cdot \mathbf{u},$$

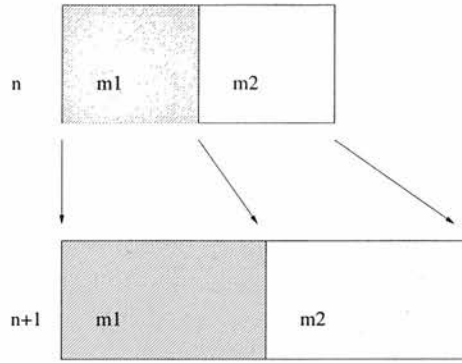


Figure 2.6: An initial mixed Eulerian cell and the developed Lagrangian cell according to “Equal expansion”.

the other material fills the remaining space (Bdzil et al., 1999).

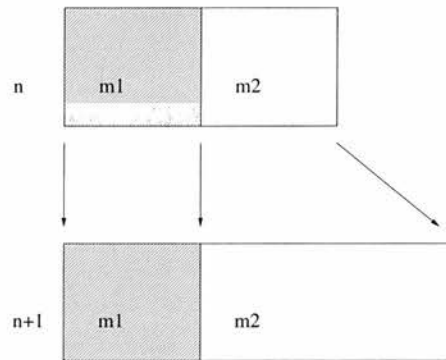


Figure 2.7: An initial mixed Eulerian cell and the developed mixed Lagrangian cell with one material incompressible.

Another possibility is for all the materials to have the same pressure, ie. the material interfaces are positioned to enclose the correct volume. This is also a physically unrealistic assumption, a wave is capable of crossing a cell several times before materials equilibrate. However the CFL condition (discussed in Section 2.5.3) restricts a wave from crossing a cell in a single timestep. Pressure equilibrium defines the volume fractions to achieve

$$P_m(\rho_m, \epsilon_m) - P_{m+1}(\rho_{m+1}, \epsilon_{m+1}) = 0 \quad \forall m.$$

Artificial viscosity, see Section 2.5.2, may or may not be included in the above expression for P . Further details of this condition can be found in Benson (1992) and Bruce Stewart and Wendroff (1984). It should be noted that using pressure equilibrium often results in a mixed hyperbolic-elliptic set of governing equations.

Possibly the most realistic choice for updating ϕ_m is time dependent compaction (Bdzil et al., 1999), (Baer and Nunziato, 1986).

$$\frac{D\phi_m}{Dt} = f(\phi_m, P_m, \rho_m, v_m).$$

This drives the phases toward equilibrium on some equilibration time scale. The resulting system of equations is hyperbolic, and it is possible to accommodate physical processes such as evaporation, burning etc. in the compaction equation.

2.5 The Lagrangian step

The equations (2.18) - (2.21) are multi-dimensional, and no directional splitting is required during the Lagrangian step. This step uses a simple predictor-corrector scheme. Predicted values of \mathbf{B} , ρ_m , ϵ_m and \mathbf{u} are found at the half timestep. These are used to update \mathbf{B} , ρ_m , ϵ_m and \mathbf{u} to the full timestep. When the ideal set of equations are being used (ie. $\eta = 0$), \mathbf{B} is not corrected as it is magnetic flux which will be remapped, and this is conserved during the Lagrangian step. A predicted value of \mathbf{B} is required for the correction of the momentum equation (2.19). Since the Equal expansion condition (2.23) is used, nothing need be done to ϕ_m during the Lagrangian step.

Mass conservation is used wherever possible in the corrector step. In one dimension this reduces to using mass coordinates, in multi-dimensions a control volume approach is used which conserves mass and energy over the full timestep to machine precision. Rather than using equation (2.18) to update ρ , the change in density is directly related to the change in volume via mass conservation. If a material element is initially at a point $\mathbf{x}^E = (x_1^E, x_2^E, x_3^E)$ and moves to a new point $\mathbf{x}^L = (x_1^L, x_2^L, x_3^L)$, then \mathbf{x}^L is a function of \mathbf{x}^E and time. The change in element length (Craig and Sneyd, 1986) is given by

$$dx_i = \frac{\partial x_i^L}{\partial x_\alpha^E} dx_\alpha^E \quad \text{with summation convention over } \alpha.$$

Now $\rho = \rho_0/\Delta$ where ρ_0 is the initial density and Δ is the determinant of the Jacobian

transformation matrix which in three dimensions is

$$\Delta = \left| \frac{\partial \mathbf{x}^L}{\partial \mathbf{x}^E} \right| = \begin{vmatrix} \frac{\partial x_1^L}{\partial x_1^E} & \frac{\partial x_2^L}{\partial x_1^E} & \frac{\partial x_3^L}{\partial x_1^E} \\ \frac{\partial x_1^L}{\partial x_2^E} & \frac{\partial x_2^L}{\partial x_2^E} & \frac{\partial x_3^L}{\partial x_2^E} \\ \frac{\partial x_1^L}{\partial x_3^E} & \frac{\partial x_2^L}{\partial x_3^E} & \frac{\partial x_3^L}{\partial x_3^E} \end{vmatrix}.$$

In this code the approximation

$$\Delta = 1 + (\nabla \cdot \mathbf{u})dt$$

is used, with $\nabla \cdot \mathbf{u}$ evaluated on the Eulerian grid. This is illustrated graphically for the two dimensional case starting with a rectangular cell evolved in time as shown in Figure 2.8. For this example of an expanding cell, the approximate volume is smaller than the true volume. Figure 2.8(a) shows the original cell, the Lagrangian cell (bold lines) and the $1 + (\nabla \cdot \mathbf{u})dt$ approximation to the Lagrangian volume (shaded). The error between the approximation and the true volume is the difference between the hatched rectangle and the black rectangle in Figure 2.8(b). If the volume was approximated by

$$\left(1 + \frac{\partial u_x}{\partial x_1^E} dt\right) \left(1 + \frac{\partial u_y}{\partial x_2^E} dt\right) = 1 + (\nabla \cdot \mathbf{u})dt + \frac{\partial u_x}{\partial x_1^E} \frac{\partial u_y}{\partial x_2^E} dt^2,$$

this approximation is larger than the true volume by

$$\frac{\partial u_x}{\partial x_2^E} \frac{\partial u_y}{\partial x_1^E} dt^2,$$

the black rectangle in Figure 2.8(b). Mass is conserved during the Lagrangian step, the error is proportional to the volume error (apart from in one dimension, where $1 + (\nabla \cdot \mathbf{u})dt$ is exact).

This approximation is shown to be accurate to second order by considering the change in position (for the x-coordinate, y and z coordinates are similarly defined)

$$x_1(\mathbf{x}^E, t) = x_1^E + \int_0^{dt} u_x(\mathbf{x}^E, t) dt.$$

Using a Taylor series expansion for u_x about the original position \mathbf{x}^E yields

$$x_1^L = x_1^E + u_x dt + \left(\frac{\partial u_x}{\partial x_1^E} u_x + \frac{\partial u_x}{\partial x_2^E} u_y + \frac{\partial u_x}{\partial x_3^E} u_z \right) \frac{dt^2}{2} + O(dt^3),$$

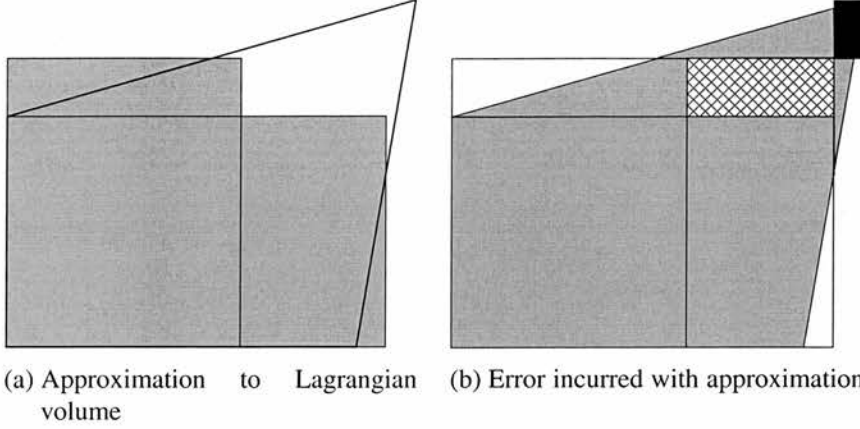


Figure 2.8: Eulerian and Lagrangian cells at the end of the Lagrangian step.

with similar relations for x_2^L , x_3^L . The determinant of the Jacobian matrix becomes

$$\Delta = \frac{\partial \mathbf{x}^L}{\partial \mathbf{x}^E} = \begin{vmatrix} 1 + \frac{\partial u_x}{\partial x_1^E} dt & \frac{\partial u_y}{\partial x_1^E} dt & \frac{\partial u_z}{\partial x_1^E} dt \\ \frac{\partial u_x}{\partial x_2^E} dt & 1 + \frac{\partial u_y}{\partial x_2^E} dt & \frac{\partial u_z}{\partial x_2^E} dt \\ \frac{\partial u_x}{\partial x_3^E} dt & \frac{\partial u_y}{\partial x_3^E} dt & 1 + \frac{\partial u_z}{\partial x_3^E} dt \end{vmatrix} + O(dt^2).$$

This gives

$$\Delta = 1 + \left(\frac{\partial u_x}{\partial x_1^E} + \frac{\partial u_y}{\partial x_2^E} + \frac{\partial u_z}{\partial x_3^E} \right) dt + O(dt^2) = 1 + (\nabla \cdot \mathbf{u}) dt + O(dt^2).$$

Relating changes in density to changes in volume and applying these relationships consistently ensures conservation of mass to machine precision.

There are two complications in the Lagrangian step, the update of the magnetic field and artificial viscosity.

2.5.1 The magnetic field

When resistivity is included, magnetic field components and ohmic heating terms need to be calculated at both the predictor and corrector steps. Integrating the induction equation (2.21) over a cell volume gives

$$\int \frac{D\mathbf{B}}{Dt} dV = \int ((\mathbf{B} \cdot \nabla) \mathbf{u} - \mathbf{B}(\nabla \cdot \mathbf{u})) dV - \int \nabla \wedge (\eta \mathbf{j}) dV \quad (2.24)$$

$$\frac{D}{Dt} \int B_i dV = \int u_i B_j \hat{n}_j dS - \int \epsilon_{ijk} \frac{\partial}{\partial x_j} (\eta j_k) dV. \quad (2.25)$$

Here \hat{n} is the outward pointing normal, and ϵ_{ijk} is the Levi-Civita tensor. For ideal MHD only predicted values of \mathbf{B} are needed, and only the first term on the RHS of (2.25) is calculated. Ohmic heating is calculated with \mathbf{j} evaluated at the beginning of the timestep, and is used to predict energy.

Integrating (2.21) over the Lagrangian cell surface gives

$$\frac{D}{Dt} \int (\mathbf{B} \cdot d\mathbf{S}) = \int \eta \mathbf{j} \cdot d\mathbf{l},$$

where $d\mathbf{l}$ is the line integral around the surface S (see appendix B for details). In this way the magnetic fluxes are updated during the corrector step. Ohmic heating is again calculated using a predicted value of \mathbf{j} and is used to correct energy.

2.5.2 Artificial viscosity

An artificial viscosity (q) is added to the governing MHD equations to enable the code to capture shocks. In particular, q is added to the equations of motion and energy as follows,

$$\begin{aligned} \rho \frac{D\mathbf{u}}{Dt} &= -\nabla(P + q) + \mathbf{j} \wedge \mathbf{B}, \\ \rho \frac{D\epsilon}{Dt} &= -(P + q)\nabla \cdot \mathbf{u} + \eta j^2. \end{aligned}$$

The variable q should only be non-zero in the environs of a shock wave, no artificial viscosity should be present elsewhere in the flow. A useful criteria presented by Caramana et al. (1990), is that artificial viscosity should:

1. always act to decrease kinetic energy (be dissipative),
2. vary continuously, tending to zero as compression tends to zero, and remain zero for expansion,
3. be zero for uniform contraction and/or rigid rotation,
4. have no effect along a wave front of constant phase,
5. vanish uniformly as the velocity field becomes constant.

The original formulation of artificial viscosity was introduced by von Neumann and Richtmyer (1950), and was used for calculating one dimensional shock problems in an inviscid fluid,

$$q = c_0^2 \rho (\delta x)^2 \left(\frac{\partial u}{\partial x} \right)^2, \quad q = 0 \text{ for } \frac{\partial u}{\partial x} \geq 0, \quad (2.26)$$

where c_0 is a constant which determines the number of cells across which the shock front will be spread. This can be recast as a diffusion equation with diffusion coefficient α ,

$$\alpha = c_0^2 \rho (\delta x) \left| \frac{\partial u}{\partial x} \right|.$$

Real viscosity is independent of the cell width, here α is grid dependent. However, the purpose of q is to connect - over as few cells as possible - the state ahead of the shock with that behind the shock, rather than to represent a real viscosity. Landshoff (1955) proposed the following form for artificial viscosity, which is more capable of dealing with weak shocks,

$$q = c_1 \rho (\delta x) c_s \left| \frac{\partial u}{\partial x} \right|, \quad q = 0 \text{ for } \frac{\partial u}{\partial x} \geq 0, \quad (2.27)$$

where c_1 is a constant. Although (2.26) copes well with strong shocks, it can produce unphysical oscillations. The initial overshoot of (2.27) is larger than that of (2.26), but (2.27) provides faster damping. Dissipation occurs over a larger distance using (2.27) rather than (2.26). The combination of both linear and quadratic terms gives an artificial viscosity which takes advantage of each term. A balance must be found between dissipating the shock enough (ie. to avoid numerical oscillation) without causing too much dissipation in the smooth regions of the solution. This can be achieved by altering the constants c_0 and c_2 in equation (2.28).

This code uses the artificial viscosity suggested by Wilkins (1980), which in one dimension is

$$q = c_1 \rho c_f |\Delta u| + c_2 \rho (\Delta u)^2, \quad (2.28)$$

where Δu is the change in velocity across the shock front. A derivation of this form from the Rankine-Hugoniot jump conditions following Kuropatenko (1967) is given in appendix A. It should be noted that $\sqrt{P/\rho}$ replaces c_s in the calculation of c_f . This is because the coefficient derived from appendix A assumes ideal gas as the equation of

state, this does not supply enough damping of numerical oscillations behind the shock front for certain other equations of state. The use of $\sqrt{P/\rho}$ can be used for all materials, solid or fluid.

Extending (2.28) to multi-dimensions requires replacing Δu by the rate of strain in the direction of acceleration ds/dt . Consider a two dimensional cell with a large aspect ratio giving a large area which leads to a large effective q , even though the shock may be traversing the shortest width of the cell. To solve this, a characteristic grid length L in the direction of acceleration is used.

$$q = c_1 \rho L^2 \left(\frac{ds}{dt} \right)^2 + c_2 \rho L c_f \left| \frac{ds}{dt} \right|. \quad (2.29)$$

The constants c_1 and c_2 are user defined and problem specific, but normally range between 0 and 1. Low resolution simulations can be used to estimate the required values of c_1 and c_2 for full scale simulations.

The choice of how to partition the artificial viscosity's contribution to the specific internal energy between materials is to a certain extent arbitrary. The choice made is to mass-weight the artificial viscosity, the other obvious choice is to volume-weight q . The latter option, however, can preferentially heat the lower density gas in a mixed cell. To illustrate why mass-weighting is preferred, consider the case of two materials, one a factor of a hundred more dense than the other, occupying a cell. So $\rho_1 = 100\rho_2$, and the equation representing the update of the specific internal energy using volume-weighting (see appendix D for the mass-weighted update equation), is

$$\phi_m \rho_m \epsilon_m^{n+1} = \phi_m \rho_m \epsilon_m^n - dt \nabla \cdot \mathbf{u} (\phi_m P_m + \phi_m q),$$

yielding

$$\begin{aligned} \epsilon_1^{n+1} &= \epsilon_1^n - \frac{dt}{\rho_1} \nabla \cdot \mathbf{u} (P_1 + q) \\ \epsilon_2^{n+1} &= \epsilon_2^n - 100 \frac{dt}{\rho_1} \nabla \cdot \mathbf{u} (P_2 + q). \end{aligned}$$

The increase in ϵ_2 (where $\nabla \cdot \mathbf{u} < 0$) is far greater than the increase in ϵ_1 . Since temperature is proportional to specific internal energy for an ideal gas equation of state, the lower density gas will be preferentially heated by any shock in the mixed cell. This is incorrect for an ideal gas, and why mass-weighting is favoured. Care must be taken to neglect the

effects of artificial viscosity when a material is under tension.

Recently, tensor formulations of artificial viscosity have been reported (Schulz, 1964), (Caramana et al., 1990), which either follow real compressible viscosity more closely, or use limited edge centred viscosity. Improvements over (2.29) can be observed in multi-dimensional problems.

Artificial viscosity can exacerbate some problems. Take, for example, the well known wall heating test problem (Noh, 1978). This configuration is a one dimensional ideal gas, with $u_x = 1$ for $x < 0.5$ and $u_x = -1$ for $x \geq 0.5$, $\rho = 1$, $P = 10^{-6}$ with inflow boundary conditions. The analytic solution has a constant state behind the shock fronts. For an analysis of this problem explaining the different errors which occur depending on the coordinate system and form of energy equation used, see Rider (2000). Figure 2.9 shows that increasing the artificial viscosity to control the shock front increases the error at the origin. Tensor artificial viscosities fair a little better than their scalar counterparts, but it is the inclusion of artificial heat conduction which provides results comparable to an Eulerian PPM code solving for total energy.

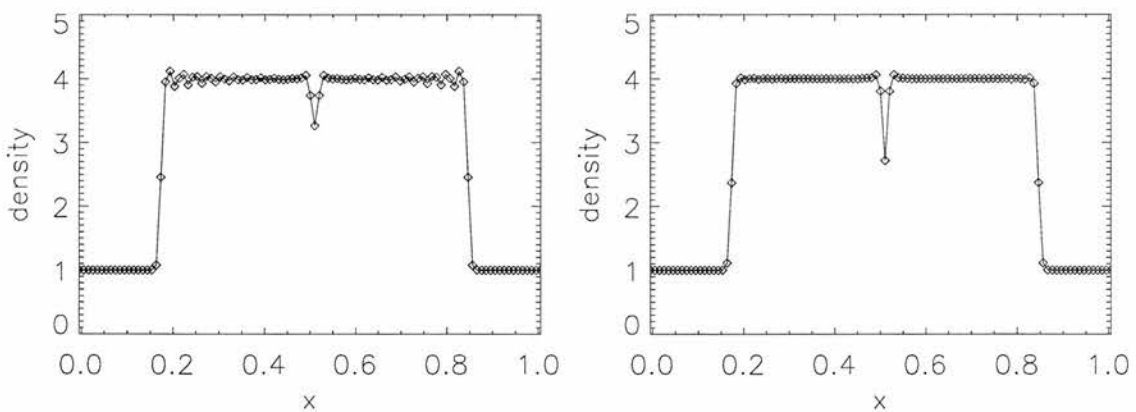


Figure 2.9: Noh’s wall heating problem, increasing the artificial viscosity to control the shocks at $x = 0.16$ and $x = 0.84$ increases the error at the “wall”, $x = 0.5$.

2.5.3 The CFL condition

The CFL condition is a necessary but insufficient condition for the stability of explicit time-marching schemes. To satisfy this condition the timestep is limited to ensure that in-

formation cannot traverse an entire cell during that timestep. For this propagation speeds are required. Firstly, the maximum fast magnetoacoustic speed is $c_f = \sqrt{c_s^2 + v_A^2}$, where v_A is the maximum Alfvén speed and c_s is the maximum sound speed from all of the present material sound speeds c_{sm} . c_{sm} is calculated from the equations of state stated in Section 2.4.1.

$$dt < \min\left(\frac{\delta x}{c_f + |u_x|}, \frac{\delta y}{c_f + |u_y|}, \frac{\delta z}{c_f + |u_z|}\right). \quad (2.30)$$

The effect of artificial viscosity, if present, need also be included. This has a characteristic speed $\sqrt{q/\rho}$. The resistivity has a characteristic speed of $\eta/\delta s$ where δs is the minimum cell width. So

$$dt < \frac{\delta s^2}{2\eta}. \quad (2.31)$$

The Lagrangian cells are prevented from overlapping by enforcing

$$dt < \frac{1}{\nabla \cdot |\mathbf{u}|}. \quad (2.32)$$

The most prohibitive of these is the resistivity condition (2.31). Although values of η in the Corona are thought to be small, η is large enough that the global timestep is limited using (2.31). To enable a larger global timestep it would be possible to subcycle the resistivity calculation. That is, (2.30) or (2.32) is used to limit dt , the resistivity calculation is repeatedly performed with a fraction of this dt that satisfies (2.31). This produces faster but less accurate simulations compared with limiting the entire calculation by (2.31). If larger than coronal values of η are necessary, the best strategy is to employ an implicit scheme for solving the resistivity calculation.

2.6 The Remap step

At the end of the Lagrangian step all state variables have been updated on a grid which has developed with the flow. To avoid difficulties associated with large grid deformation (eq. flows containing strong vorticity or strong shearing motions) inherent in structured purely Lagrangian schemes, these variables are remapped back onto the original Eulerian grid. In this code the remap is performed every timestep, but this need not necessarily be so. The remap of the state variables is performed in one dimensional sweeps along the coordinate

axes. The order in which the sweeps are performed is permuted to avoid any directional bias (Strang, 1968). One would prefer a multi-dimensional remap, then the code would be fully multi-dimensional. However, the Lagrangian step is multi-dimensional and this is the step which advances the state variables in time, the remap is purely geometrical. Nonetheless some physics may be lost by the use of Strang splitting the remap (refer to test problem 4.4.2). Two dimensional remaps incorporating corner-coupling have been reported by Rider and Kothe (1998). Such remaps are as accurate as their one dimensional counterparts and maintain any symmetry of the system. Since the remap step is far more computationally expensive than the Lagrangian step, two dimensional remaps produce more efficient code. This is even more marked with an interface tracking code as the interface need only be calculated once. First consider the case of a one dimensional single material remap of the fluid variables, these remaps follow similarly from Youngs (1982) and Arber et al. (2001).

2.6.1 Single material remap of Fluid variables

For the single material case the volume fraction is redundant - $\phi = 1$ - and nothing need be done for this variable.

Mass

Mass conservation is used throughout the code to calculate density. The mass on the evolved Lagrangian grid is known, what is required is the mass left on the original Eulerian grid to which we are remapping. This is calculated by discovering the amount of mass which has entered and left each Eulerian cell. Since the mass which moves into an Eulerian cell is naturally the mass that has left adjacent Eulerian cells, it is sufficient to calculate the mass flux on one edge of the cell. For example the shaded region (dM_i) in Figure 2.10, which has left the Eulerian cell as the bulk Lagrangian motion is to the right.

$$\text{mass left in Eulerian cell } i = \text{original mass in Eulerian cell } i - dM_i + dM_{i-1}.$$

For a general coordinate s , the total mass in the original Eulerian cell i is $\rho_i dsb_i$, the total mass in the Lagrangian cell i after dt is $\rho_i^L dsb_i^L$. Conservation of mass implies

$$\rho_i dsb_i = \rho_i^L dsb_i^L.$$

The first step in calculating dM_i is to calculate the density at the centre of dM_i . For the

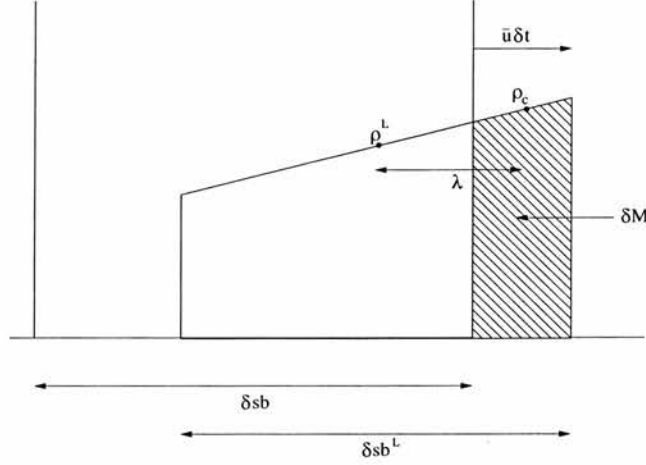


Figure 2.10: Single material density remap: showing a Lagrangian cell whose bulk motion is to the right of the Eulerian cell. The shaded region depicts dM_i .

case where $\bar{u}_i > 0$, as shown in Figure 2.10, this is

$$\rho_c = \rho_i^L + \lambda \frac{\partial \rho_i^L}{\partial s^L}.$$

By simple geometry

$$\lambda = \frac{1}{2} (dsb_i^L - |\bar{u}_i| \delta t),$$

where \bar{u}_i is the s component of the time averaged velocity. Let $D_i = \partial \rho_i^L / \partial s$, $\kappa_i = |\bar{u}_i| \delta t / dsb_i^L$,

$$\rho_c = \rho_i^L + \frac{dsb_i^L}{2} D_i (1 - \kappa_i).$$

So,

$$dM_i = \left(\rho_i^L + \frac{dsb_i^L}{2} D_i (1 - \kappa_i) \right) \bar{u}_i \delta t, \quad (2.33)$$

$$\rho_i^{n+1} dsb_i = \rho_i^L dsb_i^L - dM_i + dM_{i-1}. \quad (2.34)$$

Briefly, when $\bar{u}_i \leq 0$ κ_i and (2.34) become

$$\kappa_i = |\bar{u}_i| \delta t / dsb_{i+1}^L, \quad dM_i = \left(\rho_{i+1}^L + \frac{dsb_{i+1}^L}{2} D_i (1 - \kappa_i) \right) \bar{u}_i \delta t. \quad (2.35)$$

The calculation of D_i is discussed in Section 2.6.2.

Specific energy

This variable's remap differs from the previous case since mass coordinates are preferred to Lagrangian coordinates. Again taking the case of $\bar{u}_i > 0$ as depicted in Figure 2.11, the specific energy that has left the Eulerian cell i during the timestep $d\zeta_i$ can be calculated.

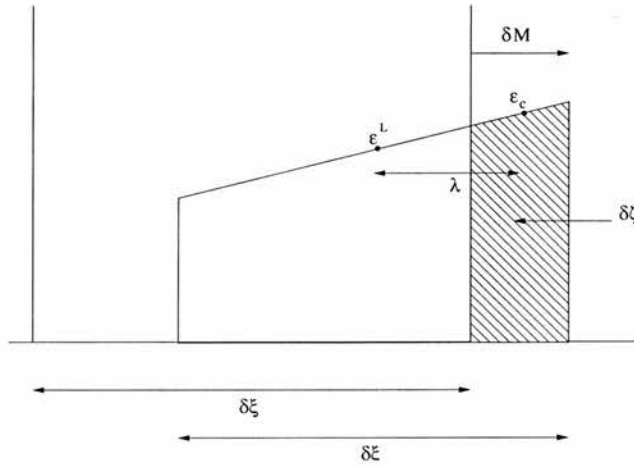


Figure 2.11: Single material specific energy remap: showing a Lagrangian cell whose bulk motion is to the right of the Eulerian cell. The shaded region depicts $d\zeta_i$.

$$d\xi_i = \rho_i dsb_i = \rho_i^L dsb_i^L, \quad (2.36)$$

$$\epsilon_c = \epsilon_i^L + \lambda \frac{\partial \epsilon_i^L}{\partial \xi}, \quad (2.37)$$

where ξ is the mass coordinate and

$$\lambda = \frac{1}{2}(d\xi_i - dM_i).$$

Since

$$d\xi \frac{\partial \epsilon^L}{\partial \xi} = dsb_i \frac{\partial \epsilon^L}{\partial s},$$

then

$$d\zeta_i = \left(\epsilon_i^L + \frac{dsb_i}{2} D_i (1 - \kappa_i) \right) dM_i, \quad (2.38)$$

where $D_i = \partial \epsilon^L / \partial s$ and $\kappa = dM_i / d\xi$. The specific energy remap is

$$\epsilon_i^{n+1} \rho_i^{n+1} dsb_i = \epsilon_i \rho_i dsb_i + d\zeta_{i-1} - d\zeta_i. \quad (2.39)$$

Similar results hold for the case $\bar{u}_i \leq 0$.

Momentum

The momentum remap is essentially the same as that for specific energy. However, since velocity is defined at the cell vertex rather than the cell centroid, a control volume centred on the vertex is used. Kinetic energy is also remapped to enforce energy conservation.

2.6.2 Gradient Limiters

All that remains is to explain the calculation of D_i . These gradients are calculated using a third order upwind method suggested by Youngs (1982). For an arbitrary variable ψ and arbitrary coordinate s ,

$$\left| \frac{\partial \psi_i}{\partial s^L} \right| = \frac{(2 - \kappa_i) |\psi_{i+1} - \psi_i|}{3 ds_{i+1}^L} + \frac{(1 + \kappa_i) |\psi_i - \psi_{i-1}|}{3 ds_i^L}, \quad \bar{u}_i > 0, \quad (2.40a)$$

$$= \frac{(2 - \kappa_i) |\psi_{i+1} - \psi_i|}{3 ds_{i+1}^L} + \frac{(1 + \kappa_i) |\psi_{i+2} - \psi_{i+1}|}{3 ds_{i+2}^L}, \quad \bar{u}_i \leq 0. \quad (2.40b)$$

This third order method offers slight improvements over a second order method, with little extra computational effort.

A gradient limiter is used to largely suppress any spurious numerical oscillations. Gradient limiters are closely related to flux limiters, indeed the terms are interchangeable in some contexts. Gradient limiters satisfy geometrically derived monotonicity conditions similar to the algebraically derived TVD condition satisfied by flux limited methods ($\text{TVD} \equiv \text{TV}(\psi^{n+1}) \leq \text{TV}(\psi^n)$ where $\text{TV}(\psi^n) = \sum_i |\psi_{i+1}^n - \psi_i^n|$). Gradient limiters are discussed in more detail by LeVeque (1992), a comparison of several flux limiters is made by Sweby (1984). This code uses the gradient limiters proposed by van Leer (1997). Van Leer's flux limiter exhibits results nearly as good as Roe's superbee method (Roe, 1985), whilst being symmetric, more robust and smoothly varying.

For the case $\bar{u}_i > 0$, the gradient D_i is limited by forcing the value of ψ_i extrapolated

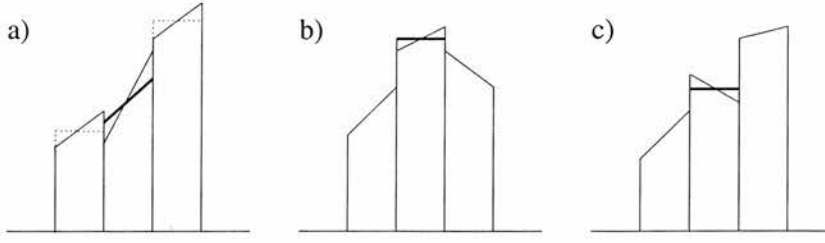


Figure 2.12: The monotonicity condition: a) The gradient (solid line) of the central cell is reduced (bold line) so that values in this cell do not go beyond the average levels (dotted line) in the adjacent cells; b) If the grid average reaches an extremum, the gradient is set to zero; c) If the gradient does not agree with the trend in the grid averages, then it is set to zero.

to the boundaries of cell i to be less than ψ_{i+1} and greater than ψ_{i-1} . So

$$\psi_i + \frac{ds_i^L}{2} \frac{\partial \psi_i}{\partial s^L} < \psi_{i+1} \Rightarrow ds_i^L \frac{\partial \psi_i}{\partial s^L} < 2(\psi_{i+1} - \psi_i)$$

and

$$\psi_i + \frac{ds_i^L}{2} \frac{\partial \psi_i}{\partial s^L} > \psi_{i-1} \Rightarrow ds_i^L \frac{\partial \psi_i}{\partial s^L} < 2(\psi_i - \psi_{i-1}).$$

These conditions are met by choosing

$$|D_i| = \min \left(\left| \frac{\partial \psi_i}{\partial s^L} \right|, \frac{2 |\psi_{i+1} - \psi_i|}{ds_i^L}, \frac{2 |\psi_i - \psi_{i-1}|}{ds_i^L} \right).$$

The gradient is thus

$$D_i = \sigma |D_i|,$$

where σ is the sign of the gradient and is given by

$$\sigma = \begin{cases} \text{sign}(\psi_{i+1} - \psi_i), & \text{sign}(\psi_{i+1} - \psi_i) = \text{sign}(\psi_i - \psi_{i-1}) \\ 0, & \text{otherwise.} \end{cases}$$

The effect of σ is to reduce the gradient to zero when either an extremum is reached, or the gradient doesn't agree with the trend set by adjacent cells. The overall effect of Van Leer's gradient limiters is to suppress numerical oscillations associated with classical second-order schemes.

2.6.3 Multi-material remap of Fluid variables

An interface exists either in a mixed cell, or at the boundary between a cell which contains a material which its neighbour lacks. Once an interface has been located it must be determined which of the materials - which need not be all of those present - needs to be remapped. Recalling the three point stencil required to calculate the gradient (2.40), if one of the materials is absent from one of the cells in the stencil, then the gradient would be unrealistically skewed. Although it may be possible to weight the gradient calculation to counteract this effect, this code reduces to a first order donor-acceptor remap when the gradient cannot be properly constructed. It should be noted that a second order approximation to the gradient - which possesses a smaller stencil - could be tried before resorting to the first order method. This has yet to be tested.

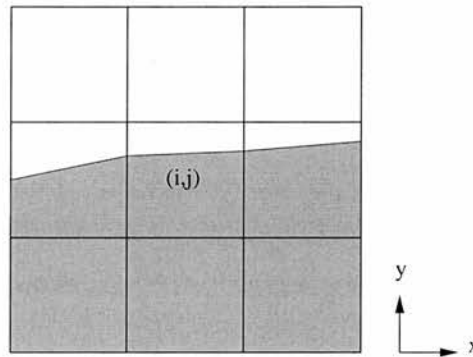


Figure 2.13: Example of a multi-material region for stencil (2.40a) where $u_x, u_y > 0$.

So, mixed cells are located, the materials which need to be remapped are identified and a decision is made as to whether a second or first order remap is to be performed. Consider Figure 2.13, assuming $u_x, u_y > 0$ all the necessary cells for the stencil of (2.40a) on cell (i, j) are shown. In the y -direction certainly the light, and possibly the dark material need to be remapped. This would be a donor-acceptor remap since the light material is absent from cell $(i, j - 1)$. However, in the x -direction both light and dark materials need to be remapped, and essentially the remap of fluid variables outlined in section 2.6.1 can be used.

The portion of the volume flux δV occupied by each material δV_m is calculated by an interface tracking algorithm. Naturally $\sum_{m=1}^n \delta V_m = \delta V$ for n materials. Such algorithms are discussed in more detail in Chapter 3. The volume remap for each material

is

$$(\phi_{i,m})^{n+1} dsb_i = (\phi_{i,m})^n dsb_i^L + dV_{i-1,m} - dV_{i,m}. \quad (2.41)$$

Figure 2.14 gives an example of a donor-acceptor remap using SLIC type V (see Figure

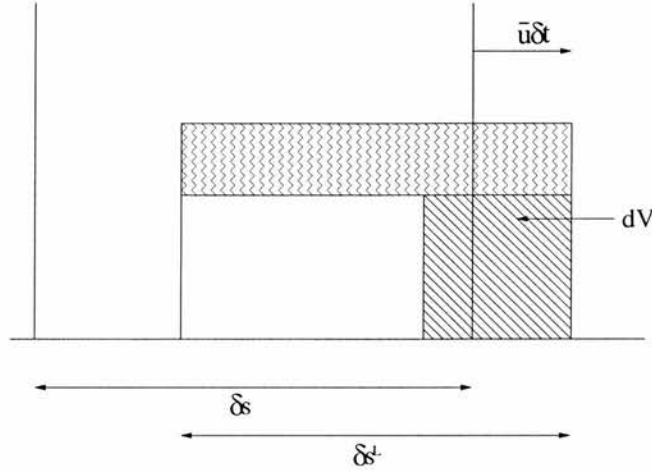


Figure 2.14: Multi-material remap of volume: showing a mixed Lagrangian cell (SLIC Type IV) whose bulk motion is to the right of the Eulerian cell.

3.3), here the light material contributes nothing to δV .

Mass fluxes are computed

$$dM_{i,m} = \begin{cases} \left(\rho_{i,m}^L + \frac{dsb_i^L}{2} D_i (1 - \kappa_{i,m}) \right) \bar{u}_i \delta t, & \bar{u}_i > 0 \\ \left(\rho_{i+1,m}^L + \frac{dsb_{i+1}^L}{2} D_i (1 - \kappa_{i,m}) \right) \bar{u}_i \delta t, & \bar{u}_i \leq 0, \end{cases} \quad (2.42)$$

where

$$\kappa_{i,m} = \begin{cases} \frac{dV_{i,m}}{\phi_{i,m} V_i}, & \bar{u}_i > 0 \\ \frac{dV_{i,m}}{\phi_{i+1,m} V_{i+1}}, & \bar{u}_i \leq 0, \end{cases}$$

and

$$D_i = \begin{cases} 0, & \text{donour-acceptor remap} \\ \sigma |D_i|, & \text{second order remap.} \end{cases}$$

The calculation of $|D_i|$ still uses $\kappa = |\bar{u}|dt/ds^L = dV/V$. The mass remap is therefore

$$(\phi_{i,m})^{n+1}(\rho_{i,m})^{n+1}dsb_i = \phi_{i,m}\rho_{i,m}^L dsb_i^L - dM_{i,m} + dM_{i-1,m}. \quad (2.43)$$

The specific energy remap follows in an analogous manner from that in Section 2.6.1. An individual material's mass flux $dM_{i,m}$ is used as the mass coordinate for that material's specific energy remap. Since the velocity is associated with the grid rather than having individual material velocities, the momentum remap is the same as before, with

$$dM_i = \sum_{m=1}^n dM_{i,m},$$

which is again averaged to the appropriate control volume.

2.6.4 Magnetic flux remap

Although the solenoidal condition is an initial constraint, any numerical scheme must enforce $\nabla \cdot \mathbf{B} = 0$ at each timestep. There are three standard approaches to this problem, Powell's fix (Powell, 1994), the projection method and constrained transport techniques. A comparison between these approaches in various guises is reported in Tóth (2000). Powell's fix uses a set of equations derived without using $\nabla \cdot \mathbf{B} = 0$. These equations contain source terms proportional to $\nabla \cdot \mathbf{B}$. In effect, the magnetic monopoles propagate with the flow, rather than accumulating at a fixed point. The non-conservative source terms can produce errors with problems containing strong shocks. The projection method (Brackbill and Barnes, 1980), (Bell et al., 1989) - also used in incompressible hydrodynamics - corrects a scheme's approximation of the magnetic field \mathbf{B}^* to a projected divergence free magnetic field \mathbf{B}^{n+1} . Let $\mathbf{B}^* = \nabla \wedge \mathbf{A} + \nabla \phi$ where $\nabla \wedge \mathbf{A}$ contains the physically relevant parts of \mathbf{B}^* . This reduces to

$$\nabla \cdot \mathbf{B}^* = \nabla^2 \phi. \quad (2.44)$$

Then $\mathbf{B}^{n+1} = \mathbf{B}^* - \nabla \phi$ where $\nabla \cdot \mathbf{B}^{n+1} = 0$. The difficulties with this method are the numerical cost of solving (2.44), and the possible constraints the Poisson solver imposes on the boundary conditions for \mathbf{B}^{n+1} .

The present code uses a constrained transport technique proposed by Evans and Haw-

ley (1988). This approach has been adapted for non-staggered grids (Tóth, 2000) and to higher order (Ryu et al., 1998), (Londrillo and Del Zanna, 2000). The constrained transport method forces $\int \mathbf{B} \cdot d\mathbf{S} = \text{constant}$ where S is a cell surface in three dimensions. If this condition is met initially, then $\nabla \cdot \mathbf{B} = 0$ is maintained to machine precision for all time.

The net flux through a closed surface bounding a numerical cell must be zero, so $\Phi_{i+1/2,j,k} + \Phi_{i,j+1/2,k} + \Phi_{i,j,k+1/2} - \Phi_{i-1/2,j,k} - \Phi_{i,j-1/2,k} - \Phi_{i,j,k-1/2} = 0$. This constraint is forced by ensuring that if flux originally departed a cell via one cell face now departs via a different cell face, then that amount of flux is subtracted from the cell it originally entered and added to the cell it subsequently enters. In this way all of the magnetic flux is accounted for, none can be created or destroyed. A 2D illustration of this process is given in Figure 2.15.

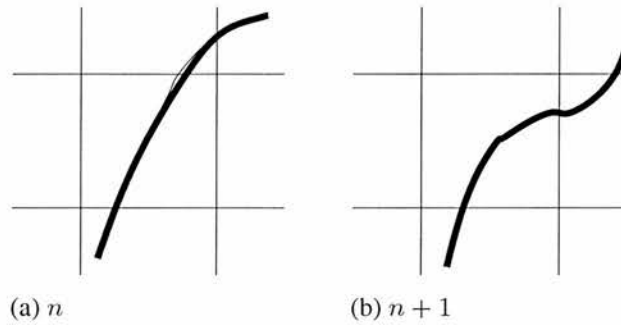


Figure 2.15: The evolution of an isolated flux tube passing through a cell.

Mathematically, for the y flux ($d\Phi_y$) in the x-remap the scheme requires

$$\begin{aligned}\Phi y_{i,j,k}^{n+1} &= \Phi y_{i,j,k} - d\Phi y_{i,j,k} \\ \Phi y_{i+1,j,k}^{n+1} &= \Phi y_{i+1,j,k} + d\Phi y_{i,j,k} \\ \Phi x_{i,j,k}^{n+1} &= \Phi x_{i,j,k} + d\Phi y_{i,j,k} \\ \Phi x_{i+1,j,k}^{n+1} &= \Phi y_{i+1,j,k} - d\Phi y_{i,j,k},\end{aligned}$$

where $\Phi y = B_y dx dz$; the calculation of $d\Phi y$ follows the calculation of dM - the mass flux for the density remap - except that since Φ is face centred, a control volume centred on this edge is used. It is the exact cancellation of $d\Phi y_{i,j,k}$ above which maintains the solenoidal condition to machine precision. Similar conditions hold for $d\Phi z$ in the x-remap and likewise for the remaining remaps.

2.7 Summary

The Lagrangian step is multi-dimensional, and second order accurate except at discontinuities. Shocks are accurately resolved by applying artificial viscosity only in the vicinity of the shock front. Contacts, or material boundaries, are resolved in one cell by using an interface tracking algorithm, examples of which are discussed in chapter 3.

The remap is second order accurate (except at interfaces), and one dimensional. Strang splitting is used to make the remap step multi-dimensional. The magnetic field remap is carried out on the magnetic fluxes using a constrained transport method. This ensures that the solenoidal condition is satisfied to machine precision.

The Lagrangian-remap technique is well suited to low beta plasmas, such as that found in the Corona, since this technique accurately calculates the local plasma temperature. Although not written in conservative form, this code conserves mass and momentum to machine precision. The remap step cannot conserve both momentum and kinetic energy, a correction is made so that kinetic energy is conserved to machine precision. Total energy is only conserved in the absence of any magnetic field, otherwise errors are incurred associated with the magnetic tension force. Each material can possess its own equation of state, and “Equal expansion” governs the mixing of materials.

As always improvements are possible, a limited edge centred artificial viscosity should improve shock resolution, and upwinded constrained transport techniques have been reported. More significantly, a two dimensional corner-coupled remap would be possible. Although this does not improve the accuracy of the code, it would preserve any symmetry and be more computationally efficient, particularly with an interface tracking code. Since the basic unit of this numerical scheme is cell volume rather than cell width, it would be possible to use polar as well as Cartesian co-ordinates by including terms of the form $1/r^{\delta-1}$ (where $\delta = 1$ - Cartesian, $\delta = 2$ - Polar) in the discretisation of the governing equations. Appropriate care would have to be taken at the pole $r = 0$.

Chapter 3

Interface tracking algorithms

3.1 Introduction

The VOF method for tracking material interfaces has proven to be robust and efficient. This method evolves the volume of each material in a cell with time, rather than tracking the interface directly. The interface is reconstructed from the volume data. The accuracy of the interface then largely depends upon the reconstruction algorithm.

In this chapter two VOF interface tracking algorithms are described. Indication is given, where appropriate, of alternative methods and potential improvements. First SLIC (Simple Line Interface Calculation), a piecewise constant method, is developed, followed by the development of Young's algorithm, a piecewise linear method. The difficulties encountered by these methods and possible solutions are discussed. Finally, a brief word is given to some current interface tracking algorithms. A good overview of current VOF techniques is given in Benson (2002).

3.2 Piecewise Constant Methods

At the beginning of the 1970's the first VOF techniques for multi-material problems were introduced. Two such algorithms are the VOF method (Hirt and Nichols, 1981), and the SLIC method (Noh and Woodward, 1976). The VOF method uses a piecewise constant stair-stepped approximation to the interface geometry. A multi-dimensional stencil is

used, but the interface segments are parallel to one of the grid coordinates. The SLIC method uses a piecewise constant approximation to the interface geometry. Only a one dimensional stencil is used, to extend to multiple dimensions operator splitting must be used. The possibility of more complicated interface approximations is traded for the ability to handle multiple (> 2) materials within a mixed cell.

In the following section an outline of the SLIC method of Noh and Woodward (1976) is given.

3.2.1 The SLIC algorithm

SLIC defines the geometrical image approximating the configuration of up to n materials in a cell, where $n \in \mathbb{N}$. Since SLIC uses only 1D information to construct interfaces, this image will, in general, be different depending upon the transport direction. This effect is illustrated in Figure 3.1, seen in the top row. Note that some slight improvements to the standard SLIC algorithm described below have been made in this code, the interface between materials in the same group is placed so that materials of the same type in neighbouring cells are adjacent. For multi-dimensional codes, the SLIC algorithm can only be used in alternating direction hydrocodes.

The material interfaces are approximated as straight lines which are either parallel or perpendicular to the transport direction. To construct an image, SLIC tests whether cells adjacent in the transport direction contain any of the materials. Consider the case where the transport direction is along the x-axis. The material occupation numbers, IL_m and IR_m , are zero if material m is absent and one if it is present, in the cells to the left and right of the current cell respectively. Naturally, $1 \leq m \leq n$. The material index is the combination $(IL, IR)_m$. There are only four possible material indices, $(IL, IR)_m = (0, 0), (0, 1), (1, 0), (1, 1)$, which define the m^{th} material in the current cell.

Materials which possess the same material index are treated as a single material group. Graphically, this is equivalent to separating the materials within a group by an interface parallel to the transport direction. The position of this interface is determined by the volume fractions of the materials within the same group. Consider the example shown in Figure 3.2, group β consists of a homogeneous mix of materials 2 and 3 in the ratio

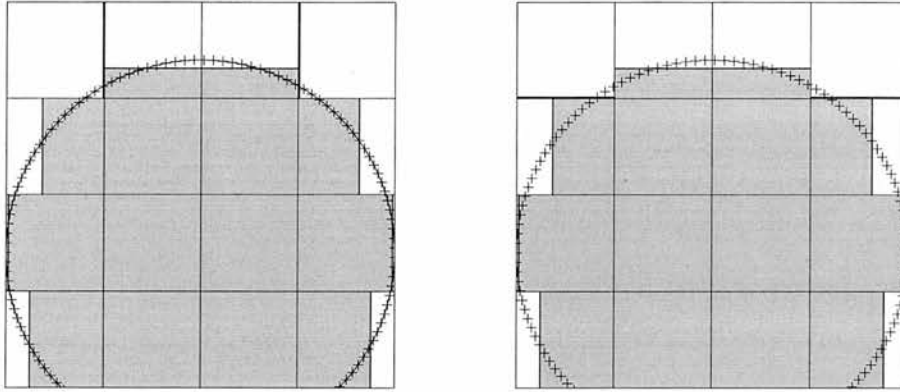


Figure 3.1: The x and y SLIC reconstructions of a portion of a circle

ϕ_2/ϕ_3 . Also $\phi_\beta = \phi_2 + \phi_3$ to conserve volume. In this way a cell containing up to n materials is transformed into a cell containing at most four (since there are only four possible material indices) material groups.

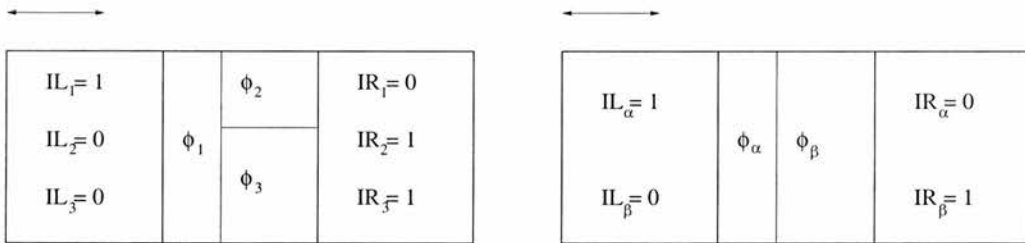


Figure 3.2: A cell with three materials, and SLIC's representation of the cell where materials two and three - which possess the same material index - are combined as material β .

The version of the SLIC algorithm presented here permits six images or material configurations. These are depicted in Figure 3.3.

Type I depicts the single material group configuration, whereby each of the materials has the same material index.

Type II shows the more common (10 out of 16 permutations) two material group configuration. One of the material groups has material index $(0, 1)$ or $(1, 0)$, the other material group is positioned as illustrated, irrespective of its material index.

The remaining two material group configuration is Type III. This configuration occurs

with the presence ($\phi \neq 0$) of a material group with material index $(0, 0)$, which is positioned in the centre of the cell. The other material group is allocated evenly either side of the central material group.

Type IV also occurs with the presence of a material group with index $(0, 0)$. This is again placed in the centre. The other two material groups $[(1, 0), (0, 1)], [(1, 1), (0, 1)], [(1, 0), (1, 1)]$ are placed either side -perpendicular to the transport direction- of the central material group. One or other of these material groups must have index $(1, 0)$ or $(0, 1)$, this is placed adjacent to the cell containing the same material group.

The 'T' configuration contains three material groups, with material indices $(1, 0)$, $(0, 1)$ and $(1, 1)$. The material group with index $(1, 1)$ is positioned with its interface parallel to the transport direction.

The four material group configuration possesses all possible material indices.

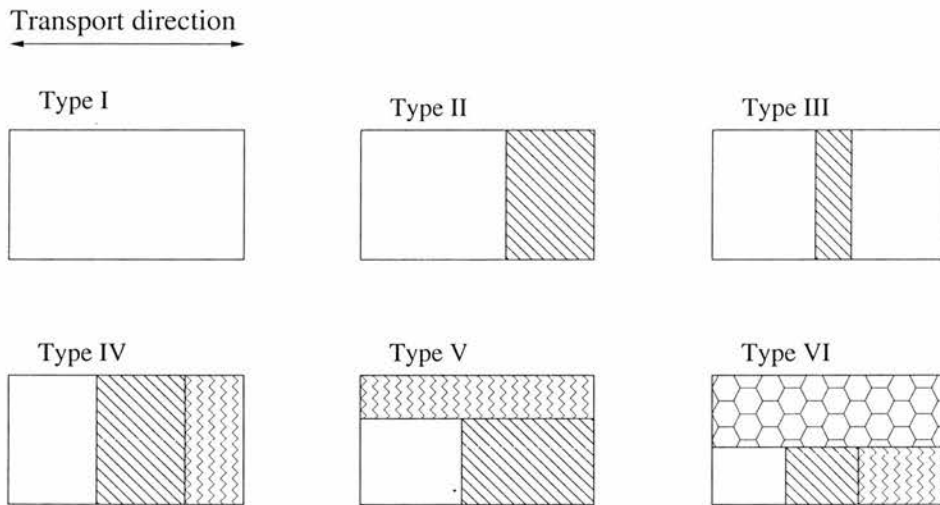


Figure 3.3: The six material configuration types recognised by SLIC.

In any of the configurations, each of the material groups occupies the correct volume. This fact determines the precise location of the interfaces between material groups. It should be remembered that material occupies the correct volume within the material group.

Interfaces between material groups which are perpendicular to the transport direction are preferred, advecting one material group at a time helps prevent unphysical diffusion. Such diffusion leads to an increase in the number of mixed cells, and a subsequent de-

crease in the efficiency of the algorithm.

Summary

The SLIC algorithm is 1D in space. To approximate any interfaces in a multi-material region of 2 or 3 dimensions is simply achieved by an alternating direction method (Strang, 1968). Any number of materials can be approximated in a single cell, and there exists only six material group configurations which depend upon the transport direction. The number of different materials in a cell can change with time, allowing materials to break up or collisions between materials to occur.

3.2.2 Difficulties with Piecewise constant Methods

A distinctive difficulty, which piecewise constant VOF methods suffer from, is the non-physical creation of flotsam and jetsam. These terms refer to isolated bodies smaller than the cell size, which separate from the main material body due to errors in the interface tracking technique. Such material remnants tend to be created when the flow possesses significant vorticity and/or shear.

Take, for example, the Rayleigh-Taylor instability. The top fluid has a density of 2 whilst the lower fluid has a density of 1, $g = 0.1$ acts in the negative y-direction. The initial pressure is hydrostatic and chosen to give a large Mach number, (the flow is therefore nearly incompressible). The interface is perturbed by

$$u_y = \frac{A}{4}(1 + \cos(4\pi x))(1 + \cos(3\pi y)).$$

Flotsam and jetsam can be seen in the left hand image in Figure 3.4. Also discernable is high frequency noise along the material interface in this image as well as more dissipation than the right hand image. The left hand image is a simulation using the SLIC algorithm, the right hand image is performed with a piecewise linear method.

The existence of flotsam and jetsam near the main material interfaces severely compromises the main solution. Such fragments may also be transported at the incorrect speed. The creation of additional mixed cells also increases computational overhead.

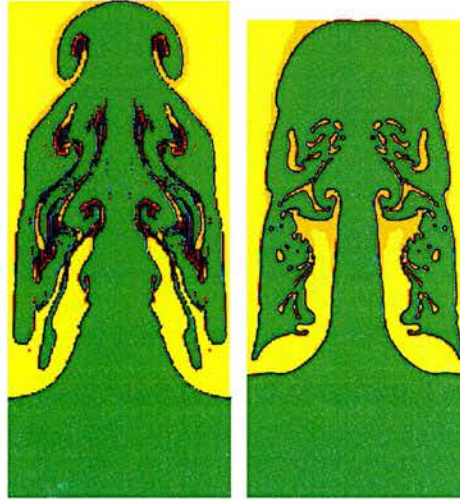


Figure 3.4: Rayleigh-Taylor instability at $t = 12.5$ with the SLIC and Youngs algorithms respectively.

3.3 Piecewise linear Methods

Interface reconstruction techniques were advanced by the use of piecewise linear schemes developed by Youngs (1982). In this method the interface line is defined by a slope and an intercept. The slope is found from the interface normal, and the intercept follows from volume conservation. This technique has been extended to three dimensions (Youngs, 1987).

In the following sections an outline of the two dimensional Youngs scheme is given and, in addition, some of the recent developments of PLIC methods are indicated. Finally, a brief mention is given to some of the new interface tracking techniques.

3.3.1 Youngs algorithm

Outlined in this section is a two dimensional scheme where interfaces are lines rather than planes. Indication is given, where appropriate, of the extensions necessary for three dimensions. To begin with, consider the case with just two materials named dark and

light for convenience. The interface between dark and light materials is prescribed by the volume fractions ϕ_m and an inward pointing normal from the dark materials perspective. Together, these define a straight line given by

$$\mathbf{n} \cdot \mathbf{x} - d = 0, \quad (3.1)$$

which is the approximation to the interface. Youngs method uses a multi-dimensional algorithm to determine the interface normal \mathbf{n} , which is independent of the transport direction (this algorithm uses a 9 point stencil in 2D, a 27 point stencil in 3D). Once the normal is known, the position of the line is moved in such a way that the normal is preserved and the line divides the cell into two volumes which are identical to the volume fractions of the dark and light materials.

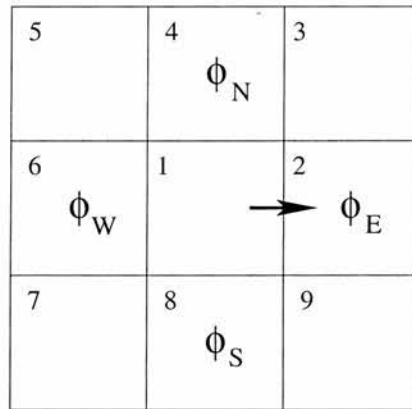


Figure 3.5: The stencil for Young's method for calculating the interface normal. The arrow indicates the transport direction.

The grid is rotated so that the transport direction is to the right in Figure 3.5 (ie. cell 1 is the donor and cell 2 is the acceptor). The variables $\phi_N, \phi_E, \phi_S, \phi_W$ are given by

$$\phi_N = \frac{1}{4}(\phi_3 + 2\phi_4 + \phi_5) \quad (3.2)$$

$$\phi_E = \frac{1}{4}(\phi_3 + 2\phi_2 + \phi_9) \quad (3.3)$$

$$\phi_S = \frac{1}{4}(\phi_7 + 2\phi_8 + \phi_9) \quad (3.4)$$

$$\phi_W = \frac{1}{4}(\phi_5 + 2\phi_6 + \phi_7), \quad (3.5)$$

where all of the above volume fractions are for the dark material only. The gradients are simply

$$\frac{\partial \phi_1}{\partial x} = \phi_E - \phi_W \quad (3.6)$$

$$\frac{\partial \phi_1}{\partial y} = \phi_N - \phi_S. \quad (3.7)$$

Earlier, the tags dark and light were arbitrarily chosen. Since the case of the dark material occupying the majority of the cell on one side of the interface is identical to the case where the light material occupies the majority of a cell with the same interface, the tags dark and light are swapped so that the dark material occupies the smaller volume. That is, if $\phi_1 > 1/2$, then

$$\begin{aligned} \phi_1 &= 1 - \phi_1 \\ \frac{\partial \phi_1}{\partial x} &= -\frac{\partial \phi_1}{\partial x} \\ \frac{\partial \phi_1}{\partial y} &= -\frac{\partial \phi_1}{\partial y}. \end{aligned}$$

The inward pointing normal to the dark material is

$$(\hat{n}_1, \hat{n}_2) = \left(\left(\frac{\partial \phi_1}{\partial x} \right)^2 + \left(\frac{\partial \phi_1}{\partial y} \right)^2 \right)^{-1/2} \left(\frac{\partial \phi_1}{\partial x}, \frac{\partial \phi_1}{\partial y} \right)$$

The interface normal is now defined, the position of the interface such that the volume occupied by the dark material equals its volume fraction must now be found.

Rather than considering an arbitrary line (or plane in three dimensions) intersecting a cell, various symmetry arguments are used to limit the possibilities to two configurations (five configurations in three dimensions). Each vertex of the mixed cell is uniquely labelled by the variable \bar{c} , the cell edges are uniquely labelled by the sum of \bar{c} connecting the corners of that edge. The interface is removed from the cell and guided towards the cell along the normal direction until it reaches a corner. This corner is labelled P'_0 and $c'_0 = \bar{c}$ for this corner. The motion is continued until a second corner is reached, this corner is labelled P'_1 and $c'_1 = \bar{c}$ for this corner. The cell is mapped onto a unit cell with the line $P'_0 P'_1$ constituting the x-axis with P'_0 the origin. The direction of the acceptor cell is required in this geometry. If the unit cell is rotated about π and $x_1 = \min(|n_1|, |n_2|)$,

$x_2 = \max(|n_1|, |n_2|)$, then there exists only two possibilities for the resulting cell.

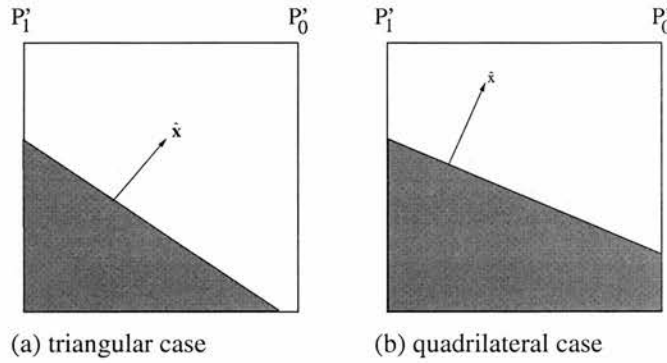


Figure 3.6: The two possible cases, after translation, for a line to intersect a cell.

The direction of the acceptor cell - also known as the exit face - is found uniquely by considering the sign of n_1 and the sum $c'_0 + c'_1$. An example is shown in Figure 3.7.

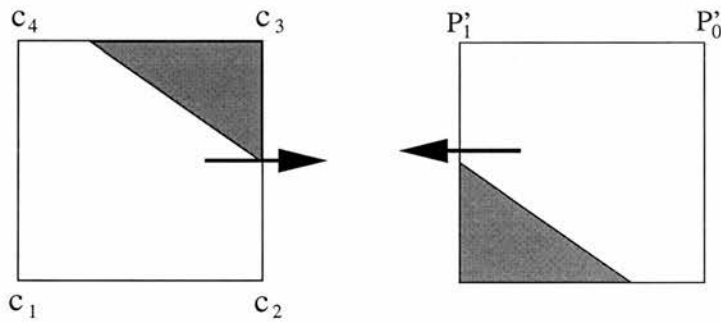


Figure 3.7: An example showing the initial and translated orientations of a cell.

After all of these translations, the result is one of two possible geometries for the cell, with the exit face known. The five possible configurations in three dimensions are illustrated in Figure 3.8.

The interface must be positioned so that the area formed below it for each of the two possible cases, matches the volume fraction for the dark material. Consider first the triangular case.

The triangular case occurs when $h_1 \leq 1$. The area of the triangle must equal the volume

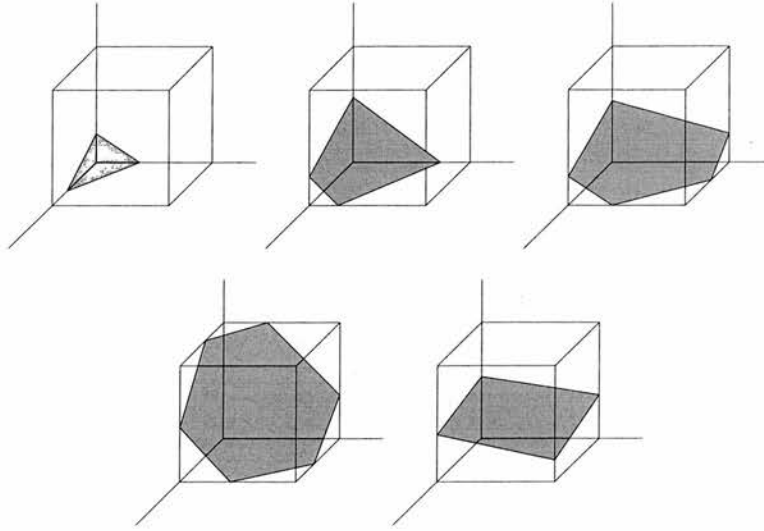


Figure 3.8: The five possible cases, after translation, for a plane to intersect a cell.

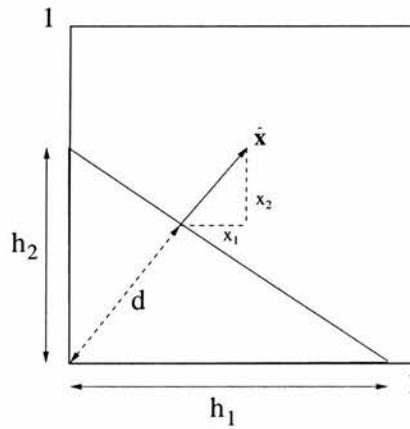


Figure 3.9: The triangular case.

fraction, this determines d in (3.1).

$$\phi_1 = \frac{1}{2}h_1h_2 = \frac{1}{2} \frac{d^2}{x_1x_2} \Rightarrow d = (2x_1x_2\phi_1)^{1/2}.$$

The quadrilateral case occurs when $h_1 > 1$.

The area below the interface must equal the volume fraction.

$$\phi_1 = ((h_2 - h') \times 1) + \left(\frac{1}{2}h' \times 1\right)$$

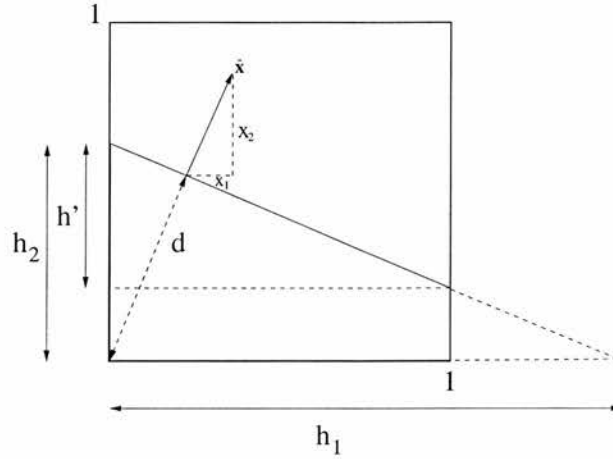


Figure 3.10: The quadrilateral case.

$$\begin{aligned}
 &= h_2 - \frac{h'}{2} \\
 &= \frac{d}{x_2} - \frac{x_1}{2x_2} \\
 \Rightarrow d &= x_2 \phi_1 + \frac{x_1}{2}.
 \end{aligned}$$

The line defining the interface in two dimensions and its relation to the transport direction are known, since the fraction of the cell to be remapped is also known it is simple to calculate the volume of the dark material to be remapped (dV_{dark}).

To simulate problems involving more than two materials, the ability to handle multiple interfaces within a cell is required. To achieve this, the so called *onion skin* model is used (see Figure 3.11(b)). Consider a mixed cell which contains $n > 2$ materials for some $n \in \mathbb{N}$. The first interface lies between materials one and two, and is calculated by placing the volume of material one (M_1) behind the interface. The second interface - which lies between materials two and three - is calculated by placing the sum of the volumes of materials one and two ($M_1 + M_2$) behind the interface. This process is continued until material $n - 1$ is reached.

The *onion skin* model assumes there are $n - 1$ interfaces for n materials in a mixed cell. The *onion skin* model is incapable of reproducing T-joins (see Figure 3.11(a)) or triple points. Moreover, it is impossible to guarantee that two interfaces will not intersect within a cell.

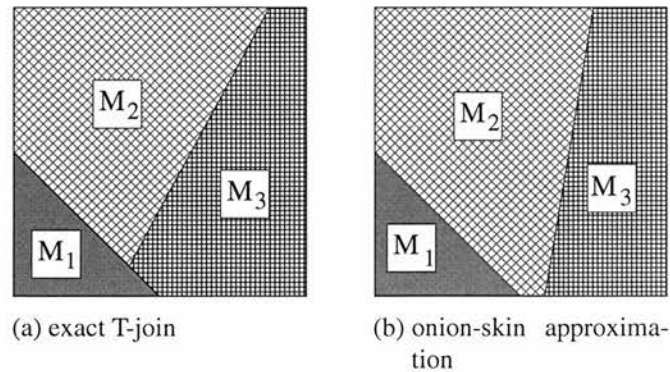


Figure 3.11: An example of a mixed cell possessing a “T-join”, and the *onion skin* representation of that same cell.

Summary

The Youngs algorithm is multi-dimensional, and any number of materials can be present in a single mixed cell using the *onion skin* model. However, T-intersects of interfaces are not possible, nor is the interface continuous across cell boundaries. A nine point stencil is used to calculate the interface normal. The reconstructed interface is placed such that the areas it divides the cell into match the volume fractions of the materials the cell contains, so that material volumes are conserved. Symmetry arguments are used to restrict the number of configurations considered to two. To extend to three dimensions a twenty seven point stencil is required to calculate the interface normal, and after similar symmetry arguments it is necessary to consider only five configurations.

3.3.2 Further developments of PLIC methods

First, reconsider the Rayleigh-Taylor instability presented in section 3.2.2. Figure 3.12 contains three images, on the left depicting a single material case, in the centre depicting a two material case, and on the right depicting a single material case at double the resolution of the other two simulations. The single material case is clearly the most dissipative, but develops at the correct speed. The multi-material case exhibits very little dissipation, whereas the single material case at double the resolution still displays some dissipation as well as some additional features. The indent seen in the centre of the rising material for both single material cases, is absent from the multi-material case. A similar Raleigh-Taylor configuration is discussed in Liska and Wendroff (2001).

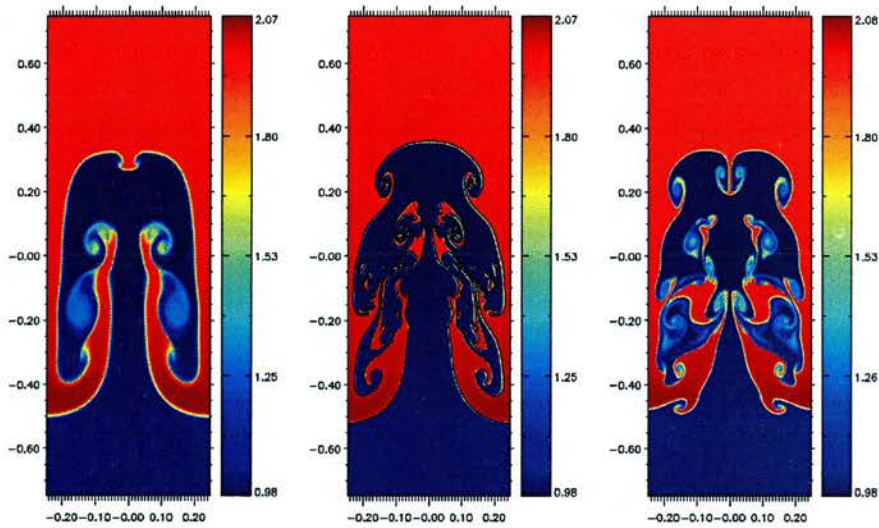


Figure 3.12: Contours of density for the Rayleigh-Taylor problem, with the single material, multi-material, and double the resolution single material simulations respectively.

Interface normal calculation

Youngs algorithm uses straightforward finite difference approximations for the volume fraction gradient (3.6)-(3.7) to define the interface normal. This is robust but is incapable of reproducing all linear interfaces exactly. According to Pilliod and Puckett (1999), a second order accurate interface reconstruction method should exactly reproduce straight lines. Consider the line $y = 2x/3 + \delta$ shown in Figure 3.13 along with the volume fraction information. Equations (3.2)-(3.5) yield

$$\begin{aligned}\phi_N &= \frac{1}{4} \left(\frac{2}{3} + \frac{1}{6} + 0 \right) \\ \phi_E &= \frac{1}{4} \left(\frac{2}{3} + 2 + 1 \right) \\ \phi_S &= \frac{1}{4} \left(1 + 2 + 1 \right) \\ \phi_W &= \frac{1}{4} \left(0 + 2\frac{1}{3} + 1 \right),\end{aligned}$$

giving

$$\frac{\partial \phi}{\partial x} = \frac{6}{12}, \quad \frac{\partial \phi}{\partial y} = -\frac{19}{24}.$$

The gradient of Youngs reconstructed interface is

$$m_Y = \frac{-\partial \phi / \partial x}{\partial \phi / \partial y} = \frac{12}{19},$$

whereas the correct gradient is $m = 2/3$.

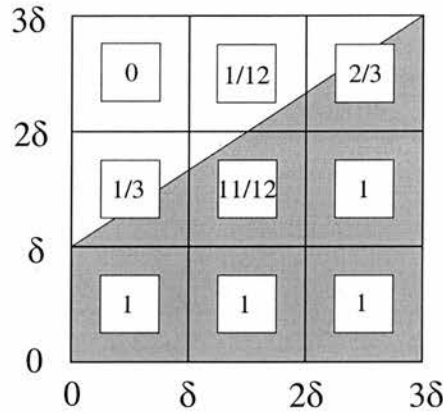


Figure 3.13: An example of a multi-material region - with volume fraction data - where Young’s interface stencil fails to reproduce a straight line exactly.

The approximation to the gradient is independent of δ , implying that the approximation to the gradient does not improve with grid resolution.

Several alternatives to (3.6)-(3.7) have been suggested, Pilliod and Puckett (1999) proposed two algorithms (LVIRA/ELVIRA) both of which reproduce straight lines exactly. LVIRA minimises the discrete L^2 error between the volume fractions contained in the nine point stencil under the constraint that the approximate interface exactly reproduces the volume fraction in the donor cell. A less expensive approach is ELVIRA, which chooses from among six candidates for the volume fraction gradient. This choice is determined by minimising the L_1 or L_2 norms over the six candidates. Rider and Kothe (1998) has reported another algorithm which preserves linear interfaces based upon the work of Swartz (1989). This iterative procedure uses Youngs algorithm as an initial guess for \mathbf{n} and uses interfaces in neighbouring mixed cells constructed with this \mathbf{n} to calculate a new guess for the interface normal \mathbf{n}_{new} . This is repeated until \mathbf{n} and \mathbf{n}_{new} differ

by less than some prefixed tolerance. This algorithm, like LVIRA can be prohibitively expensive, especially in three dimensions.

These algorithms are more accurate than (3.6)-(3.7), and reproduce linear interfaces exactly, however on coarse grids, Youngs method for calculating the interface normal produces more accurate results for curved interfaces.

Interface continuity

Since Youngs algorithm represents the interface as a single straight line within a cell in two dimensions, the result is a jagged edge when two such lines fail to meet at a cell boundary. This is illustrated in Figure 3.14. Some of the more recently developed algorithms attempt to surmount this difficulty. FLAIR (Ashgriz and Poo, 1991) reconstructs piecewise linear interfaces across cell boundaries rather than within the cell, resulting in a more continuous interface. It is more difficult to conserve material volume in the cell with the interfaces centred on the cell boundaries.

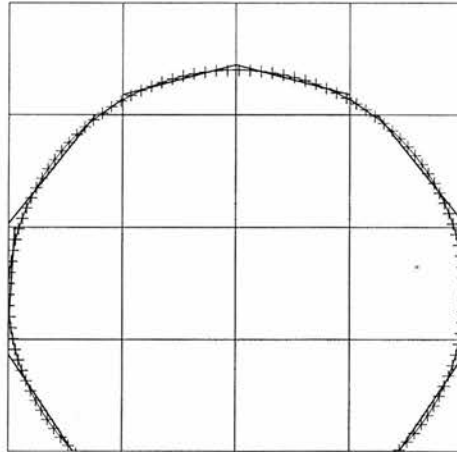


Figure 3.14: Young's reconstruction of a portion of a circle.

HELMIT (Giddings, 2001) can be seen as a post-processor for existing schemes. If, after reconstructing two interfaces in adjoining cells (with, for example, Youngs method)

the interfaces are discontinuous across the common cell boundary, then they are forced to meet (Figure 3.15).

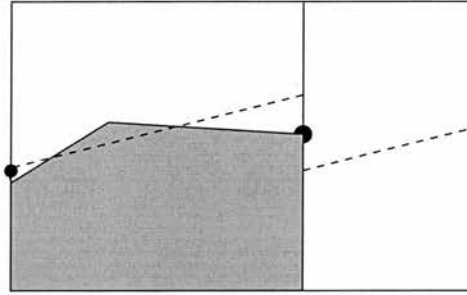


Figure 3.15: A hinged line interface. The dashed line indicates the original Young's interface reconstruction.

The intercepts of the interface with the cell boundaries are known, however simply connecting these points with a straight line will not enclose the correct volume. Instead, each interface consists of two joined line segments. As there is a choice in hinge location, the use of a hinged line permits the representation of T-joins (see the right hand side of Figure 3.16).

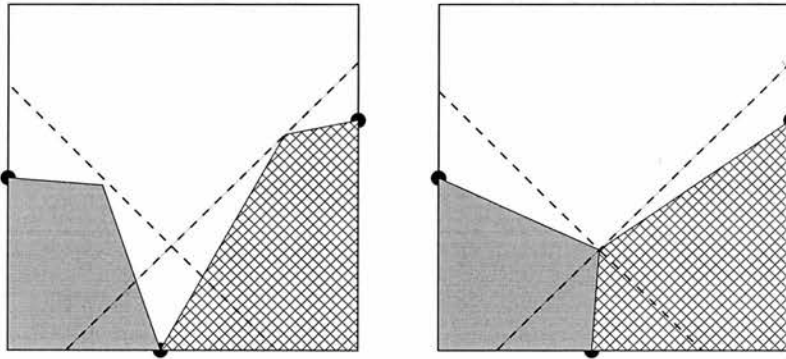


Figure 3.16: HELMIT's ability to construct "T-joins".

Material ordering

The order of the materials used to construct the partial sums in the *onion skin* model for multiple interfaces within a mixed cell can be important. The simplest method is a

fixed ordering or priority list. For example, if the priority list were $[3, 5, 1, 2, 4]$ and a cell contained materials one, three and five, the ordering of the materials is $(3, 5, 1)$. Priority lists suffice for most situations, but they can fail. The most common situation where a priority list fails is the presence of a background material, which should always be placed between any other two materials. Consider the example of three discs surrounded by a fourth material illustrated in Figure 3.17. There is no priority list that places the fourth material between every combination of the remaining three materials. The materials may diffuse into one another (Figure 3.17(a)).

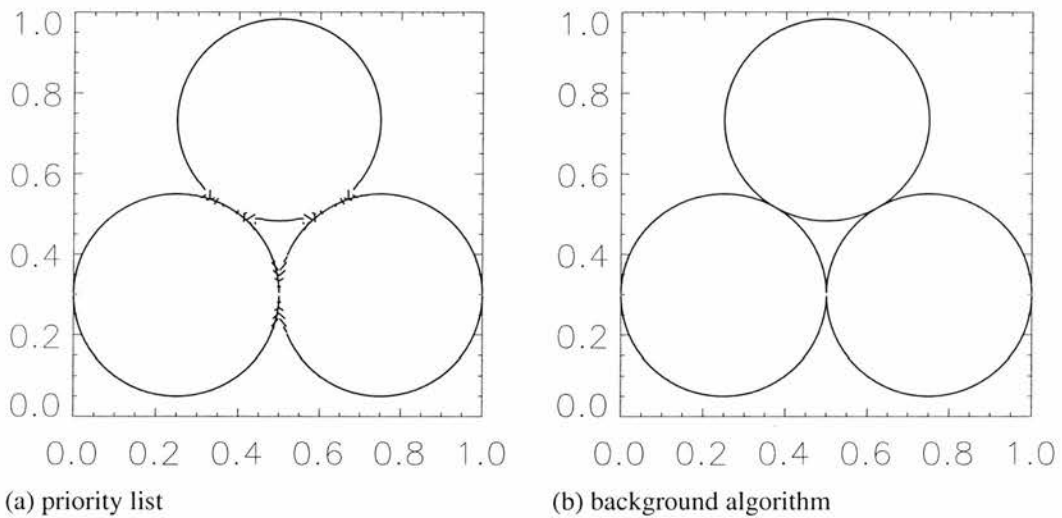


Figure 3.17: The material ordering problem encountered by a fixed priority list, and the improvement gained by a background algorithm.

The background algorithm (Benson, 1998) dynamically assigns the background material - when present - to be second on the adjacency list. The rest of the adjacency list is filled in from the priority list, albeit additional empirical rules are given in Benson (1998). This is only useful when the configuration makes “background” meaningful. This method has been incorporated into the code. Comparing Figure 3.17(b) to Figure 3.17(a), the background algorithm offers a clear improvement over the fixed priority list. The jagged edge seen in Figure 3.17(a) is a result of the material occupying the smallest volume in the advection region being advected first or last. Recently, more general and complex algorithms to calculate the adjacency list have been developed, which, for example, dynamically order the materials by decreasing volume fraction in the downstream cell, or by projecting an estimate of the material centroids onto a line.

3.3.3 New developments

Recently, a number of new interface tracking codes have been reported. Level Set methods (smooth function $\theta(\mathbf{x}, t)$ represents the interface as the set $\theta(\mathbf{x}, t) = 0$) continue to be improved, for a current review see Osher and Fedkiw (2001). Topological changes are well described, and configurations such as T-joins offer no difficulty to Level set techniques.

A VOF interface tracking algorithm has been implemented in a high order Godunov method for multiple condensed phases (Miller and Puckett, 1996), this code also utilises an AMR driver.

A combined marker particle area preserving interface tracking scheme has been reported (Aulisa et al., 2004). The interface is defined by a set of closed lines, markers are placed at the line intersects. The interface is reconstructed and the markers are advected with the flow. A new interface is calculated to conserve area, and new markers are placed at the line intersects for the next timestep. This approach yields good results, but a comparison in terms of computational cost with existing methods has yet to be made. A ghost fluid interaction method has also been reported (Hu and Khoo, 2004).

3.4 Summary

Two interface tracking algorithms have been discussed; SLIC, a piecewise constant method, and Youngs, a piecewise linear method. A number of improvements to Youngs method have been mentioned, including the interface normal calculation, interface continuity, coping with material configurations such as “T-joins”, and the ordering of materials for advection. Possibly the most significant of these is interface continuity. If the interface were continuous it would be simpler to develop a constrained transport technique for a multi-material magnetic field. Other possible improvements include parabolic interface reconstruction, which would give some estimate for interface curvature. It should also be possible to combine interface tracking with AMR, the simplest strategy would be to enforce all cells in the interface normal stencil to be at the highest level of refinement. Since the interface is likely to be an area of interest, this is reasonable.

Chapter 4

Test cases

4.1 Introduction

In this chapter a number of test cases are performed by the multi-material code using Youngs algorithm. These tests are designed to gauge the code's ability to resolve material boundaries or contact discontinuities. For results which test other aspects of the code, for example shock capturing, see Arber et al. (2001). First, a series of advection tests are undertaken, these involve no physics but merely test the reconstruction technique. This is followed by a series of one and two dimensional test problems which all include contact discontinuities, before a couple of multi-material test problems are run.

4.2 Advection tests

4.2.1 Notched circle

The notched circle advection problem, first introduced by Zalesak (1979), consists of a circle with a radius of fifteen cells having a rectangle of dimension 25×5 cells cut out of it. The cut is placed a third of a radius from the top of the circle, and passes through the circle's centre. The notched circle is rotated as a solid body about a point five thirds of its radius below its centre for one revolution. This simulation uses a resolution of $\delta x = \delta y = 0.01$, there is no magnetic field and the void equation of state is used.

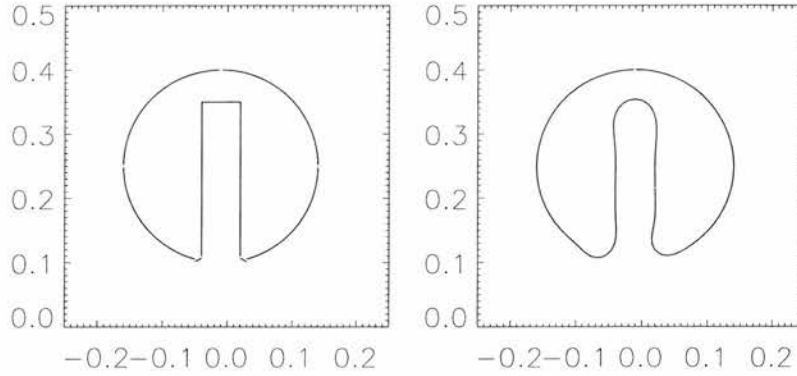


Figure 4.1: The initial notched circle, and the notched circle after one revolution.

The largest error is incurred where the first derivative of the function describing the interface is discontinuous. The slight bulges seen there in Figure 4.1 can be explained by volume conservation: although the sharp corner has been flattened, volume must be conserved and so it is redistributed slightly away from the corner. Improvements to counter this effect include unsplit advection, and are discussed by Pilliod and Puckett (1999).

4.2.2 Single vortex

A circle with radius 0.15 and centre (0.5, 0.75) is placed inside a unit square domain. The numerical grid covers the domain, with resolution 128×128 . Each of the boundaries of the domain are periodic. The volume fraction field is zero or one outside or inside the circle respectively. The volume fraction field for cells containing the interface is set to between zero and one in proportion to the volume of the cell occupied by the circle. Again, the void equation of state is used. A single vortex is imposed with a velocity field defined by the stream function

$$\psi = \frac{1}{\pi} \sin^2(\pi x) \sin^2(\pi y),$$

where

$$u_x = -\frac{\partial \psi}{\partial y} \quad \text{and} \quad u_y = \frac{\partial \psi}{\partial x}.$$

The flow field is also given cosinusoidal time dependence (Leveque, 1996). Thus the flow returns to its initial state after one period T . A quantitative estimate of the error can be made by comparing the solution at $t = 0$ and $t = T$. The velocity field stretches the circle into a spiral about the centre of the domain, wrapping around the centre approximately two and a half times by $t = 3$. This test problem was introduced by Rider and Kothe (1995) and is also discussed in Rider and Kothe (1998)

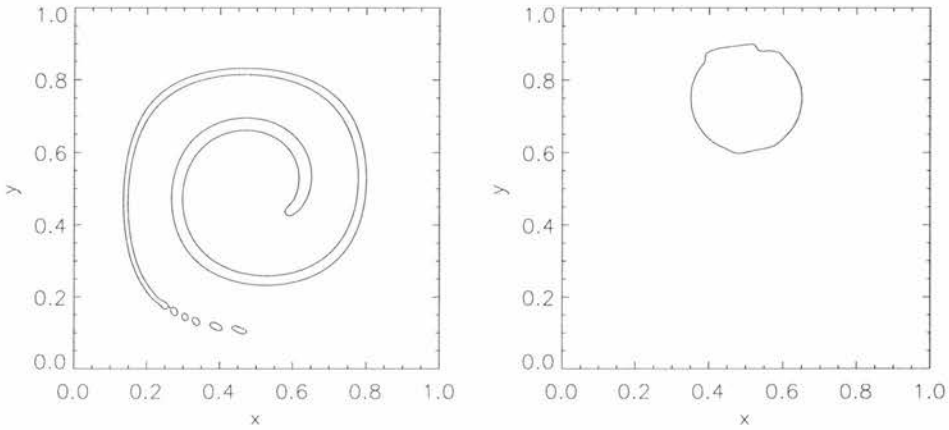


Figure 4.2: Vortex problem at $t = 4$ and $t = 8$ where $T = 8$

The interface reconstruction algorithm flattens high curvature regions, and the developing filament structure of the spiral is broken when the filament width is approximately the same size as a cell width. Because of this, the initial circle is not recreated at $t = 8$, however the interface is continuous at this time.

4.2.3 Deformation field

This uses the same initial conditions as the single vortex problem, but with the stream function

$$\psi = \frac{1}{4\pi} \sin(4\pi(x + 1/2)) \cos(4\pi(y + 1/2)).$$

This flow field possesses sixteen vortices, a large portion of the circle gets trapped by the nearest two vortices, the rest of the circle remains in nearby vortices. Again, this flow is time reversed as with the single vortex problem.

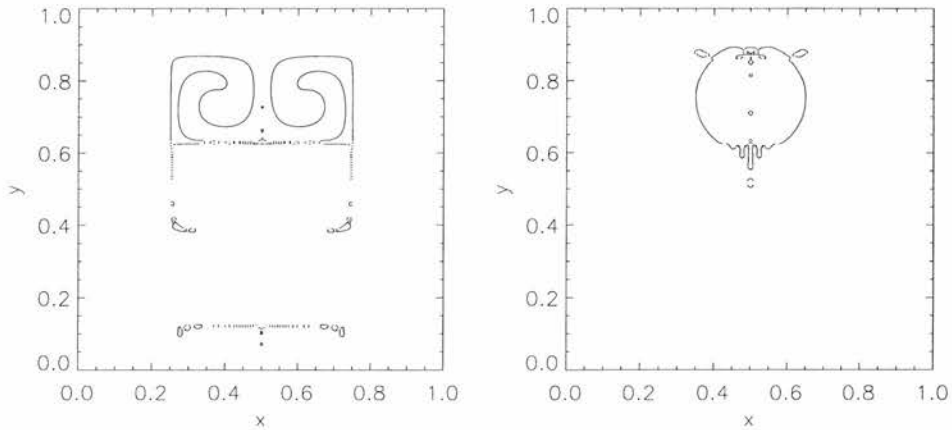


Figure 4.3: Deformation problem at $t = 1$ and $t = 2$ where $T = 2$.

The ability of the deformation field to tear the circle apart is clearly seen in Figure 4.3. The time reversed solution is not of the highest quality, but the original circle is discernable. Flotsam and jetsam are evident, a result of the numerical surface tension. For a discussion of this problem with unsplit time advection, see Rider and Kothe (1998), and for a comparison with other interface capturing and tracking methods (including PPM and Level set techniques) see Rider and Kothe (1995).

4.3 1D tests

4.3.1 1D shock tube problem

This 1D shock tube problem follows the initial conditions presented by Sod (1978). A diaphragm at $x = 0.5$ separates two regions of differing densities and pressures, namely

$$\rho = \begin{cases} 1 & x \leq 0.5 \\ 0.125 & x > 0.5 \end{cases}, \quad P = \begin{cases} 1 & x \leq 0.5 \\ 0.1 & x > 0.5. \end{cases}$$

The velocity in both regions is initially zero. The ratio of specific heats γ is taken to be 1.4 corresponding to air. At $t > 0$ the diaphragm is broken, the simulation is halted at $t = 0.1$ before any wave can reach either boundary.

The solution consists of a rarefaction wave travelling to the left, a contact discontinuity and a shock. Both the pressure and the velocity are continuous across the contact discontinuity contrary to the density and specific internal energy which are not continuous. All the variables are discontinuous across the shock.

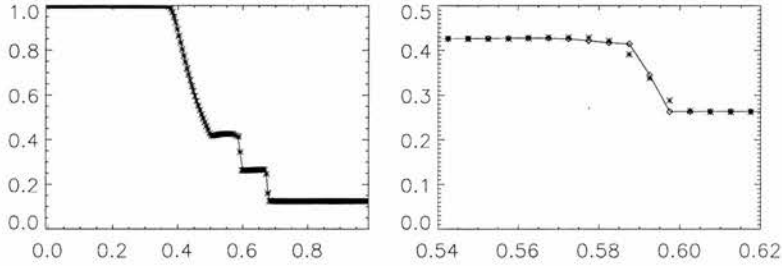


Figure 4.4: Density profile for Sod's problem at $t = 0.1$, with an enlargement of the contact discontinuity.

On the left of Figure 4.4, the density profiles to Sod's problem at $t = 0.1$ calculated using single material (line) and multi-material (symbols) codes at the same resolution of $\delta x = 0.005$, are depicted. In either case two grid points reside in the shock. The slight undershoot at the foot of the rarefaction wave is experienced by both codes. On the right of Figure 4.4, an enlargement of the contact discontinuity is shown. Here, the asterisks show the single material simulation, the joined diamonds show the multi-material simulation. First, the multi-material simulation produces a steeper profile for the contact discontinuity. The slight dip noticeable at the top of the contact discontinuity in the multi-material simulation, is due to the scheme reducing to a donor-acceptor remap near the interface. Weighting the volume fluxes appropriately near the interface would permit a second order remap to be used, this should eliminate this difficulty.

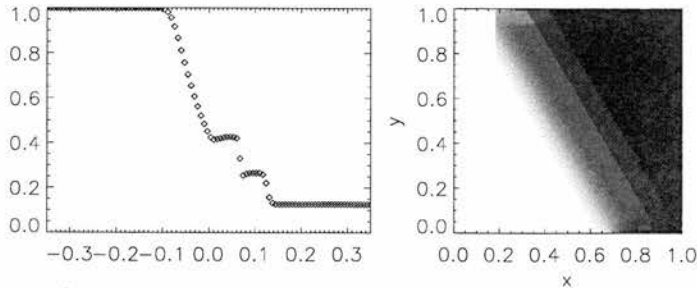


Figure 4.5: Plot and contour of density for the Sod problem, at 45° and 30° respectively.

This problem has been run on a two dimensional grid at angles of 45° and 30° , to check the multi-dimensional nature of Youngs algorithm. Figure 4.5 shows the density profile plotted along the leading diagonal for the 45° case ($\delta x = 0.01$), and a contour plot for the 30° case ($\delta x = 0.00714$), using the multi-material code. Note that both simulations used a castellated initial condition. As with the one dimensional case above, the multi-material code captures the contact discontinuity with one grid point.

4.3.2 Interacting blast waves

This is a more complex 1D test problem involving interactions between strong shocks, rarefactions and contact discontinuities. At $t = 0$ there are three ideal gas states at rest between reflecting walls which are separated by a distance of unity. The ratio of specific heats γ is 1.4 and the density is everywhere equal to one. The three distinct states are defined by the pressure, which is

$$P = \begin{cases} 1000 & 0 < x < 0.1 \\ 0.01 & 0.1 \leq x \leq 0.9 \\ 100 & 0.9 < x < 1.0. \end{cases}$$

Two strong blast waves develop and collide, which produces a new contact discontinuity. For a full description of the development and interaction of the blast waves see Woodward and Colella (1984), here the result at $t = 0.038$ is shown.

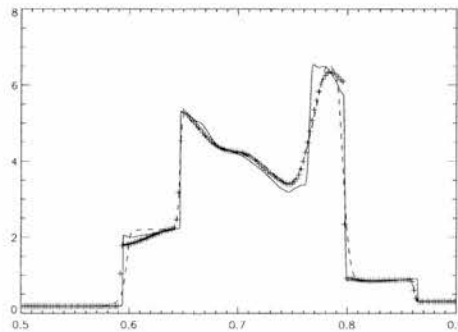


Figure 4.6: Density profile for interacting blast wave problem at $t = 0.038$. Solid line depicts the exact solution (4800 grid points), the dashed line the single material case (1200 grid points) and the symbols the multi-material case (1200 grid points).

Figure 4.6 shows the density and velocity profiles at $t = 0.038$. Two shocks and two contact discontinuities can clearly be made out even after they have passed through each other. The contacts are once again better resolved with the multi-material code. The “exact” solution is provided from a simulation with 4800 grid points.

4.3.3 1.5D MHD shock tube problem

This test case was originally composed by Brio and Wu (1988). It is an initial value problem consisting of two constant states U_L, U_R , the initial states being $(u_x)_L = (u_y)_L = 0$, $\rho_L = 1$, $P_L = 1$, $(B_y)_L = 1$ and $(u_x)_R = (u_y)_R = 0$, $\rho_R = 0.125$, $P_R = 0.1$, $(B_y)_R = -1$, in addition $B_x = 0.75$ and $\gamma = 2$. Note that in the absence of the magnetic field and with $\gamma = 1.4$ this reduces to the well known hydrodynamic shock tube problem of Sod (1978).

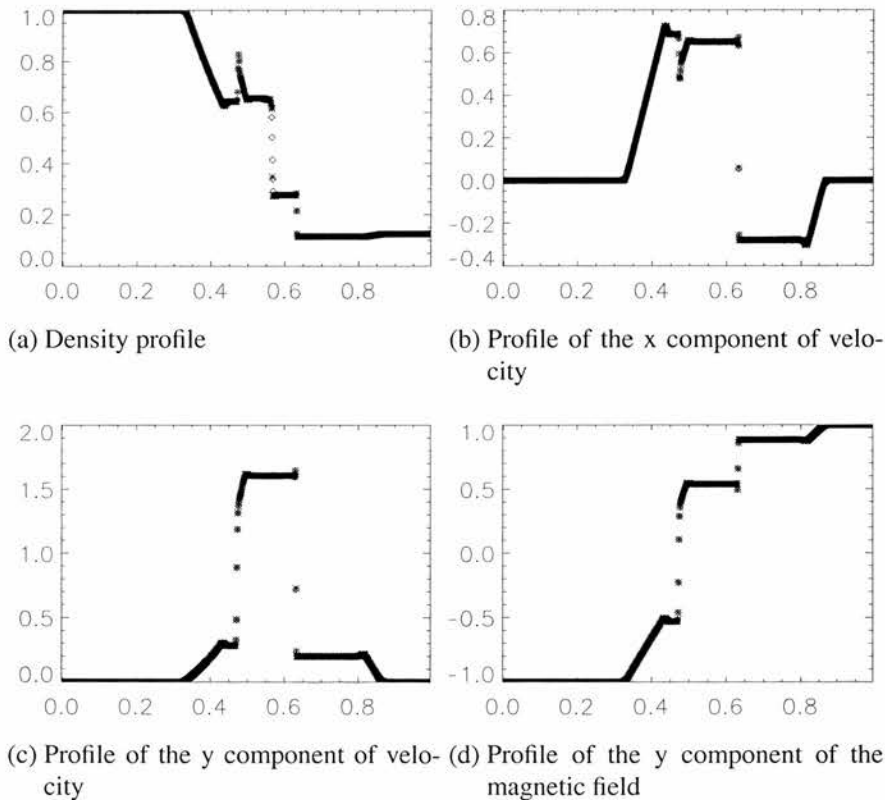


Figure 4.7: Profiles for the Brio & Wu shock tube problem. Diamonds represent the single material code, crosses the multi-material code.

The numerical results shown were obtained using 800 grid points, all the results displayed are at $t = 0.1$. Figure 4.7 gives plots of density, x and y components of velocity and the y component of magnetic field. Focusing on the density profile, travelling to the left one can discern a fast rarefaction wave ($x \approx 0.4$) and a slow compound wave ($x \approx 0.47$), moving to the right is a contact discontinuity ($x \approx 0.55$), a slow shock ($x \approx 0.65$) and another fast rarefaction wave ($x \approx 0.9$). The existence of a compound wave is due to the nonconvexity of the MHD equations (see Brio and Wu (1988) section VI for details), note that the compound wave is located precisely where B_y changes sign. Some overshoot can be seen at the shock in the velocity profiles, this can probably be avoided by a more careful choice of the artificial viscosity coefficients. The diamonds represent the single material code, the crosses the multi-material code. The contact, discernable in the density plot, is better resolved by the multi-material code. The shock, rarefaction waves and compound wave are identical to the single material case.

4.4 2D tests

4.4.1 2D Riemann problem

This two dimensional problem was proposed by Schulz-Rinne et al. (1993), and is also discussed in Lax and Liu (1998). A comparison of several numerical techniques on this test problem is discussed by Liska and Wendroff (2001). A unit square is subdivided into four equal quadrants. All four subsequent 1D Riemann problems contain one contact and no other waves. The initial conditions are

$$\text{Bottom left quadrant: } \rho = 1.0, P = 1.0, u_x = -0.75, u_y = 0.5$$

$$\text{Top left quadrant: } \rho = 2.0, P = 2.0, u_x = 0.75, u_y = 0.5$$

$$\text{Bottom right quadrant: } \rho = 3.0, P = 1.0, u_x = -0.75, u_y = -0.5$$

$$\text{Top right quadrant: } \rho = 1.0, P = 1.0, u_x = 0.75, u_y = -0.5.$$

The simulation is run to $t = 0.3$ with $\delta x = \delta y = 0.0025$. Figure 4.8 displays colour pressure contours, 29 density contours in steps of 0.1 starting at 0.25, and velocity by arrows for the single material case.

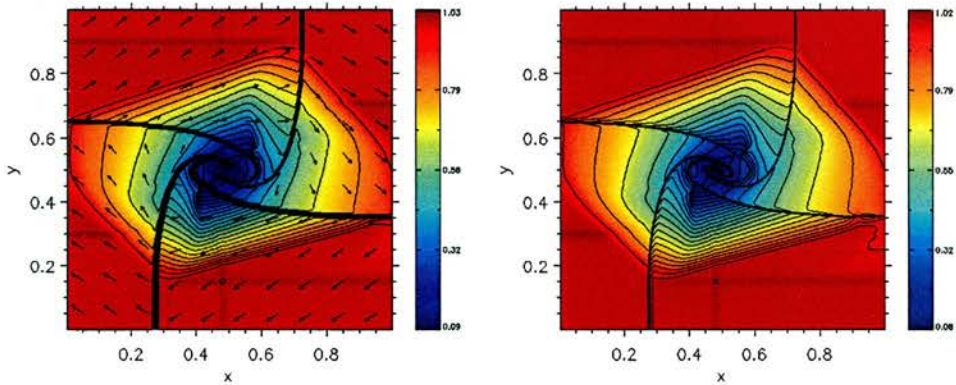


Figure 4.8: Single and multi-material contours of the 2D Riemann problem.

Comparing the single and multi-material cases, Figure 4.8, the multi-material case achieves far greater resolution at the contacts. Both cases exhibit some numerical artefacts seen in the pressure contours.

4.4.2 Implosion problem

This is a converging shock tube problem presented in Hui et al. (1999) and Chang et al. (1999), again a comparison of several numerical techniques for this test case is made by Liska and Wendroff (2001). It is essentially the shock tube problem of Sod (1978) at 45° in a domain with solid wall boundary conditions.

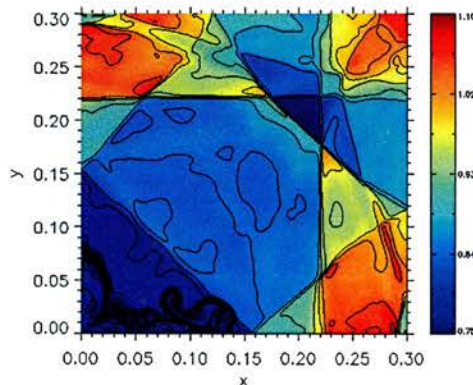


Figure 4.9: Implosion problem with a dimensionally split code.

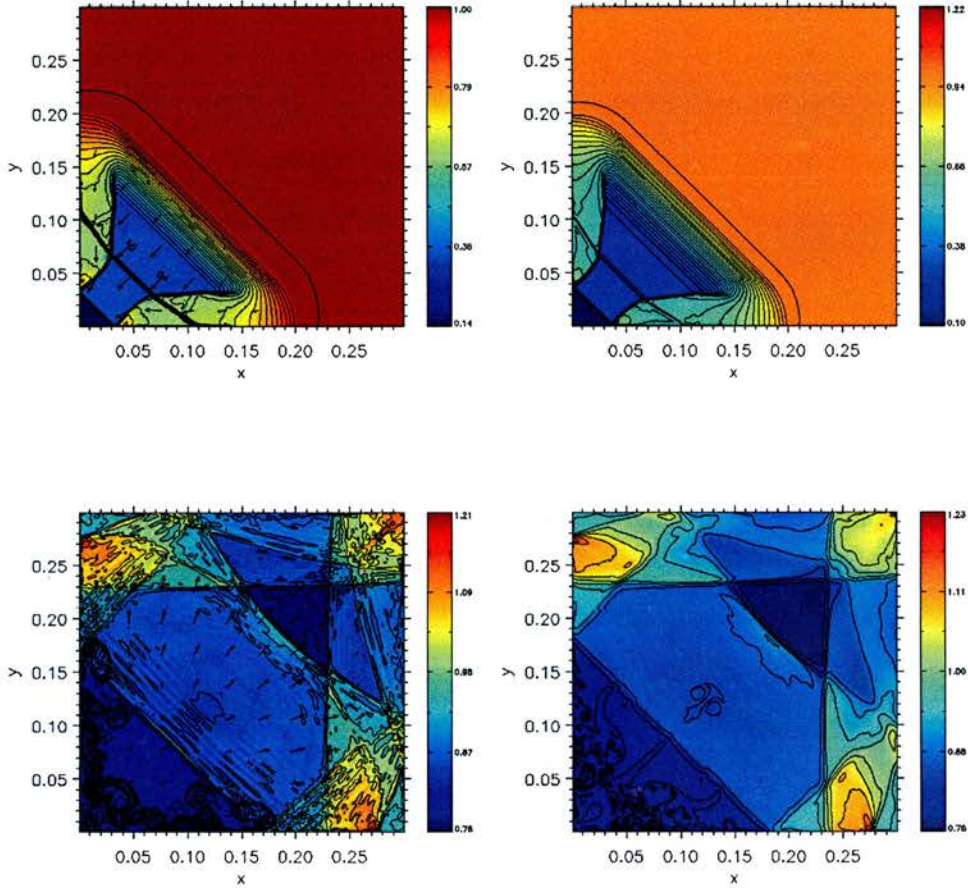


Figure 4.10: Single and multi-material contours for the Implosion problem.

Figure 4.10 depicts this shock problem at $t = 0.045$ and $t = 2.5$, with pressure contours in colour. 36 density contours from 0.125 in steps of 0.025 are shown at $t = 0.045$, at $t = 2.5$ 31 contours from 0.35 with the same step are shown. Again, the multi-material results exhibit better contact resolution. Although the Lagrangian-remap technique works quite well, completely multi-dimensional schemes, such as WENO5 (Jiang and Shu, 1996), indicate a jet forming along the leading diagonal (reported in Liska and Wendroff (2001)). This can perhaps be discerned in the multi-material results. However, in comparison with a completely dimensionally split scheme (Figure 4.9), the Lagrangian-remap technique is quite symmetrical. The Riemann solver used is based upon Harten (1983) and Ryu and Jones (1995).

4.4.3 Explosion problem

Introduced by Toro (1997), the explosion problem consists of a circular region, radius of 0.4 centred at $(0, 0)$, of high density and pressure ($\rho_i = 1$, $P_i = 1$) surrounded by a region of low density and pressure ($\rho_e = 0.125$, $P_e = 0.1$). Initially at rest with $\gamma = 1.4$, the contact is unstable to the Rayleigh-Taylor instability.

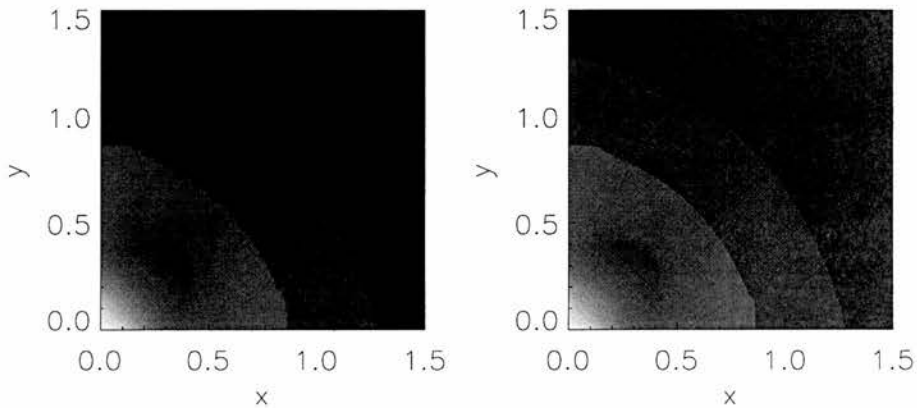


Figure 4.11: Single and multi-material explosion test.

Figure 4.11 shows the single and multi-material simulations of the Explosion problem with $\delta x = \delta y = 0.00375$ at $t = 0.5$. This problem is quite sensitive to perturbations of the interface, and hence the multi-material simulation is more accurate. However, differences between the two simulations is partly due to the initial conditions: the single material run has a castellated contact whereas the multi-material run uses area weighting to initialise density and pressure.

4.5 Multi-material tests

4.5.1 2D air cavity collapse in water

This test was introduced by Hu and Khoo (2004) and is based upon an experiment by Bourne and Field (1992). A 6mm circular air cavity in water is impacted upon by a 1.9GPa shock. Experiments indicate the formation of a high speed jet. The initial condi-

tions (non-dimensionalised against the density of water at 1atm and 1mm) are

pre-shocked water $\rho = 1, u_x = 0, u_y = 0, P = 1, \gamma = 7.15$

post shocked water $\rho = 1.31, u_x = 67.32, u_y = 0, P = 19000, \gamma = 7.15$

air $\rho = 1.2 \times 10^{-3}, u_x = 0, u_y = 0, P = 1, \gamma = 1.4.$

An ideal gas equation of state is used for both materials as in Hu and Khoo (2004), although the Tait equation of state is better suited for water. The air cavity has a radius of 3 and its centre is positioned at $(0, 0)$.

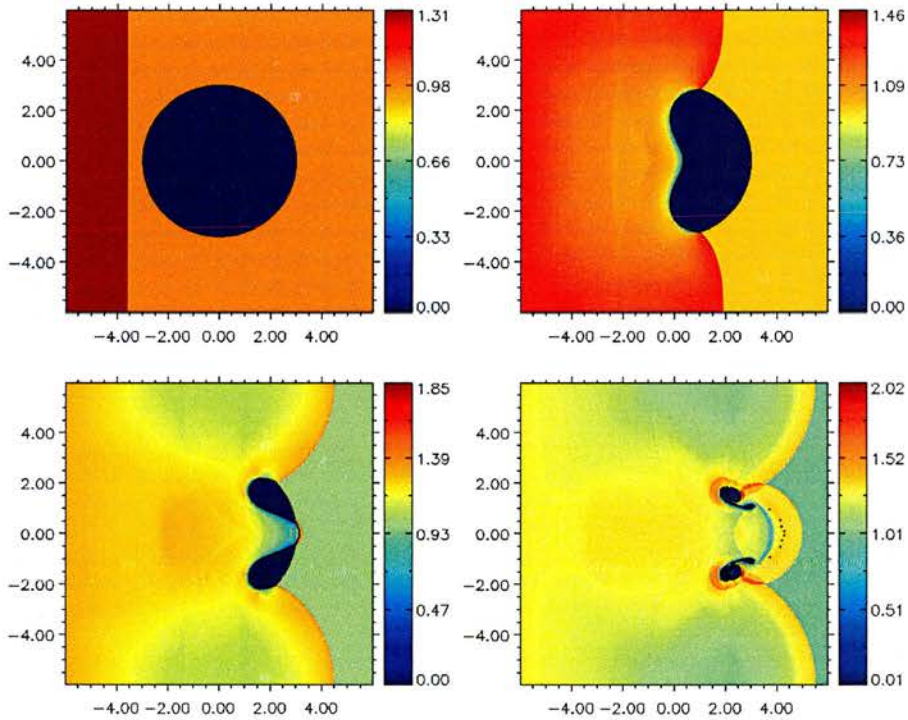


Figure 4.12: Density contours for 2D air cavity collapse.

Figure 4.12 show contours of density at $t = 0, t = 0.02, t = 0.031$ and $t = 0.037$ respectively. At $t = 0.031$, the high speed jet is just about to reach the back wall of the cavity, and at $t = 0.037$ two secondary jets are produced. This is in good agreement with Hu and Khoo (2004).

4.5.2 Air-Helium shock interaction

This test was introduced by Quirk and Karni (1996) based upon experiments by Haas and Sturtevant (1987), and has been discussed in Hu and Khoo (2004). A Mach= 1.22 shock wave in air interacts with a circle filled with Helium. The left and right boundary conditions are transmissive, whilst there are solid walls top and bottom. The initial conditions (non-dimensionalised against the density of air at 1atm and 1mm) are

$$\text{pre-shocked air } \rho = 1, u_x = 0, u_y = 0, P = 1, \gamma = 1.4$$

$$\text{post shocked air } \rho = 1.3764, u_x = 0.394, u_y = 0, P = 1.5698, \gamma = 1.4$$

$$\text{Helium } \rho = 0.138, u_x = 0, u_y = 0, P = 1, \gamma = 1.667.$$

The circle of helium has a radius of 25 and is centred at (0,150). The resolution is $\delta x = \delta y = 0.5$ and the simulation is run until $t = 123.8$. Figure 4.13 agrees well with Hu and Khoo (2004).

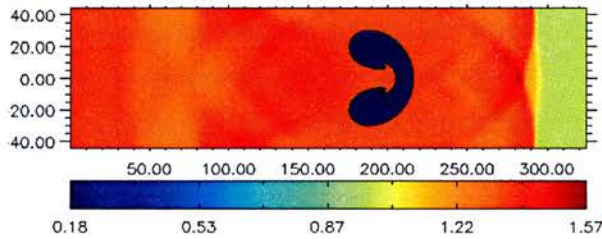


Figure 4.13: Air-Helium interaction at $t = 123.8$.

4.6 Summary

The interface tracking ability of the code, using Youngs algorithm, has been tested on a series of advection tests and one dimensional shock tube problems. Further tests have been performed in two dimensions, including a multi-phase problem. In all cases the code performs quite well in comparison to results published in the literature. Where a single material code could be used, the multi-material code produces similar results. However, at a contact discontinuity or material boundary, the multi-material code produces superior results. Although the code performs better than a completely dimensionally split method, this code fails to preserve the inherent symmetry in some tests.

Chapter 5

Non-linear phase-mixing of an Alfvén wave

5.1 Introduction

Space plasmas support MHD waves (for example those outlined in section 1.3), indeed current theories for stellar/solar wind acceleration and stellar/solar coronal heating make use of MHD wave theory. Recent observations, from such satellite missions as SOHO and TRACE, have successfully detected MHD waves in coronal loops and plumes (De Moor et al., 2002). For a recent review of MHD wave theory, see Roberts (2000).

A current research area is the interaction of MHD waves with plasma inhomogeneities. For a low beta plasma, MHD waves are anisotropic, variations in plasma density outline coronal loops and act as refractive wave guides for fast magnetoacoustic waves (Roberts, 1991). Fast magnetoacoustic waves trapped in such an inhomogeneity are dispersive. Alfvén waves exhibit no dispersion or refraction, and little dissipation. The creation of small length scales enhances dissipation, and for the Alfvén wave this is achieved via resonant absorption (Ionson, 1978) or Phase-mixing (Heyvaerts and Priest, 1983).

An initially plane Alfvén wave propagating along a straight magnetic field with an Alfvén speed inhomogeneity perpendicular to the magnetic field, has its wave front distorted. The speed at which an Alfvén wave propagates is determined by the local magnetic field strength and plasma density. So, Alfvén waves on neighbouring field-lines will propagate at different speeds if the neighbouring field-lines possess differing Alfvén

speeds, thus causing the distortion in the planar wave front. This process shortens the perpendicular wavelength and generates steep transverse gradients. Eventually dissipation mechanisms become important and the initial disturbance is damped.

This process was first proposed as a mechanism for coronal heating by Heyvaerts and Priest (1983), and has been investigated by Browning (1991) and Ireland and Priest (1997); with inhomogeneous steady flows Ryutova and Habbal (1995), Nakariakov et al. (1998); in two dimensional structures Hood et al. (1997), De Moortel et al. (2000).

The inhomogeneity effects the efficiency of non-linear processes (eg. stratification Ofman and Davila (1997)) including fast mode generation. These fast modes are subject to dissipative mechanisms and provide an indirect heating mechanism which is distributed across the magnetic field. Fast mode generation has been studied by Nakariakov et al. (1997), Tsiklauri et al. (2001) and Tsiklauri et al. (2002).

In this chapter some of the effects of varying the plasma β are considered, but mainly the effects of resistivity, and the resulting heating of the plasma, are considered.

5.2 The Equations

In this chapter, a resistive inhomogeneous plasma is considered in Cartesian co-ordinates (x, y, z) , and variations in the y -direction are ignored ($\partial/\partial y \equiv 0$). This follows the analysis of Nakariakov et al. (1997). The equilibrium is an inhomogeneous plasma with density $\rho_0(x)$ embedded in a uniform magnetic field $\mathbf{B}_0 = (0, 0, B_0)$. The equilibrium pressure is uniform P_0 and only a uniform resistivity is used. The perturbed velocity is $\mathbf{u}(x, z, t) = (u_x, u_y, u_z)$, the perturbed magnetic field is $\mathbf{B}(x, z, t) = (B_x, B_y, B_z)$, and the perturbed density and pressure are $\rho(x, z, t)$, $P(x, z, t)$ respectively. From (1.18)-(1.22), perturbations to this system satisfy

$$\rho_0(x) \frac{\partial u_x}{\partial t} + \frac{\partial P}{\partial x} - \frac{B_0}{\mu_0} \left(\frac{\partial B_x}{\partial z} - \frac{\partial B_z}{\partial x} \right) = N_1 \quad (5.1)$$

$$\rho_0(x) \frac{\partial u_y}{\partial t} - \frac{B_0}{\mu_0} \frac{\partial B_y}{\partial z} = N_2 \quad (5.2)$$

$$\rho_0(x) \frac{\partial u_z}{\partial t} + \frac{\partial P}{\partial z} = N_3 \quad (5.3)$$

$$\frac{\partial B_x}{\partial t} - B_0 \frac{\partial u_x}{\partial z} - R_1 = N_4 \quad (5.4)$$

$$\frac{\partial B_y}{\partial t} - B_0 \frac{\partial u_y}{\partial z} - R_2 = N_5 \quad (5.5)$$

$$\frac{\partial B_z}{\partial t} + B_0 \frac{\partial u_x}{\partial x} - R_3 = N_6 \quad (5.6)$$

$$\frac{\partial \rho}{\partial t} + \frac{\partial}{\partial x}(\rho_0 u_x) + \rho_0 \frac{\partial u_z}{\partial z} = N_7 \quad (5.7)$$

$$\frac{\partial P}{\partial t} + \gamma P_0 \left(\frac{\partial u_x}{\partial x} + \frac{\partial u_z}{\partial z} \right) = N_8, \quad (5.8)$$

where the left-hand sides of (5.1)-(5.8) involve only linear terms, and $N_1 - N_8$ involve the non-linear terms. The non-linear terms are

$$\begin{aligned} N_1 = & -\rho \frac{\partial u_x}{\partial t} - \rho_0(x) \left(u_x \frac{\partial u_x}{\partial x} + u_z \frac{\partial u_x}{\partial z} \right) - \frac{1}{\mu_0} B_y \frac{\partial B_y}{\partial x} \\ & + \frac{1}{\mu_0} B_z \left(\frac{\partial B_x}{\partial z} - \frac{\partial B_z}{\partial x} \right) - \rho \left(u_x \frac{\partial u_x}{\partial x} + u_z \frac{\partial u_x}{\partial z} \right) \end{aligned} \quad (5.9)$$

$$\begin{aligned} N_2 = & -\rho \frac{\partial u_y}{\partial t} - \rho_0(x) \left(u_x \frac{\partial u_y}{\partial x} + u_z \frac{\partial u_y}{\partial z} \right) \\ & + \frac{1}{\mu_0} B_z \frac{\partial B_y}{\partial z} + \frac{1}{\mu_0} B_x \frac{\partial B_y}{\partial x} - \rho \left(u_x \frac{\partial u_y}{\partial x} + u_z \frac{\partial u_y}{\partial z} \right) \end{aligned} \quad (5.10)$$

$$\begin{aligned} N_3 = & -\rho \frac{\partial u_z}{\partial t} - \rho_0(x) \left(u_x \frac{\partial u_z}{\partial x} + u_z \frac{\partial u_z}{\partial z} \right) - \frac{1}{\mu_0} B_y \frac{\partial B_y}{\partial z} \\ & - \frac{1}{\mu_0} B_x \left(\frac{\partial B_x}{\partial z} - \frac{\partial B_z}{\partial x} \right) - \rho \left(u_x \frac{\partial u_z}{\partial x} + u_z \frac{\partial u_z}{\partial z} \right) \end{aligned} \quad (5.11)$$

$$N_4 = -\frac{\partial}{\partial z} (u_z B_x - u_x B_z) \quad (5.12)$$

$$N_5 = -\frac{\partial}{\partial z} (u_z B_y - u_y B_z) + \frac{\partial}{\partial x} (u_y B_x - u_x B_y) \quad (5.13)$$

$$N_6 = \frac{\partial}{\partial x} (u_z B_x - u_x B_z) \quad (5.14)$$

$$N_7 = -\frac{\partial}{\partial x} (\rho u_x) - \frac{\partial}{\partial z} (\rho u_z) \quad (5.15)$$

$$N_8 = -\left(u_x \frac{\partial}{\partial x} + u_z \frac{\partial}{\partial z} \right) P - \gamma P \left(\frac{\partial u_x}{\partial x} + \frac{\partial u_z}{\partial z} \right) + R_4. \quad (5.16)$$

The resistive terms are

$$R_1 = \eta \left(\frac{\partial^2}{\partial x^2} + \frac{\partial^2}{\partial z^2} \right) B_x \quad (5.17)$$

$$R_2 = \eta \left(\frac{\partial^2}{\partial x^2} + \frac{\partial^2}{\partial z^2} \right) B_y \quad (5.18)$$

$$R_3 = \eta \left(\frac{\partial^2}{\partial x^2} + \frac{\partial^2}{\partial z^2} \right) B_z \quad (5.19)$$

$$R_4 = (\gamma - 1) \frac{\eta}{\mu_0} \left(\left(\frac{\partial B_y}{\partial z} \right)^2 + \left(\frac{\partial B_x}{\partial z} - \frac{\partial B_z}{\partial x} \right)^2 + \left(\frac{\partial B_y}{\partial x} \right)^2 \right). \quad (5.20)$$

If one were to perform a weakly non-linear analysis ($v = v_0 + \delta v_1 + \delta^2 v_2 + \dots$ for $v = \rho, \mathbf{B}, \mathbf{u}, P$ remembering that $\mathbf{u}_0 = 0$), then the $O(\delta^2)$ equations would simply be (5.1) - (5.8) with the last term of $N_1 - N_3$ absent.

Equations (5.1) - (5.8) can be combined to yield

$$\left(\frac{\partial^2}{\partial t^2} - v_A^2(x) \frac{\partial^2}{\partial z^2} \right) u_y = \frac{1}{\rho_0(x)} \left(\frac{\partial N_2}{\partial t} + \frac{B_0}{\mu_0} \left(\frac{\partial N_5}{\partial z} + \frac{\partial R_2}{\partial z} \right) \right) \quad (5.21)$$

$$\left(\frac{\partial^2}{\partial t^2} - c_s^2(x) \frac{\partial^2}{\partial z^2} \right) u_z - c_s^2(x) \frac{\partial^2 u_x}{\partial x \partial z} = \frac{1}{\rho_0(x)} \left(\frac{\partial N_3}{\partial t} - \frac{\partial N_8}{\partial z} \right) \quad (5.22)$$

$$\left(\frac{\partial^2}{\partial t^2} - (c_s^2(x) + v_A^2(x)) \frac{\partial^2}{\partial x^2} - v_A^2(x) \frac{\partial^2}{\partial z^2} \right) u_x - c_s^2(x) \frac{\partial^2}{\partial x \partial z} u_z = \frac{1}{\rho_0(x)} \left(\frac{\partial N_1}{\partial t} - \frac{\partial N_8}{\partial x} + \frac{B_0}{\mu_0} \left(\frac{\partial N_4}{\partial z} - \frac{\partial N_6}{\partial x} + \frac{\partial R_1}{\partial z} - \frac{\partial R_3}{\partial x} \right) \right), \quad (5.23)$$

where $c_s^2(x) = \gamma P_0 / \rho_0(x)$ is the unperturbed sound speed and $v_A^2(x) = B_0^2 / \mu_0 \rho_0(x)$ is the unperturbed Alfvén speed. The equations governing the Alfvén and magnetoacoustic wave modes (5.21)-(5.23) reduce to the equations in Botha et al. (2000) when $R_1 - R_4$ are identically zero.

5.3 The model

Following Botha et al. (2000) and Tsiklauri et al. (2001), the density profile is

$$\rho_0(x) = 3 \pm 2 \tanh(\lambda x),$$

where λ is a free parameter controlling the width over which the density profile varies. The influence of λ on fast mode generation is discussed in Botha et al. (2000). Figure 5.1 shows the density profile and associated Alfvén velocity used during the simulations.

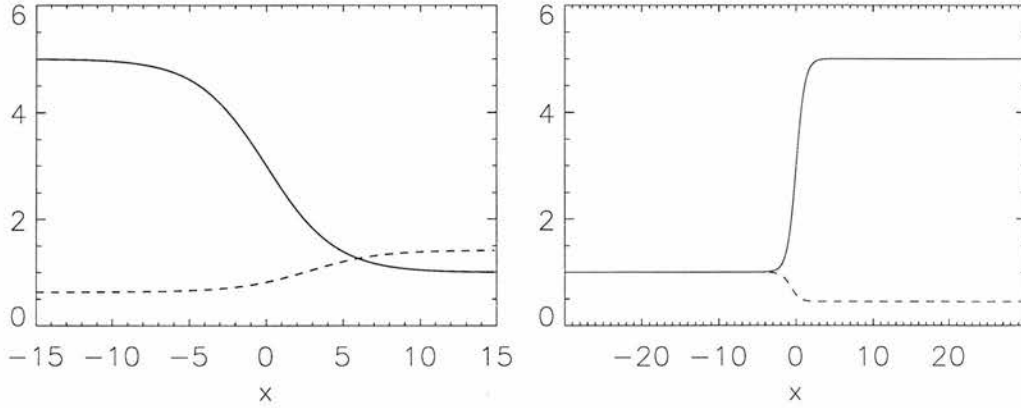


Figure 5.1: Density (solid line) and Alfvén velocity (dashed line) profiles for the periodic and driven set ups respectively.

Two perturbations to the system, which induce linearly polarised Alfvén waves, are considered. Firstly, periodic boundary conditions are imposed in the z -direction, and an Alfvén wave is initialised so that two wavelengths fill the domain. The Alfvén wave is given by

$$\begin{aligned} u_y &= A \sin(kz) \\ B_y &= -A\sqrt{\rho_0\mu_0} \sin(kz), \end{aligned}$$

at $t = 0$ and is planar. The amplitude is 10^{-3} , and $\lambda = \sqrt{0.05}$. It is with this set up that the effects of the plasma β are investigated. This is referred to as the periodic system.

Secondly, a sinusoidal Alfvén wave is driven at the $z = 0$ boundary

$$u_y(x, z, t) = A \sin(\omega t), \quad u_x(x, z, t) = u_z(x, z, t) = 0, \quad (5.24)$$

with $A = 10^{-3}$, $\omega = 1$ and $\lambda = \sqrt{0.75}$. The simulation is halted before the wave reaches the upper boundary. This is referred to as the driven system. It should be noted that (5.24) does not drive a pure Alfvén wave into the numerical domain, acoustic modes are excited as well. Consider the 1.5D problem of driving an Alfvén wave via (5.24). The equation governing the slow mode is

$$\frac{\partial^2 u_z}{\partial t^2} - c_s^2 \frac{\partial^2 u_z}{\partial z^2} = -\frac{1}{\mu_0} B_y \frac{\partial B_y}{\partial z},$$

and the solution is

$$u_z = F(z - c_s t) + G(z - v_A t).$$

This comprises the non-linear effects of the Alfvén wave and the slow mode driven at the boundary (see Figure 5.2).

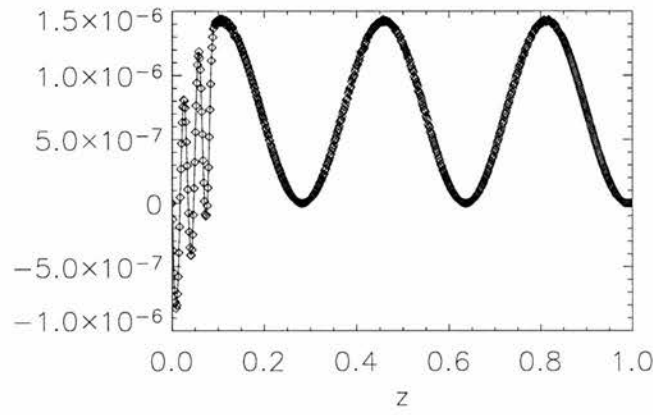


Figure 5.2: Plot of u_z showing the pondermotive effect and acoustic mode.

The slow mode can be irradiated with more carefully chosen boundary conditions. However, it is unlikely that photospheric disturbances will generate pure Alfvén waves, and with $\beta \ll 1$, the acoustic mode does not obscure the phase-mixing result.

5.4 The $\beta = 0, \eta = 0$ case

Consider the simplified case of a cold ($\beta = 0$), non-resistive ($\eta = 0$) plasma. Equations (5.21) - (5.23) reduce to

$$\left(\frac{\partial^2}{\partial t^2} - v_A^2(x) \frac{\partial^2}{\partial z^2} \right) u_y = \frac{1}{\rho_0(x)} \left(\frac{\partial N_2}{\partial t} + \frac{B_0}{\mu_0} \frac{\partial N_5}{\partial z} \right) \quad (5.25)$$

$$\frac{\partial^2 u_z}{\partial t^2} = \frac{1}{\rho_0(x)} \frac{\partial N_3}{\partial t} \quad (5.26)$$

$$\left(\frac{\partial^2}{\partial t^2} - v_A^2(x) \left(\frac{\partial^2}{\partial x^2} + \frac{\partial^2}{\partial z^2} \right) \right) u_x = \frac{1}{\rho_0(x)} \left(\frac{\partial N_1}{\partial t} + \frac{B_0}{\mu_0} \left(\frac{\partial N_4}{\partial z} - \frac{\partial N_6}{\partial x} \right) \right). \quad (5.27)$$

Equations (5.25) - (5.27) are those laid out in Nakariakov and Oraevsky (1995), Nakariakov et al. (1997).

A linear Alfvén wave perturbs u_y and B_y , whereas magnetoacoustic waves perturb the other variables. However, the non-linear effects of an Alfvén wave perturb these variables as well. Initially there are no magnetoacoustic waves present, only the Alfvén wave is perturbed. In the linear limit ($N_2, N_5 = 0$) equation (5.25) is satisfied by $u_y = f(z - v_A(x)t)$, where f is determined by the initial or boundary conditions. So, for example, with an harmonic oscillator ($u_y = A \sin(\omega t)$) at the lower boundary ($z = 0$) driving a travelling Alfvén wave into the domain the solution is

$$u_y = A \sin(\omega(t - z/v_A(x)))$$

$$B_y = -A\sqrt{\mu_0\rho_0(x)} \sin(\omega(t - z/v_A(x))),$$

where A is the wave amplitude, which is assumed sufficiently small for the wave to submit to weakly non-linear theory, and ω is the wave frequency, (see Figure 5.3).

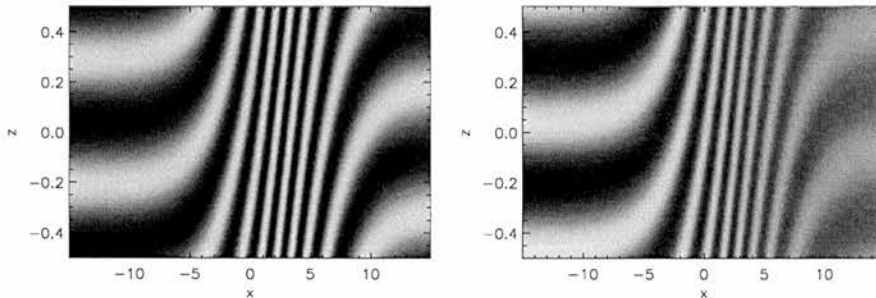


Figure 5.3: Contours of u_y and b_y respectively, showing the phase-mixed Alfvén wave at $t = 5$ for the periodic case.

In the cold plasma limit the fast and slow magnetoacoustic modes decouple. So equation (5.27) describes the fast mode, equation (5.26) describes the degenerate slow mode. Whilst N_2, N_5 have been neglected, B_y is non-zero, and so N_1 and N_3 are non-zero. In the early stages, the fast mode generation is governed by

$$\left(\frac{\partial^2}{\partial t^2} - v_A^2(x)\left(\frac{\partial^2}{\partial x^2} + \frac{\partial^2}{\partial z^2}\right)\right)u_x = \frac{-1}{\mu_0\rho_0(x)}\frac{\partial}{\partial t}\left(B_y\frac{B_y}{\partial x}\right),$$

see Nakariakov et al. (1997). Taking the driven Alfvén wave example, the right-hand-side

of the above equation equals

$$\frac{\partial}{\partial t} \left(\frac{\partial}{\partial x} \left(\frac{B_y^2}{2} \right) \right) = \frac{-A^2 \omega}{2\rho_0(x)v_A^2(x)} \left(\rho_0' \sin(2\omega(t - z/v_A(x))) v_A^2(x) + 2\rho_0(x)\omega z v_A' \cos(2\omega(t - z/v_A(x))) \right).$$

The fast mode generation is forced non-linearly by temporal and spatial variations in the wave pressure ($B_y^2/2$). The fast wave frequency (2ω) is twice that of the driving Alfvén wave. The fast mode, in these initial stages, grows secularly with time (Botha et al., 2000). The fast mode generation relies upon the plasma inhomogeneity.

Longitudinal plasma motions are also excited non-linearly by equation (5.26), which for the harmonic driver described above is

$$u_z = -\frac{A^2 \mu_0 \rho_0(x) \omega^2}{v_A(x)} \cos(2\omega(t - z/v_A(x))).$$

Again the frequency is twice the driving frequency. Longitudinal motions do not grow with time, and are independent of the plasma inhomogeneity.

Both the fast mode and the slow mode linearly affect the plasma density, equation (5.7).

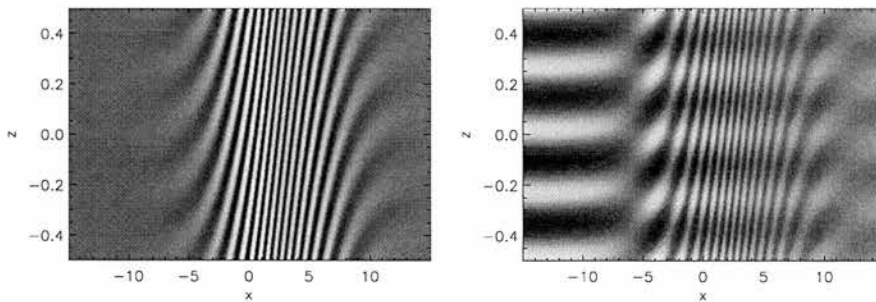


Figure 5.4: Perpendicular and parallel components of velocity respectively, for the periodic case at $t = 5$.

Although the fast mode generated by Alfvén wave phase-mixing initially grows secularly with time, this process is seen to saturate in numerical simulations. Numerical studies have been undertaken with a wave train (Botha et al., 2000) and individual pulses (Tsiklauri et al. (2001), Tsiklauri et al. (2002)). The saturation level is dependent upon

the amplitude and wavelength of the Alfvén wave and the length scale of the plasma inhomogeneity.

5.5 The $\beta \neq 0, \eta = 0$ case

In this section a brief look at the effects of varying the plasma β is made. The periodic equilibrium is used. In Figure 5.5 a comparison is made of u_x and u_z at $t = 1$. The height at which the velocity component is considered depends upon the magnetoacoustic velocities, so to enable a fair comparison each case of β is plotted at the same stage of development. For u_x there is little difference between $\beta = 0$, $\beta = 0.01$ and $\beta = 0.1$. The case $\beta = 1$ is significantly different throughout all of the comparisons. Small differences in amplitude can be seen in the comparison of u_z for the cases $\beta = 0$, $\beta = 0.01$ and $\beta = 0.1$.

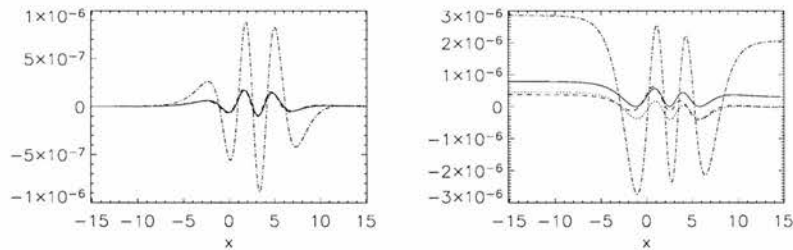


Figure 5.5: Comparison of slices across the x -direction of the perpendicular and parallel velocity components respectively, for $\beta = 0$ (solid line), $\beta = 0.01$ (dotted line), $\beta = 0.1$ (dashed line) and $\beta = 1$ (dot-dashed line) at $t = 1$.

In Figure 5.6 a similar comparison is made for cuts in the z -direction. Again, to enable a fair comparison the value of z at which the cut is made is dependent upon the fast magnetoacoustic speed. Ignoring the $\beta = 1$ case, varying β has had little effect on u_x , whilst $\beta = 0$ differs in amplitude and phase to $\beta = 0.1, 0.01$ in u_z .

In Figure 5.7, contours of u_z at $t = 5$ are displayed. There is no discernable difference between the cases $\beta = 0$ and $\beta = 0.01$. By this time the structure of u_y for the case $\beta = 0.1$ is quite different from the lower values of β , and bands starting at $x = -2, 0, 1, 5$ can be seen in the case $\beta = 1$.

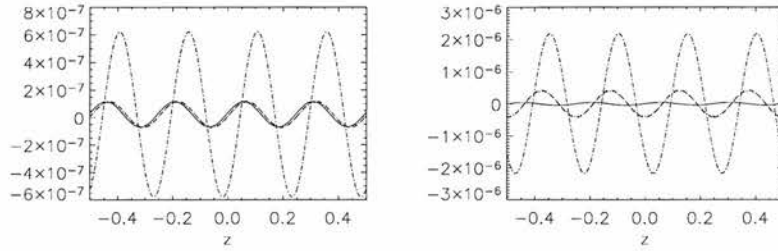


Figure 5.6: Comparison of slices across the z -direction of the perpendicular and parallel velocity components respectively, for $\beta = 0$ (solid line), $\beta = 0.01$ (dotted line), $\beta = 0.1$ (dashed line) and $\beta = 1$ (dot-dashed line) at $t = 1$.

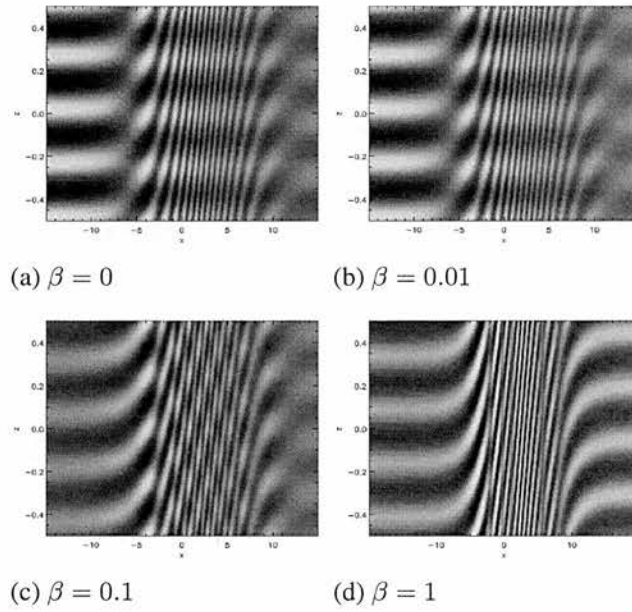


Figure 5.7: Contours of the parallel velocity component for differing values of β at $t = 5$.

Similarly to Figure 5.5, Figure 5.8 shows cuts across x for u_x and u_z , but at the later time of $t = 5$. At this time there is still very little difference between $\beta = 0$, $\beta = 0.01$ and $\beta = 0.1$ for u_x . For u_z , as indicated by Figure 5.7, there is no difference between $\beta = 0$ and $\beta = 0.01$, whilst the structure for the case $\beta = 0.1$ is significantly different.

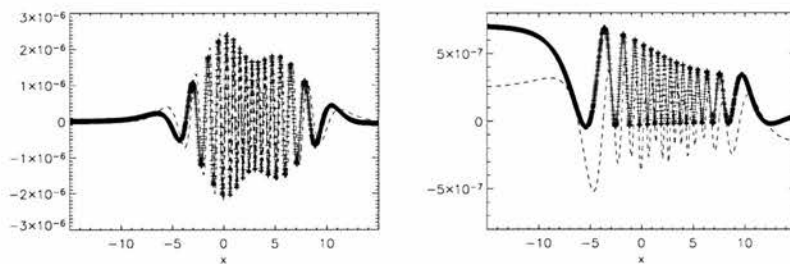


Figure 5.8: Comparison of slices across the x -direction of the perpendicular and parallel velocity components respectively, for $\beta = 0$ (solid line), $\beta = 0.01$ (crosses) and $\beta = 0.1$ (dashed line) at $t = 5$.

5.6 The resistive effects

A linear solution to the Alfvén wave perturbation is sought, equation (5.21) reduces to

$$\left(\frac{\partial^2}{\partial t^2} - v_A^2(x) \frac{\partial^2}{\partial z^2} \right) u_y = \frac{B_0}{\mu_0 \rho_0(x)} \frac{\partial R_2}{\partial z} = \eta \left(\frac{\partial^2}{\partial x^2} + \frac{\partial^2}{\partial z^2} \right) \frac{\partial u_y}{\partial t}. \quad (5.28)$$

The solution is taken to be of the form

$$\exp(i\omega(t - z/v_A(x)) + \eta F(x, z)),$$

for some arbitrary function F . Equation (5.28) becomes

$$2i\omega\eta F_z v_A - \eta F_{zz} v_A^2 = -\omega\eta z \frac{(v_A')^2}{v_A^3} - i\omega^3 \eta z^2 \frac{(v_A')^2}{v_A^4} - i\omega^3 \eta \frac{1}{v_A^2} + O(\eta^2),$$

where subscript z denotes differentiation with respect to z , and prime denotes differentiation with respect to x . Let $F = \alpha z^3 + \beta z^2 + \gamma z$, equating coefficients yields

$$\alpha = \frac{-\omega^2 (v_A')^2}{6v_A^5}, \quad \beta = \frac{i\omega}{4v_A^2} \left(\frac{(v_A')^2}{v_A} \right)', \quad \gamma = \frac{-\omega^2}{2v_A^3} + \frac{1}{4v_A^2} \left(\frac{(v_A)'}{v_A} \right)'$$

and

$$u_y = \exp\left(\frac{-\eta\omega^2}{2v_A^3} z - \frac{\eta\omega^2 (v_A')^2}{6v_A^5} z^3 + \frac{\eta}{4v_A^2} \left(\frac{v_A'}{v_A} \right)' z \right) \sin\left(\omega \left(t - \frac{z}{v_A} \right) + \frac{\omega}{4v_A^2} \left(\frac{v_A'}{v_A} \right)' z^2 \right).$$

Simulations are carried out using the driven condition, equation (5.24). The effects

of uniform resistivity on the development, and any possible heating, is investigated. The simulation is halted at $t = 48$, just before the Alfvén wave reaches the top of the numerical domain. Firstly, for comparison, the simulation is run with $\eta = 0$. Figure 5.9 shows plots of the velocity components. The Alfvén wave (u_y) propagates at the local Alfvén speed, and a large shear develops. The pondermotive effect can be seen in Figure 5.9(b), with the slow mode penetrating to $z = 4$ on the left hand boundary. In Figure 5.9(c), two interacting parts can be seen. The generated fast mode (following the same profile as the pondermotive effect on u_z) is interacting with a diagonally propagating wave. The interaction pattern is in the region $0 < x < 12, 2 < z < 20$. It is likely that the diagonally propagating part is a result of the driven boundary conditions.

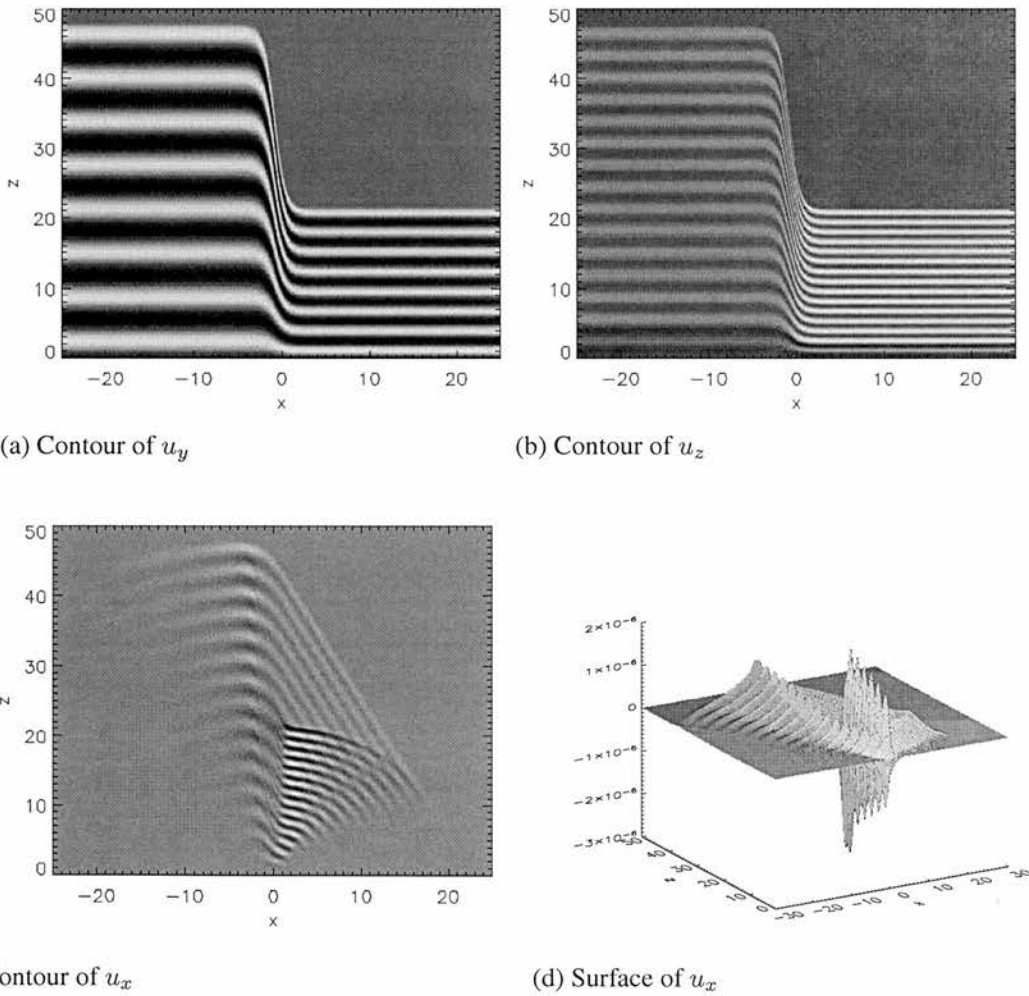
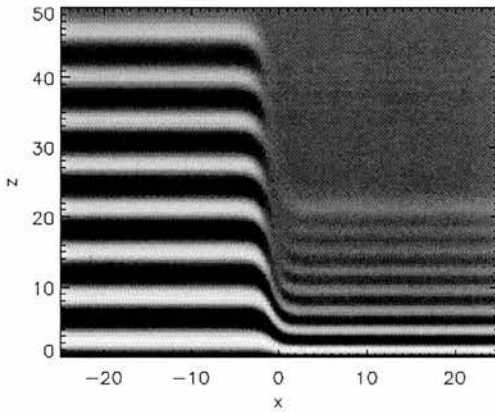
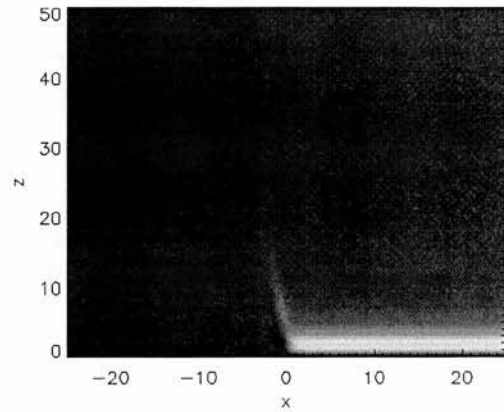


Figure 5.9: Images of all of the velocity components for the $\eta = 0$ case, at $t = 48$.

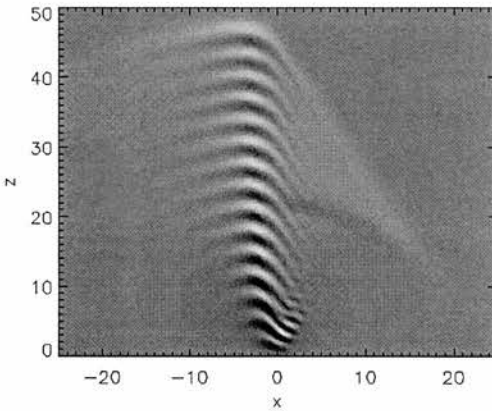
The simulation is repeated with uniform resistivity included. In Figure 5.10(a) the Alfvén wave amplitude is damped across its entire front, but at the inflection point of $v_A(x)$ the damping is most pronounced, as expected from phase-mixing theory (Heyvaerts and Priest, 1983). The pondermotive effect (Figure 5.10(b)) is obscured by a bulk flow up the background field. For $x > 0$, the fast mode has been significantly damped.



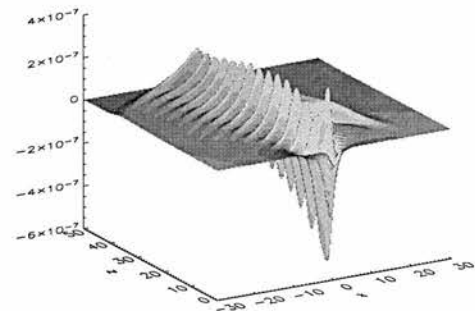
(a) Contour of u_y



(b) Contour of u_z



(c) Contour of u_x



(d) Surface of u_x

Figure 5.10: Images of all of the velocity components for the $\eta \neq 0$ case, at $t = 48$.

In Figure 5.11, the perturbed density is plotted along the field at $x = -10$, $x = 0$ and $x = 10$ respectively. At $x = -10$ the slow mode and pondermotive effects can be seen. From a height of $z \approx 5$ the density is enhanced for the $\eta \neq 0$ case. The density enhancement is far more pronounced at $x = 0$, whilst the largest density enhancement is achieved at $x = 10$.

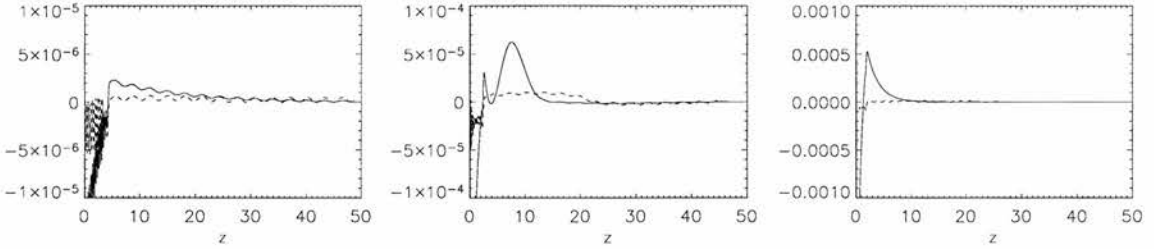


Figure 5.11: Comparison of the density perturbation for the $\eta = 0$ (dashed line) and $\eta \neq 0$ (solid line), at 3 locations in x .

In Figure 5.12 the perturbed value of P/ρ at the same locations as in Figure 5.11. For the case where $\eta = 0$, the effects of the slow mode and the pondermotive force are clearly visible. For the case where $\eta \neq 0$, increases in P/ρ exist. These are largest at $x = 0$ where the phase-mixing occurs, and in the right half-plane.

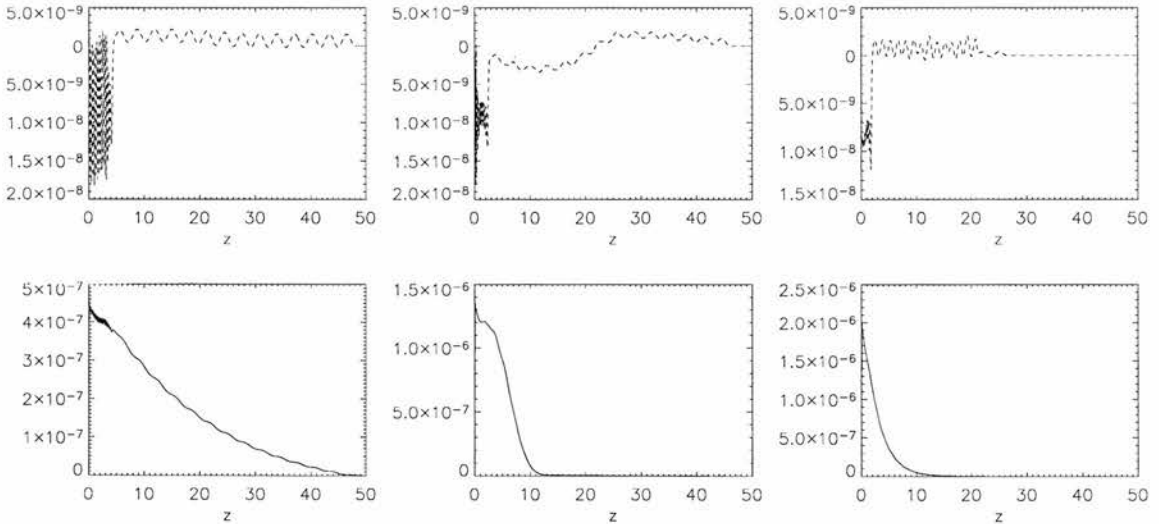


Figure 5.12: Comparison of the temperature perturbation for 3 locations in x , where the upper panel considers the case $\eta = 0$ whilst the lower panel considers the case $\eta \neq 0$.

There are signs of increased density and P/ρ enhancement at the location of phase-mixing. However, equally large enhancements are found in the right half-plane. It is in this region where the fast mode is damped, and where the large bulk motion exists presumably to support the density enhancement.

5.7 Conclusions

The dissipation of Alfvén waves due to phase-mixing is considered. In addition, a uniform resistivity is applied and the effects of ohmic heating are investigated.

The boundary driven perturbations force not only an Alfvén wave, but a slow mode and a fast mode into the numerical domain. Due to the small size of β being considered, the slow mode does not propagate far into the numerical domain, and consequently has little effect on the solution. The boundary driven fast mode interacts with the fast mode generated by phase-mixing.

The inclusion of resistivity sets up an additional flow, this is not due to phase-mixing but simply the effect ohmic heating has on the boundary driven perturbations. For the set of parameters considered, the change in density due to this flow is larger than the change in density due to phase-mixing.

Chapter 6

Ongoing research: Coronal heating by nanoflares triggered by an ideal kink instability in a loop

6.1 Introduction

One of the outstanding problems in Solar physics is to explain how the Corona is heated to millions of degrees. Although it is acknowledged that the heating mechanism relies upon the coronal magnetic field, many different theories for the precise heating mechanism have been proposed. These fall into two broad categories: wave dissipation mechanisms, such as phase-mixing and resonant absorption, and magnetic reconnection.

The “nanoflare” scenario (Parker, 1988) suggests that coronal heating is due to the superposition of many small, and as yet unobservable, flare-like energy releasing events. This energy release mechanism, the same as for large flares, is magnetic reconnection (Priest and Forbes, 2002). This mechanism converts energy stored in the coronal magnetic field into thermal and kinetic energy on timescales much shorter than the ohmic diffusion timescale for the large scale Corona. The “nanoflare” model proposes that the heating of the Corona is sporadic rather than continuous, this is compatible with current satellite observations which indicate that transient energy releasing events are widespread in the solar atmosphere. Whether nanoflares occur frequently enough for them to heat the Corona is an open question. It is of interest to be capable of predicting how frequently

energy releasing events of varying sizes occur.

It is difficult to directly calculate the energy release due to magnetic reconnection in several localised sites, as may be found in complicated coronal fields. Instead magnetic relaxation theory is used. This process originally reported by Taylor (1974) has often been used in the Solar coronal context: Heyvaerts and Priest (1984), Browning and Priest (1986), Browning et al. (1986), Browning (1988), Vekstein et al. (1993), Lothian and Browning (2000), Zhang and Low (2003), Melrose (2004), Priest et al. (2005). For an ideal plasma the magnetic helicity, which is gauge invariant, is defined as

$$K = \int_V \mathbf{A} \cdot \mathbf{B} dV, \quad (6.1)$$

where \mathbf{A} is such that $\mathbf{B} = \nabla \wedge \mathbf{A}$. Relaxation theory states that, in the presence of small scale magnetic reconnection, global magnetic helicity is maintained, whereas magnetic energy is dissipated by the reconnection process. Helicity dissipation is expected to be much smaller than energy dissipation (Berger (1984), Taylor (1986)). A simple justification for this is presented in Browning (1988); the respective resistive dissipation rates for magnetic helicity and magnetic energy are

$$\frac{dK}{dt} = -2 \int_V \eta(\mathbf{j} \cdot \mathbf{B}) dV, \quad \frac{dW}{dt} = - \int_V \eta(\mathbf{j} \cdot \mathbf{j}) dV, \quad (6.2)$$

where W is the magnetic energy. Assuming that the dissipation occurs predominantly in thin current layers of width l , where $l \ll L$ and L is the global length scale, then $\mathbf{j} \propto B/(\mu_0 l)$ and

$$\frac{dK}{dt} = -\frac{2\eta B^2 L^3}{\mu_0 l}, \quad \frac{dW}{dt} = -\frac{\eta B^2 L^3}{\mu_0^2 l^2}, \quad (6.3)$$

so that

$$\frac{l}{K} \frac{dK}{dt} \bigg/ \frac{L}{W} \frac{dW}{dt} \ll 1. \quad (6.4)$$

So, the dissipation of helicity in thin current layers is much slower than the dissipation of magnetic energy. It should be noted that any injection of helicity and energy via driving motions has been ignored. Although helicity injection via photospheric footpoint motions can be important (Heyvaerts and Priest (1984), Berger (1984)), the model considered here starts with an unstable loop. Helicity and energy are injected during the slow evolution

which establishes the initial unstable equilibrium (Browning and Van der Linden, 2003). A more detailed discussion of helicity during magnetic reconnection processes is presented in Ji (1999).

Once a magnetic field is disrupted, it tends to relax towards the minimum magnetic energy state, subject to helicity conservation. This relaxed state is the linear force-free field,

$$\nabla \wedge \mathbf{B} = \alpha \mathbf{B}, \quad (6.5)$$

where α is a constant. Observation of such a relaxation process has been reported in Nandy et al. (2003). Since the relaxed state is assumed to be static, the energy difference between the initial and relaxed states is assumed to be dissipated as heat. During the relaxation process some magnetic energy may be converted into kinetic energy, but this is assumed to be subsequently dissipated by viscosity, or some other process, to achieve the static relaxed state.

Consider the situation where the coronal magnetic field is stressed by photospheric footpoint motions, where the timescale of the footpoint motions is small in comparison to the Alfvén travel time along the coronal field lines. The magnetic field evolves into a non-linear force-free field. If this field is disrupted, it may relax to the lower energy linear force-free field, releasing the energy as heat (Heyvaerts and Priest, 1984). One answer to the question of how long does the magnetic energy build up as the field is stressed by footpoint motions before a heating event occurs, is proposed by Browning and Van der Linden (2003). They suggest that a heating event is triggered by the onset of an ideal MHD instability. Numerical simulations of cylindrical loop models indicate that the kink instability, in its non-linear phase, generates strong current sheets where magnetic reconnection can dissipate energy rapidly via resistive effects (see for example Baty and Heyvaerts (1996), Velli et al. (1997), Arber and Van der Linden (1999), Baty (2000)).

The coronal heating process proposed by Browning and Van der Linden (2003), and the model considered in this chapter is as follows. The coronal magnetic field is stressed by photospheric footpoint motions, evolving quasi-statically through a sequence of equilibria until the field becomes linearly unstable. At this stage a heating event occurs, by the end of which the magnetic field has relaxed to a linear force-free field with the same helicity but less magnetic energy. The heat released during the event can be calculated as

the difference between the magnetic energies of the stressed and relaxed state. The value of α for the relaxed magnetic field is determined by helicity conservation. This process is investigated using a simple model which consists of a cylindrical coronal loop, with the photosphere represented by the boundaries at the top and bottom of the loop. The initial non-linear force-free equilibrium is given by a two layer model with a piecewise constant α profile. So

$$\nabla \wedge \mathbf{B} = \alpha(r)\mathbf{B}, \quad (6.6)$$

where $\alpha = \alpha_1$ for $r \leq R_c$ and $\alpha = \alpha_2$ for $r > R_c$. The magnetic field components are continuous across the boundary $r = R_c$ whilst the current is discontinuous at this point. The linear stability threshold for the ideal kink instability is calculated using the CILTS code. This code is similar to MALTS described in Van der Linden and Hood (1998).

The purpose of this work is to compare the non-linear dynamical evolution of the kink instability and following relaxation provided by three dimensional numerical simulations, with the predictions of linear stability theory and relaxation theory as appropriate.

6.2 The model

The length and width of the numerical domain is taken to be 3, whilst the height is 20. Since the radius of the loop is 1 for each equilibrium, each loop has an aspect ratio of 20. The length and width of the box were chosen so that the boundary conditions will not affect the evolution of the loop. Line-tied boundary conditions are imposed at the top and bottom of the domain. Each simulation has a resolution of 81^3 , simulations with a greater resolution will be undertaken in the near future. The non-uniform resistivity used is given by equation (2.9), and is limited so that it cannot exceed 10^{-3} . The relative helicity is calculated from equation (6.2), with the initial value given by an analytical calculation from the equilibrium (6.7)-(6.11).

The equilibria are defined as in Browning and Van der Linden (2003), and are given by

$$B_z = B_1 J_0(\alpha_1 r), \quad B_\theta = B_1 J_1(\alpha_1 r), \quad (r \leq R_c), \quad (6.7)$$

$$\begin{aligned} B_z &= B_2 J_0(\alpha_2 r) + C_2 Y_0(\alpha_2 r), \\ B_\theta &= B_2 J_1(\alpha_2 r) + C_2 Y_1(\alpha_2 r), \end{aligned} \quad (R_c < r < 1.0), \quad (6.8)$$

where,

$$C_2 = B_1 \frac{J_0(\alpha_1 R_c) J_1(\alpha_2 R_c) - J_1(\alpha_1 R_c) J_0(\alpha_2 R_c)}{\Delta}, \quad (6.9)$$

$$B_2 = B_1 \frac{J_1(\alpha_1 R_c) Y_0(\alpha_2 R_c) - J_0(\alpha_1 R_c) Y_1(\alpha_2 R_c)}{\Delta}, \quad (6.10)$$

and,

$$\Delta = \frac{2}{\pi \alpha_2 R_c}, \quad (6.11)$$

where $R_c = 0.5$ and $B_1 = 1$. The remainder of the numerical domain is filled with a potential field which matches the equilibrium field at $r = 1$. For case 1: $\alpha_1 = 2.3$, $\alpha_2 = 0.01$, and for case 2: $\alpha_1 = 4.9$ and $\alpha_2 = 0.01$. Figure 6.1 shows the initial B_z (solid line) and B_θ (dashed line) as a function of loop radius, for case 1 and case 2 respectively.

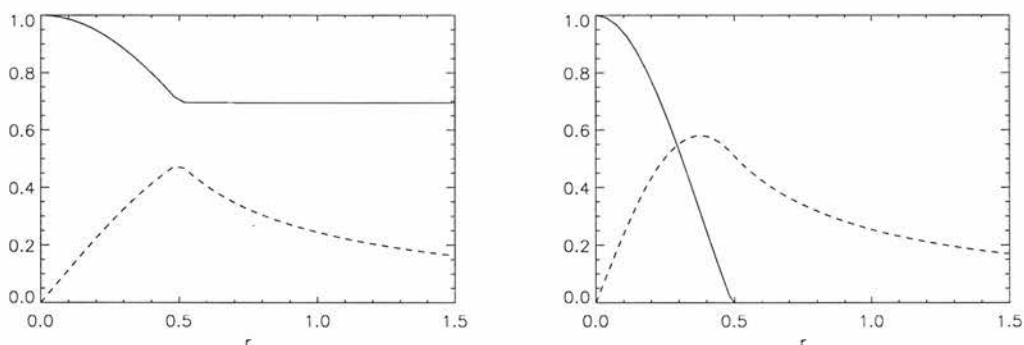


Figure 6.1: Plots of B_z (solid) and B_θ (dashed) for case 1 and case2 respectively.

These equilibria are initially unstable, and small a velocity perturbation is applied to trigger the kink instability. The evolution of the instability, and the subsequent relaxation are investigated.

6.3 Preliminary results

6.3.1 Case 1

By $t = 100\tau_A$ the loop shows signs of instability (see Figure 6.2). The growth rate of the instability is estimated from the kinetic energy ($\nabla(\log(KE))$), and is approximately 0.05 which is in agreement with the linear results. A current concentration starts to form at $r \approx 0.75$ at $t = 110\tau_A$, a helical current sheet can be seen wrapped around the loop at $t = 120\tau_A$ in Figure 6.2.

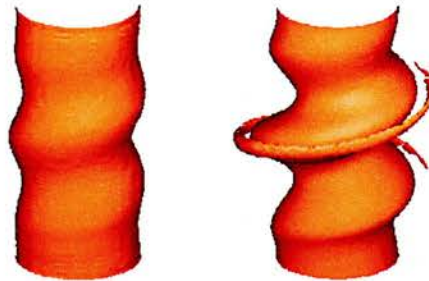


Figure 6.2: Isosurfaces of current at $|j| = 1.5$ at $t = 100\tau_A$ (left hand side) and $t = 120\tau_A$ (right hand side) for case 1.

The resistive effects start at $t \approx 130\tau_A$ when the current exceeds the pre-determined value of j_{crit} . Figure 6.3 shows that the ohmic heating increases from this time. At $t \approx 200\tau_A$ the magnetic energy starts to fall quickly, whilst the kinetic energy increases rapidly, before decreasing more slowly.

The simulation is continued until $t = 400\tau_A$, by which time the magnetic energy is starting to level out, and the current has dropped below j_{crit} and the resistive effects are switched off. The helicity varies in a similar fashion to the ohmic heating, the variation in helicity is small in comparison to its initial value. The relative change in helicity ($\delta K/K \approx 0.003$) is much smaller than the relative change in magnetic energy ($\delta W/W \approx 0.01$). This is consistent with relaxation theory. From equation (6.4), the change in helicity relative to the change in energy should scale like l/L which cannot be smaller than $1/81$ in these simulations, whereas much smaller values would be expected

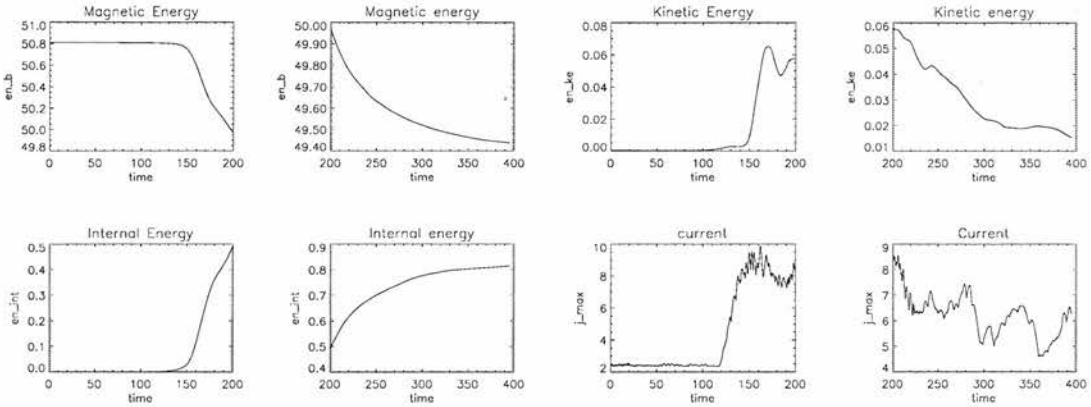


Figure 6.3: Plots of magnetic energy (top, left hand side), kinetic energy (top, right hand side) internal energy (bottom, left hand side) and current (bottom, right hand side) for case 1.

in the corona.

The cumulative ohmic heating (Figure 6.4) is constant from $t \approx 300\tau_A$, suggesting that

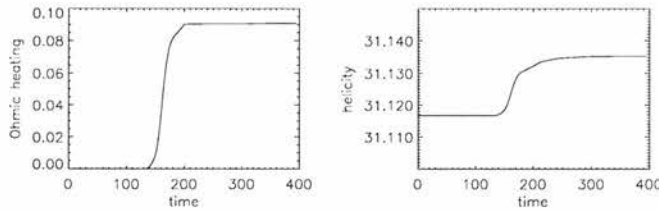


Figure 6.4: Plots of cumulative ohmic heating (left),and helicity (right) for case 1.

the value of resistivity is too small for much magnetic reconnection to occur. Current and kinetic energy are still decaying at this time, suggesting that the relaxation process has not yet been completed. More resolution is necessary to follow the evolution further.

6.3.2 Case 2

This equilibrium is far more unstable than case 1, with the loop showing signs of being kinked by $t \approx 10\tau_A$, (see Figure 6.5) and a growth rate of 0.15.

The isosurface of current (Figure 6.5) shows a very different structure to that of case 1. Indeed this equilibrium is quite different in its behaviour compared with other invest-

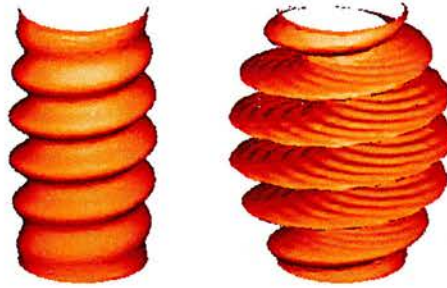


Figure 6.5: Isosurfaces of the loop at $|j| = 1.5$ at $t = 10\tau_A$ (left hand side) and $t = 20\tau_A$ (right hand side) for case 2.

igated equilibria. Nonetheless, a current concentration forms and the resistive effects are triggered at $t \approx 20\tau_A$. The magnetic energy falls and the kinetic energy peaks and then falls as in case 1 (see Figure 6.6).

The cumulative ohmic heating increases between $t \approx 20\tau_A$ and $t \approx 30\tau_A$, levels off between $t \approx 35\tau_A$ and $t \approx 55\tau_A$ (see Figure 6.7). Just before the simulation is halted at $t = 60\tau_A$, the ohmic heating starts to increase again. Conversely, the helicity falls, is almost constant and then starts to fall again just before $t = 60\tau_A$.

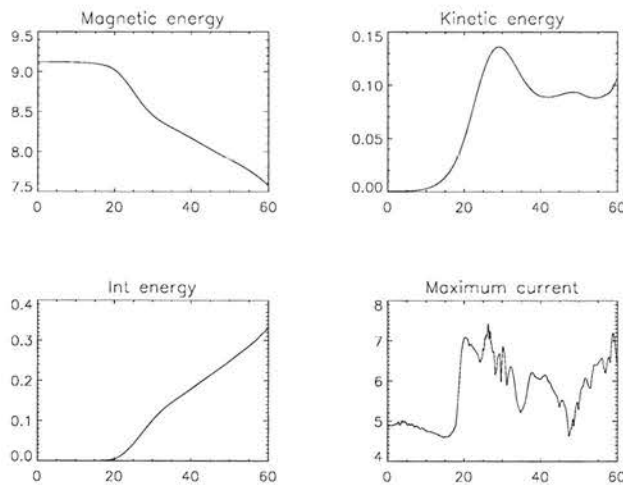


Figure 6.6: Plots of magnetic energy (top, left hand side), kinetic energy (top, right hand side), internal energy (bottom, left hand side) and current (bottom, right hand side) for case 2.

This equilibrium is included for interest, as it is quite different from the other equilib-

ria considered. More resolution is needed to see how long the trend of increasing ohmic heating extends beyond $t = 60\tau_A$.

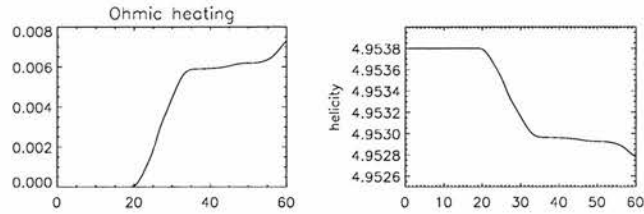


Figure 6.7: Plots of cumulative ohmic heating (left hand side), and helicity (right hand side) for case 2.

Chapter 7

Summary

In this thesis a two dimensional multi-material code for non-linear resistive MHD has been developed. The code uses the Lagrangian-remap technique, whereby the numerical grid evolves with the plasma during the Lagrangian step, and then the primary variables are remapped back onto the original Eulerian grid. The grid is staggered to prevent checkerboard instabilities. Gradient limiters are employed in the remap step to help preserve monotonicity. The code uses artificial viscosity to control shocks, and a constrained transport technique to maintain $\nabla \cdot \mathbf{B} = 0$. The code is written in MPI-f90 to enable it to be run on parallel architectures.

The most important development is the interface tracking capability of this code. The motivation for interface tracking abilities is two-fold: failing to resolve discontinuities dominates the error produced by most hydrocodes, it is therefore important to resolve shocks and contact discontinuities as well as possible; a multi-material code allows materials to have different properties (eg. γ in an ideal gas), different equations of state, or even different phase states. Two interface tracking algorithms are discussed, SLIC and Youngs. The interface tracking ability of the code using Youngs algorithm has been rigorously tested.

Improvements can always be made, it would be desirable to have a two dimensional remap (so the code can preserve any symmetry inherent in the problem), or to work in non-Cartesian geometries. Other desirable improvements include: an interface tracking algorithm which produces interfaces which are continuous; enhancing the multi-material remap to be second order accurate; the ability to track magnetic discontinuities. Depend-

ing upon the type of problem to be solved, material strength and the ability to exchange mass between materials, may be beneficial. The code could be developed in three dimensions, and it would also be possible to include an AMR strategy.

Also in this thesis is an investigation into the dissipation of Alfvén waves due to phase-mixing and the effect of ohmic heating. Boundary motions drive Alfvén waves, slow and fast modes, into an inhomogeneous uniformly resistive plasma. The Alfvén waves phase-mix due to the plasma inhomogeneity, this generates fast modes which interact with the boundary driven fast modes. The Alfvén waves damp due to resistivity, the damping is enhanced in the phase-mixing region. Ohmic heating generates a flow directed along the field.

Preliminary results of the Taylor relaxation of a kink unstable coronal loop is also presented. The simulations have yet to be run to a timewhen the relaxed state can be achieved.

Appendix A

Derivation of artificial viscosity

The 1D ideal gas equations in Lagrangian form are

$$\frac{D\rho}{Dt} = -\rho \frac{\partial u}{\partial x} \quad (\text{A.1})$$

$$\frac{D}{Dt}(\rho u) = -\rho u \frac{\partial u}{\partial x} - \frac{\partial P}{\partial x} \quad (\text{A.2})$$

$$\frac{D}{Dt}(\rho E) = -\rho E \frac{\partial u}{\partial x} - \frac{\partial}{\partial x}(Pu). \quad (\text{A.3})$$

These equations can be simplified by using mass co-ordinates, (van Leer, 1997) ie. let $d\xi = \rho dx$ and $v = 1/\rho$ where v is the specific volume. Then (A.1)-(A.3) become

$$\frac{Dv}{Dt} = \frac{\partial u}{\partial \xi} \quad (\text{A.4})$$

$$\frac{Du}{Dt} = -\frac{\partial P}{\partial \xi} \quad (\text{A.5})$$

$$\frac{DE}{Dt} = -\frac{\partial}{\partial \xi}(Pu). \quad (\text{A.6})$$

From the integral form of the conservative laws, it is possible to derive jump conditions across a shock (Laney, 1998),

$$\frac{Dv}{Dt} + \frac{\partial}{\partial \xi} f(v) = 0 \Rightarrow w(v_R - v_L) = f(v_R) - f(v_L),$$

where v is a conserved property, f is the corresponding flux function, and $w > 0$ is the forward propagating shock speed. Using this jump condition on (A.4)-(A.6) yields

$$w(v_1 - v_0) = u_0 - u_1, \quad (\text{A.7})$$

$$w(u_1 - u_0) = P_1 - P_0, \quad (\text{A.8})$$

$$w(E_1 - E_0) = P_1 u_1 - P_0 u_0. \quad (\text{A.9})$$

The specific total energy can be split into $\epsilon + u^2/2$, so (A.9) becomes

$$\begin{aligned} w(\epsilon_1 - \epsilon_0) &= -\frac{w}{2}(u_1 - u_0)(u_1 + u_0) + P_1 u_1 - P_0 u_0, \\ &= \frac{1}{2}(P_0 + P_1)(u_1 - u_0), \\ \Rightarrow \epsilon_1 - \epsilon_0 &= \frac{P_0 + P_1}{2}(v_0 - v_1). \end{aligned} \quad (\text{A.10})$$

Since $v_1 - v_0 = (\rho_0 - \rho_1)/(\rho_0 \rho_1)$, (A.7), (A.8) and (A.10) become the Rankine-Hugoniot conditions:

$$\begin{aligned} w &= \rho_0 \rho_1 \frac{u_1 - u_0}{\rho_1 - \rho_0} = \frac{P_1 - P_0}{u_1 - u_0} \\ \epsilon_1 - \epsilon_0 &= \frac{P_0 + P_1}{2} \left(\frac{1}{\rho_0} - \frac{1}{\rho_1} \right). \end{aligned}$$

To continue further an equation of state is required. Choosing the ideal gas law (Kuropatenko, 1967), $\epsilon = P/(\rho(\gamma - 1))$, $c_s^2 = (\gamma P)/\rho$, and writing $u_1 - u_0 = \Delta u$, $P_1 - P_0 = \Delta P$, the Rankine-Hugoniot conditions become

$$\frac{\rho_0 \rho_1}{\rho_1 - \rho_0} \Delta u = \frac{\Delta P}{\Delta u} \quad \Rightarrow \quad \rho_1 = \frac{\Delta P \rho_0}{\Delta P - \rho_0 \Delta(u^2)} \quad (\text{A.11})$$

$$\frac{P_1}{\rho_1} - \frac{P_0}{\rho_0} = \frac{\gamma - 1}{2\rho_0} (P_0 + P_1) \left(1 - \frac{\rho_0}{\rho_1} \right). \quad (\text{A.12})$$

Combining (A.11) and (A.12) produces

$$\begin{aligned} P_1(\Delta P - \rho_0(\Delta u^2)) &= P_0 \Delta P + \frac{\Delta P}{2}(\gamma - 1)(P_0 + P_1) \left(1 - \frac{(\Delta P - \rho_0(\Delta u^2))}{\Delta P} \right) \\ &= P_0 \Delta P + \frac{(\gamma - 1)}{2}(P_0 + P_1)\rho_0(\Delta u)^2. \end{aligned} \quad (\text{A.13})$$

(A.13) can be rewritten as a quadratic for P_1 ,

$$P_1^2 - \left(2P_0 + \frac{\gamma+1}{2}\rho_0(\Delta u)^2\right) P_1 + P_0 \left(P_0 - \frac{\gamma-1}{2}\rho_0(\Delta u)^2\right) = 0,$$

the solution of which is,

$$P_1 = P_0 + \frac{\gamma+1}{4}\rho_0(\Delta u)^2 + \rho_0|\Delta u| \left(\left(\frac{\gamma+1}{4} \right)^2 (\Delta u)^2 + c_s^2 \right)^{1/2}.$$

Taking the limits $|\Delta u|^2 \ll c_s^2$ and $|\Delta u|^2 \gg c_s^2$ yields the linear and quadratic terms of the artificial viscosity respectively,

$$q = k_1 c_s \rho |\Delta u| + k_2 \rho (\Delta u)^2, \tag{A.14}$$

where k_1 and k_2 are constants.

Wilkins (1980) suggested replacing c_s in (A.14) with $(P/\rho)^{1/2}$.

Appendix B

Integration of the Induction equation

Integrating the ideal induction equation (1.26) over the volume yields

$$\begin{aligned}\int \frac{D\mathbf{B}}{Dt} dV &= \frac{D}{Dt} \int \mathbf{B} dV - \int \mathbf{B} \frac{D}{Dt} dV \\ &= \frac{D}{Dt} \int \mathbf{B} dV - \int \mathbf{B}(\nabla \cdot \mathbf{u}) dV && \text{(Goedbloed, 1983)} \\ &= \frac{D}{Dt} \int \mathbf{B} dV + \int \frac{D\mathbf{B}}{Dt} dV - \int (\mathbf{B} \cdot \nabla) \mathbf{u} dV.\end{aligned}$$

Therefore,

$$\frac{D}{Dt} \int \mathbf{B} dV = \int (\mathbf{B} \cdot \nabla) \mathbf{u} dV,$$

which in tensor notation is

$$\begin{aligned}\frac{D}{Dt} \int B_i dV &= \int B_j \frac{\partial u_i}{\partial x_j} dV \\ &= \int \frac{\partial}{\partial x_j} (B_j u_i) dV - \int u_i \frac{\partial B_j}{\partial x_j} dV \\ &= \int \frac{\partial}{\partial x_j} (B_j u_i) dV && \text{using the solenoidal condition.}\end{aligned}$$

Integrating the resistive induction equation (1.21) over a surface yields

$$\begin{aligned}
 \int \frac{D}{Dt}(\mathbf{B} \cdot d\mathbf{S}) &= \int \frac{D\mathbf{B}}{Dt} \cdot d\mathbf{S} + \int \mathbf{B} \cdot \frac{D}{Dt}(d\mathbf{S}) \\
 &= \int \left((\mathbf{B} \cdot \nabla) \mathbf{u} - \mathbf{B}(\nabla \cdot \mathbf{u}) \right) \cdot d\mathbf{S} - \int \nabla \wedge (\eta \mathbf{j}) \cdot d\mathbf{S} \\
 &\quad + \int \mathbf{B} \cdot \frac{D}{Dt}(d\mathbf{S}) \qquad \text{from subst. equation (2.8)} \\
 &= \int \left((\mathbf{B} \cdot \nabla) \mathbf{u} - \mathbf{B}(\nabla \cdot \mathbf{u}) \right) \cdot d\mathbf{S} - \int \nabla \wedge (\eta \mathbf{j}) \cdot d\mathbf{S} \\
 &\quad + \int \mathbf{B} \cdot \left(-\nabla(\mathbf{u} \cdot d\mathbf{S}) + (\nabla \cdot \mathbf{u}) d\mathbf{S} \right) \qquad \text{(Goedbloed, 1983)} \\
 &= - \int \nabla \wedge (\eta \mathbf{j}) \cdot d\mathbf{S} \\
 &= - \int \eta \mathbf{j} \cdot d\mathbf{l} \qquad \text{from Stoke's theorem.}
 \end{aligned}$$

Appendix C

Initialising a volume fraction field

Unless the interface lies solely upon grid-lines, some method for initialising ϕ is needed. A mixed cell is divided into two regions (labelled dark and light for convenience) by a single interface. Consider the two dimensional case where a cell is defined by four nodes. An equation specifying the initial interface location within the domain must be given as part of the initial conditions. Whether a node is located in the dark or light region can be determined with reference to this equation. If all four nodes defining a cell lie within the dark region, then $\phi_{dark} = 1$ for that cell. Alternatively, if all four nodes defining a cell lie within the light region, then $\phi_{dark} = 0$. However, if neither of the above is the case (ie. a mixed cell), then the cell is divided into four subcells. Each of the four subcells is tested as for the cell, and these subcells themselves may be subdivided.

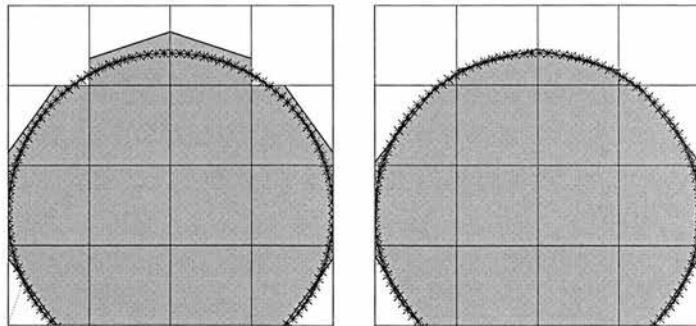


Figure C.1: The effect of p on the interface, showing the reconstruction with $p = 1$ and $p = 5$ respectively.

Obviously this process could continue *ad infinitum*, instead it is curtailed at p subdivi-

sions, for some $p \in \mathbb{N}$. The effect of p is shown in Figure C.1. In this code $p = 10$ is used, since this is an initialisation routine, computational overhead is not so important, and there is some flexibility in setting p . If the centre of the p^{th} subcell lies within the dark region, then $\phi_{dark,p} = 1$. The contribution of a subcell's volume fraction to the cell's volume fraction is $(1/4)^q$, where $1 \leq q \leq p$. Figure C.2 illustrates the subdividing process for a curve with $p = 3$.

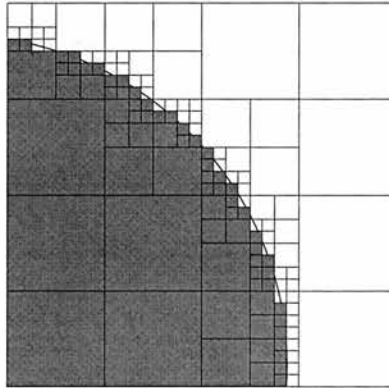


Figure C.2: Schematic of the subdividing process for volume fraction initialisation.

To complete the process, $\phi_{light} = 1 - \phi_{dark}$. If there are several materials present in the domain, and therefore several interfaces, then the process outlined in this section must be carried out consistently so that

$$\sum_{m=1}^n \phi_m = 1, \quad \text{for } n \text{ materials.}$$

Appendix D

Discretisation of the multi-material Ideal gas equations

D.1 Conservation of mass

Integrating (2.18) over a cell moving with the materials gives

$$\int \frac{D}{Dt}(\phi_m \rho_m) dv = - \int \phi_m \rho_m \nabla \cdot \mathbf{u} dv.$$

Using the relation (see Goedbloed (1983))

$$\begin{aligned} \frac{D}{Dt} \int f dv &= \int \frac{Df}{Dt} dv + \int f \frac{D}{Dt}(dv) \\ \Rightarrow \frac{D}{Dt} \int f dv &= \int \frac{Df}{Dt} dv + \int f \nabla \cdot \mathbf{u} dv, \end{aligned} \tag{D.1}$$

yields

$$\frac{D}{Dt} \int (\phi_m \rho_m) dv = 0, \tag{D.2}$$

ie. the mass of individual materials is conserved. The discrete analogue of (D.2), using $dv^{n+1} = (1 + \nabla \cdot \mathbf{u}^n dt) dv^n$ as discussed in section 2.5, is

$$\frac{(1 + \nabla \cdot \mathbf{u}^n dt) dv^n \phi_m^{n+1} \rho_m^{n+1} - dv^n \phi_m^n \rho_m^n}{dt} = 0.$$

Since Equal expansion (see (2.23)) is being used, this simplifies to

$$(1 + \nabla \cdot \mathbf{u}^n dt) \rho_m^{n+1} = \rho_m^n. \quad (\text{D.3})$$

A predictor-corrector discretization is

$$\begin{aligned} \left(1 + \nabla \cdot \mathbf{u}^n \frac{dt}{2}\right) \rho_m^{n+1/2} &= \rho_m^n, \\ (1 + \nabla \cdot \mathbf{u}^{n+1/2} dt) \rho_m^{n+1} &= \rho_m^n. \end{aligned}$$

D.2 Conservation of momentum

Integrating (2.19) over a cell moving with the fluid, and making use of (D.1) produces

$$\frac{D}{Dt} \int \rho \mathbf{u} dv = - \int \nabla P dv$$

The finite difference version is

$$\frac{(1 + \nabla \cdot \mathbf{u}^n dt) dv^n \rho^{n+1} \mathbf{u}^{n+1} - dv^n \rho^n \mathbf{u}^n}{dt} = - \nabla^n P^n dv^n,$$

which simplifies upon using (D.3) to

$$\mathbf{u}^{n+1} = \mathbf{u}^n - \frac{dt}{\rho^n} \nabla^n P^n. \quad (\text{D.4})$$

It is worth noting that in 1D mass co-ordinates (A.5) can be discretized, giving

$$u^{n+1} = u^n - dt \frac{\partial P^n}{\partial \xi},$$

since $\partial \xi$ does not change in time,

$$u^{n+1} = u^n - \frac{dt}{\rho^n} \frac{\partial P^n}{\partial x^n}$$

where $\partial/\partial x^n$ is always on the original grid (even for a corrector step). This can be

generalised for 2D and 3D using $d\xi = \rho dv$ to get

$$\mathbf{u}^{n+1} = \mathbf{u}^n - \frac{dt}{\rho^n dv^n} \nabla(AP^n)$$

where the difference on the original grid is area weighted. This area does change in time, so this is no longer exact (it is $O(dt^2)$), as a second order scheme is being sought, this is acceptable. In any case the $\nabla^n P^n$ term in (D.4) should be treated in an area weighted way.

From (D.4) the predictor-corrector scheme is

$$\mathbf{u}^{n+1} = \mathbf{u}^n - \frac{dt}{\rho^n} \nabla^n(P^{n+1/2}) \quad (\text{D.5})$$

$$\mathbf{u}^{n+1/2} = (\mathbf{u}^{n+1} + \mathbf{u}^n)/2, \quad (\text{D.6})$$

or

$$\mathbf{u}^{n+1/2} = \mathbf{u}^n - \frac{dt}{2\rho^n} \nabla^n(P^{n+1/2}) \quad (\text{D.7})$$

$$\mathbf{u}^{n+1} = 2\mathbf{u}^{n+1/2} - \mathbf{u}^n. \quad (\text{D.8})$$

The above forces conservation of total energy in the Lagrangian step (see appendix D.4), and conservation of mass and momentum in the full (Lagrangian plus remap) step.

It is simple to verify that momentum is conserved:

$$\begin{aligned} \mathbf{M} &= \int \rho^{n+1} \mathbf{u}^{n+1} dv^{n+1} \\ &= \int \rho^n \mathbf{u}^{n+1} dv^n \\ &= \int (\rho^n \mathbf{u}^n - dt \nabla^n(P^{n+1/2})) dv^n \\ &= \int (\rho^n \mathbf{u}^n) dv^n - \int P^{n+1/2} ds. \end{aligned}$$

D.3 Specific internal energy

The predictor step is of basic ‘‘mass co-ordinate’’ form, it does not conserve energy to round-off (only to $O(dt^2)$), however the full predictor-corrector scheme will do so. The

predictor step is

$$\epsilon_m^{n+1/2} = \epsilon_m^n - \frac{dt}{2\rho_m^n} P_m^n \nabla^n \cdot \mathbf{u}^n. \quad (\text{D.9})$$

More care needs to be taken with the corrector step. First note that on using (D.3) and (D.6) that

$$\frac{1}{2} \rho^{n+1} (\mathbf{u}^{n+1})^2 dv^{n+1} = \rho^n dv^n \left((\mathbf{u}^{n+1} - \mathbf{u}^n) \cdot \mathbf{u}^{n+1/2} + \frac{(\mathbf{u}^n)^2}{2} \right). \quad (\text{D.10})$$

Integrating (2.20) over a cell moving with the materials and using (D.1) produces

$$\frac{D}{Dt} \int \phi_m \rho_m \left(\epsilon_m + \frac{u^2}{2} \right) dv = - \int \nabla \cdot (\phi_m P_m \mathbf{u}) dv. \quad (\text{D.11})$$

Discretising gives

$$\frac{(1 + \nabla \cdot \mathbf{u}^{n+1/2} dt) dv^n \phi_m^{n+1} \rho_m^{n+1} (\epsilon_m^{n+1} + (\mathbf{u}^{n+1})^2 / 2)}{dt} - \frac{dv^n \phi_m^n \rho_m^n (\epsilon_m^n + (\mathbf{u}^n)^2 / 2)}{dt} = - \nabla^n \cdot (\phi_m^{n+1/2} P_m^{n+1/2} \mathbf{u}^{n+1/2}) dv^n,$$

which simplifies upon using (D.3) and (D.11) to

$$\epsilon_m^{n+1} = \epsilon_m^n - \frac{dt}{\phi_m^n \rho_m^n} \nabla^n \cdot (\phi_m^{n+1/2} P_m^{n+1/2} \mathbf{u}^{n+1/2}) - \mathbf{u}^{n+1/2} \cdot (\mathbf{u}^{n+1} - \mathbf{u}^n).$$

This can be reduced further using (D.5) and standard vector identities to get

$$\epsilon_m^{n+1} = \epsilon_m^n - \frac{dt}{\rho_m^n} P_m^{n+1/2} \nabla^n \cdot \mathbf{u}^{n+1/2}. \quad (\text{D.12})$$

As mentioned in Section 2.4.2, a particular partitioning of energy has been assumed. The full momentum equation (2.19) is taken to be the sum over the m momentum equations

$$\phi_m \rho_m \frac{D\mathbf{u}_m}{Dt} = - \nabla \phi_m P_m,$$

with $\mathbf{u}_m = \mathbf{u} \forall m$, ie. there is only a single material velocity.

D.4 Energy conservation

It is worth verifying that the finite difference equations conserve total energy.

$$\begin{aligned}
 KE^{n+1} &= \int \frac{1}{2} \rho^{n+1} (\mathbf{u}^{n+1})^2 dv^{n+1} \\
 &= \int \frac{1}{2} \rho^n ((\mathbf{u}^{n+1} - \mathbf{u}^n) \cdot (\mathbf{u}^{n+1} + \mathbf{u}^n) + (\mathbf{u}^n)^2) dv^n && \text{using (D.3)} \\
 &= \int \frac{1}{2} \rho^n (\mathbf{u}^n)^2 dv^n - \int \mathbf{u}^{n+1/2} \cdot \nabla^n P^{n+1/2} dv^n dt && \text{using (D.6), (D.5)}
 \end{aligned}$$

$$\begin{aligned}
 IE^{n+1} &= \int \sum_m \phi_m^{n+1} \rho_m^{n+1} \epsilon_m^{n+1} dv^{n+1} \\
 &= \int \sum_m \phi_m^n \rho_m^n \epsilon_m^n dv^n \\
 &\quad - \int \sum_m P_m^{n+1/2} \phi_m^n \nabla^n \cdot \mathbf{u}^{n+1/2} dt dv^n && \text{using (D.3), (D.12)} \\
 &= \int \sum_m \phi_m^n \rho_m^n \epsilon_m^n dv^n - \int \sum_m \nabla^n \cdot (\phi_m^n P_m^{n+1/2} \mathbf{u}^{n+1/2}) dv^n dt \\
 &\quad + \int \mathbf{u}^{n+1/2} \cdot \nabla P^{n+1/2} dv^n dt
 \end{aligned}$$

$$\begin{aligned}
 TE^{n+1} &= KE^{n+1} + IE^{n+1} \\
 &= \int \left(\frac{1}{2} \rho^n (\mathbf{u}^n)^2 + \sum_m \phi_m^n \rho_m^n \epsilon_m^n \right) dv^n \\
 &\quad - \int \sum_m \nabla^n \cdot (\phi_m^n P_m^{n+1/2} \mathbf{u}^{n+1/2}) dv^n dt
 \end{aligned}$$

The last term on the rhs. is zero for rigid or periodic boundary conditions, otherwise it is a source term. So $TE^{n+1} = TE^n$ and total energy is conserved to round-off during the Lagrangian step. Note that total energy is not conserved for the ideal MHD equations.

Bibliography

- Abramowitz, M. and Stegun, I. (1965). *Handbook of mathematical functions with Formulas, Graphs and mathematical Tables*. Dover Publications.
- Arber, T.D. Longbottom, A. and Van der Linden, R. (1999). Unstable Coronal Loops: numerical simulations with predicted observational signatures. *ApJ*, 517:990–1001.
- Arber, T., Longbottom, A., Gerrard, C., and Milne, A. (2001). A staggered grid, Lagrangian-Eulerian remap code for 3-D MHD simulations. *J. Comput. Phys*, 171:151–181.
- Ashgriz, N. and Poo, J. (1991). Flair: Flux Line-Segment Model for Advection and Interface Reconstruction. *J. Comput. Phys*, 93:449–468.
- Aulisa, E., Manservigi, S., and Scardovelli, R. (2004). A surface marker algorithm coupled to an area preserving marker redistribution method for three-dimensional interface tracking. *J. Comput. Phys*, 197:555–584.
- Baer, M. and Nunziato, J. (1986). A Two-phase Mixture Theory for the Deflagration- to-Detonation Transition (DDT) in Reactive Granular Materials. *Int. J. Multiphase Flow*, 12:861–889.
- Balescu, R. and Paiva-Veretennicoff, I. (1978). Anomalous transport coefficients in a turbulent plasma. *J. Plasma Physics*, 20:231–263.
- Baty, H. (2000). Magnetic topology during the reconnection process in a kinked coronal loop. *A&A*, 360:345–350.
- Baty, H. and Heyvaerts, J. (1996). Electric current concentration and kink instability in line-tied coronal loops. *A&A*, 308:935–950.
- Bdzil, J., Menikoff, R., Son, S., Kapila, A., and Stewart, D. (1999). Two-phase modeling of deflagration-to-detonation transition in granular materials: A critical examination of modeling issues. *Physics of Fluids*, 11:378–402.
- Bell, J., Colella, P., and Glaz, H. (1989). A second order projection method for the incompressible Navier-stokes equations. *J. Comput. Phys*, 85:257–283.
- Benson, D. (1992). Computational methods in Lagrangian and Eulerian hydrocodes.

- Comput. Methods Appl. Mech. Engrg.*, 99:235–394.
- Benson, D. (1998). Eulerian finite element methods for the micromechanics of heterogeneous materials: Dynamic prioritization of material interfaces. *Comput. Methods Appl. Mech. Engrg.*, 151:343–360.
- Benson, D. (2002). Volume of fluid interface reconstruction methods for multi-material problems. *Appl. Mech. Rev.*, 55.
- Berger, M. (1984). Rigorous new limits on magnetic helicity dissipation in the solar corona. *GApFD*, 30:79–104.
- Botha, G., Arber, T., Nakariakov, V., and Keenan, F. (2000). A developed stage of Alfvén wave phase mixing. *A&A*, 363:1186–1194.
- Bourne, N. and Field, J. (1992). Shock induced collapse of single cavities in liquids. *J. Fluid Mech.*, 244:225–240.
- Boyd, T. and Sanderson, J. (2003). *The Physics of Plasmas*. CUP.
- Brackbill, J. and Barnes, D. (1980). The effect of Non-zero $\nabla \cdot \mathbf{B}$ on the numerical solution of the magnetohydrodynamic equations. *J. Comput. Phys*, 35:426–430.
- Braginskii, S. (1965). Transport processes in a plasma. *Reviews of Plasma Physics*, 1:205.
- Brio, M. and Wu, C. (1988). An upwinding differencing scheme for the equations of ideal MHD. *J. Comput. Phys*, 75:400–422.
- Browning, P. (1988). Helicity injection and relaxation in a solar-coronal magnetic loop with a free surface. *J. Plasma Physics*, 40:263–280.
- Browning, P. (1991). Mechanisms of Solar Coronal heating. *Plasm.Phys. Contr. Nucl. Fus.*, 33:539–571.
- Browning, P. and Priest, E. (1986). Heating of coronal arcades by magnetic tearing turbulence, using the Taylor-Heyvaerts hypothesis. *A&A*, 159:129–141.
- Browning, P., Sakurai, T., and Priest, E. (1986). Coronal heating in closely-packed flux tubes - A Taylor-Heyvaerts relaxation theory. *A&A*, 158:217–227.
- Browning, P. and Van der Linden, R. (2003). Solar coronal heating by relaxation events. *A&A*, 400:355–367.
- Bruce Stewart, H. and Wendroff, B. (1984). Two-Phase Flow: Models and Methods. *J. Comput. Phys*, 56:363–409.
- Bychenkov, V., Silin, V., and Uryupin, S. (1988). Ion-acoustic turbulence and anomalous transport. *Physics Reports*, 164:119–215.
- Caramana, E., Shaskov, M., and Whalen, P. (1990). Formulations of artificial viscosity for multidimensional shock wave computations. *J. Comput. Phys*, 144:70–97.
- Chang, S., Wang, X., and Chow, C. (1999). The space-time conservation element and

- solution element method: A new high resolution and genuinely multidimensional paradigm for solving conservation laws. *J. Comput. Phys*, 156:89–136.
- Colella, P. and Woodward, P. (1984). The Piecewise Parabolic Method (PPM) for gas-dynamical simulations. *J. Comput. Phys*, 54:174–201.
- Craig, I. and Sneyd, A. (1986). A dynamic relaxation technique for determining the structure and stability of Coronal magnetic fields. *Astrophysical journal*, 311:451–459.
- De Moortel, I., Hood, A., and Arber, T. (2000). Phase mixing of Alfvén waves in a stratified and radially diverging atmosphere. *A&A*, 354:334–348.
- De Moortel, I., Ireland, J., Walsh, R., and Hood, A. (2002). Longitudinal density oscillations in coronal loops observed with TRACE-i: Overview of measured parameters. *Sol. Phys.*, 209:61–88.
- Démoulin, P. (1991). *Advances in Solar system Magnetohydrodynamics*, chapter - Solar Prominences. CUP.
- Evans, C. and Hawley, J. (1988). Simulation of magnetohydrodynamic flows: a constrained transport method. *Astrophysical journal*, 332:659–677.
- Giddings, R. (2001). *Godunov Methods: Theory and Applications*, chapter - HELMIT - A new interface reconstruction algorithm, pages 367–376. Kluwer Academic.
- Goedbloed, J. (1983). *Lecture notes on Ideal MHD*. FOM.
- Golub, L. and Pasachoff, J. (2001). *Nearest Star*. Harvard.
- Haas, J. and Sturtevant, B. (1987). Interaction of weak shock waves with cylindrical and spherical gas inhomogeneities. *J. Fluid Mech.*, 181:41–76.
- Harten, A. (1983). High resolution schemes for hyperbolic conservation laws. *J. Comput. Phys*, 49:357–393.
- Heyvaerts, J. and Priest, E. (1983). Coronal heating by phase-mixed shear Alfvén waves. *A&A*, 117:220–234.
- Heyvaerts, J. and Priest, E. (1984). Coronal heating by reconnection in DC current systems - A theory based on Taylor’s hypothesis. *A&A*, 137:63–78.
- Hirt, C. and Nichols, B. (1981). Volume of Fluid (VOF) Method for the Dynamics of Free Boundaries. *J. Comput. Phys*, 39:201–225.
- Hood, A., Ireland, J., and Priest, E. (1997). Heating of Coronal holes by phase mixing. *A&A*, 318:957–961.
- Hu, X. and Khoo, B. (2004). An interface interaction method for compressible multifluids. *J. Comput. Phys*, 198:35–64.
- Hui, W., Li, P., and Li, Z. (1999). A unified coordinate system for solving the two-dimensional euler equations. *J. Comput. Phys*, 160:89–136.

- Ionson, J. (1978). Resonant absorption of Alfvénic surface waves and the heating of solar coronal loops. *ApJ*, 226:650–673.
- Ireland, J. and Priest, E. (1997). Phase-mixing in Dissipative Alfvén Waves. *Sol. Phys.*, 173:31–51.
- Ji, H. (1999). *Magnetic Helicity in Space and Laboratory Plasmas*, chapter - Helicity, Reconnection and Dynamo effects. AGU.
- Jiang, G. and Shu, C. (1996). Efficient implementation of weighted ENO schemes. *J. Comput. Phys.*, 126:202–228.
- Kuropatenko, V. (1967). *Difference methods for solutions of problems of mathematical physics, I*. American mathematical society, Providence.
- Landshoff, R. (1955). A numerical method for treating fluid flow in the presence of shocks. Technical Report LA-1930, Los Alamos National Laboratory.
- Laney, C. (1998). *Computational gas dynamics*. CUP.
- Lax, P. and Liu, X. (1998). Solution of two dimensional Riemann problem of gas dynamics by positive schemes. *SIAM J. Sci. Comput.*, 19:319–340.
- LeVeque, R. (1992). *Numerical Methods for Conservation Laws*. Lectures in Mathematics. Birkhäuser Verlag.
- Leveque, R. (1996). High-resolution conservative algorithms for advection in incompressible flow. *SIAM J. Numer. Anal.*, 33:627–665.
- Liska, R. and Wendroff, B. (2001). Comparison of several difference schemes on 1D and 2D test problems for the Euler equations. Technical Report LA-UR-01-6225, Los Alamos National Laboratory.
- Londrillo, P. and Del Zanna, L. (2000). High-order upwind schemes for multidimensional magnetohydrodynamics. *ApJ*, 530:508–524.
- Lothian, R. and Browning, P. (2000). Energy dissipation and helicity in coronal loops of variable cross-section. *Sol. Phys.*, 194:205–227.
- Melrose, D. (2004). Conservation of both current and helicity in a quadrupolar model for solar flares. *Sol. Phys.*, 221:121–133.
- Miller, G. and Puckett, E. (1996). A High-Order Godunov Method for Multiple Condensed Phases. *J. Comput. Phys.*, 128:134–164.
- Nakariakov, V. and Oraevsky, V. (1995). Resonant interactions of modes in Coronal magnetic flux tubes. *Solar Phys.*, 160:289–302.
- Nakariakov, V., Roberts, B., and Murawski, K. (1997). Alfvén wave phase mixing as a source of Fast magnetosonic waves. *Solar Phys.*, 175:93–105.
- Nakariakov, V., Roberts, B., and Murawski, K. (1998). Nonlinear coupling of MHD

- waves in inhomogeneous steady flows. *A&A*, 332:795–804.
- Nandy, D., Hahn, M., Canfield, R., and Longcope, D. (2003). Detection of a Taylor-like Plasma Relaxation Process in the Sun. *ApJ*, 597:L73–L76.
- Noh, W. (1978). Errors for Calculations of Strong Shocks Using an Artificial Viscosity and an Artificial Heat Flux. *J. Comput. Phys*, 72:78–120.
- Noh, W. and Woodward, P. (1976). *Lecture Notes in Physics*, volume 59, chapter - SLIC (Simple Line Interface Calculation). Springer.
- Ofman, L. and Davila, J. (1997). Solar wind acceleration by solitary waves in Coronal holes. *ApJ*, 476:357–365.
- Osher, S. and Fedkiw, R. (2001). Level Set Methods: An Overview and Some Recent Results. *J. Comput. Phys*, 169:463–502.
- Parker, E. (1963). The Solar phenomenon and the theory of reconnection and annihilation of magnetic fields. *ApJ Suppl.*, 8:177–211.
- Parker, E. (1988). Nanoflares and the Solar X-ray Corona. *ApJ*, 330:474–479.
- Petschek, H. (1964). Magnetic field annihilation. In *AAS-NASA Symp. on Solar Flares*, pages 425–439.
- Pilliod, J. and Puckett, E. (1999). Second-Order Accurate Volume-of-Fluid Algorithms for Tracking Material Interfaces. *J. Comput. Phys*, 199:465–502.
- Powell, K. (1994). An approximate Riemann solver for magnetohydrodynamics (that works in more than one dimension). Technical Report 92-94, ICASE.
- Priest, E. (1982). *Solar Magnetohydrodynamics*. Kluwer.
- Priest, E. and Forbes, T. (2000). *Magnetic Reconnection: MHD theory and Applications*. CUP.
- Priest, E. and Forbes, T. (2002). The magnetic nature of solar flares. *A&A Rev.*, 10:313–377.
- Priest, E., Longcope, D., and Heyvaerts, J. (2005). Coronal Heating at Separators and Separatrices. *ApJ*, 624:1057–1071.
- Quirk, J. and Karni, S. (1996). On the dynamics of shock-bubble interaction. *J. Fluid Mech.*, 318:129–163.
- Rider, W. (2000). Revisiting Wall Heating. *J. Comput. Phys*, 162:395–410.
- Rider, W. and Kothe, D. (1995). Stretching and Tearing Interface Tracking Methods. In *The 12th AIAA CFD Conference, San Diego, June 20, 1995, AIAA-95-1717*.
- Rider, W. and Kothe, D. (1998). Reconstructing Volume Tracking. *J. Comput. Phys*, 141:112–152.
- Roberts, B. (1991). *Advances in Solar System Magnetohydrodynamics*, chapter - MHD

- waves in the Sun. CUP.
- Roberts, B. (2000). Waves and Oscillations in the Corona. *Sol. Phys.*, 193:139–152.
- Roe, P. (1985). Some contributions to the modeling of discontinuous flows. *Lect. Notes Appl. Math.*, 22:163–193.
- Ryu, D. and Jones, T. (1995). Numerical magnetohydrodynamics in Astrophysics: Algorithms and tests for one dimensional flow. *ApJ*, 442:228–258.
- Ryu, D., Miniati, F., Jones, T., and Frank, A. (1998). A divergence free upwind code for multidimensional magnetohydrodynamic flows. *ApJ*, 509:244–255.
- Ryutova, M. and Habbal, S. (1995). The effects of mass flows on the dissipation of Alfvén waves in the upper layers of the Solar atmosphere. *ApJ*, 451:381–390.
- Schulz, W. (1964). Tensor artificial viscosity for numerical hydrodynamics. *J. Math. Phys.*, 5:133–138.
- Schulz-Rinne, C., Collins, J., and Glaz, H. (1993). Numerical solution of the Riemann problem for two-dimensional gas dynamics. *SIAM J. Sci. Comput.*, 14:1394–1414.
- Sod, G. (1978). A survey of several finite difference methods for systems of non-linear hyperbolic conservation laws. *J. Comput. Phys.*, 27:1–31.
- Soward, A. and Priest, E. (1982). Fast magnetic field-line reconnection in a compressible fluid. Part 1. coplanar field lines. *ApJ*, 28:335–367.
- Strang, G. (1968). On the construction and comparison of difference schemes. *SIAM J. Numer. Anal.*, 5:506–517.
- Swartz, B. (1989). The second-order sharpening of blurred smooth borders. *Mathematics of Computation*, 52:675–714.
- Sweby, P. (1984). High resolution schemes using flux limiters for hyperbolic conservation laws. *SIAM J. Numer. Anal.*, 21:995–1011.
- Sweet, P. (1958). The neutral point theory of Solar flares. In *IAU Symp. 6*, pages 123–134.
- Taylor, J. (1974). Relaxation of Toroidal Plasma and Generation of Reverse Magnetic Fields. *Physical Review Letters*, 33:1139–1141.
- Taylor, J. (1986). Relaxation and magnetic reconnection in plasmas. *Reviews of Modern Physics*, 58:741–763.
- Toro, E. (1997). *Riemann Solvers and Numerical Methods for Fluid Dynamics*. Springer-Verlag.
- Tóth, G. (2000). The $\nabla \cdot \mathbf{B} = 0$ constraint in shock-capturing magnetohydrodynamics codes. *J. Comput. Phys.*, 161:605–652.
- Tsiklauri, D., Arber, T., and Nakariakov, V. (2001). A weakly nonlinear Alfvénic pulse in a transversely inhomogeneous medium. *A&A*, 379:1098–1105.

- Tsiklauri, D., Arber, T., and Nakariakov, V. (2002). A strongly nonlinear Alfvénic pulse in a transversely inhomogeneous medium. *A&A*, 395:285–292.
- Van der Linden, R. and Hood, A. (1998). A complete solar coronal loop stability analysis in ideal magnetohydrodynamics. i. non-force-free cylindrical equilibria. *A&A*, 339:887–896.
- van Leer, B. (1997). Towards the ultimate conservative difference scheme V. *J. Comput. Phys*, 135:229–248. Originally printed in JCP 32:101.
- Vekstein, G., Priest, E., and Steele, C. (1993). On the problem of magnetic coronal heating by turbulent relaxation. *ApJ*, 417:781–789.
- Velli, M., Lionello, R., and Einaudi, G. (1997). Kink Modes and Current Sheets in Coronal Loops. *Sol. Phys.*, 172:257–266.
- von Neumann, J. and Richtmyer, R. (1950). A method for the numerical calculation of hydrodynamic shocks. *Journal of applied physics*, 21:232–237.
- Wilkins, M. (1980). Use of artificial viscosity in multi-dimensional fluid dynamic calculations. *J. Comput. Phys*, 36:281–303.
- Woodward, P. and Colella, P. (1984). The numerical simulation of two-dimensional fluid flow with strong shocks. *J. Comput. Phys*, 54:115–173.
- Xiaoming, Q. and Balescu, R. (1982). Anomalous transport coefficients in a magnetized turbulent plasma. *J. Plasma Physics*, 22:193–214.
- Youngs, D. (1982). *Numerical Methods for Fluid Dynamics*, chapter - Time dependent multi-material flow with large fluid distortion, pages 273–285. Academic Press.
- Youngs, D. (1987). An Interface Tracking Method for a 3D Eulerian Hydrodynamics Code. Technical Report AWRE/44/92/35, Atomic Weapons Research Establishment.
- Zalesak, S. (1979). Fully multidimensional Flux-Corrected transport algorithms for fluids. *J. Comput. Phys*, 31:335–362.
- Zhang, M. and Low, B. (2003). Magnetic flux emergence into the Solar Corona. III The role of magnetic helicity conservation. *ApJ*, 584:479–496.